

2011-01-01

# Development and Characterization of the Oxidation Behavior of Various High Temperature Niobium Based Alloys

Benedict Isabel Portillo

University of Texas at El Paso, benp34@gmail.com

Follow this and additional works at: [https://digitalcommons.utep.edu/open\\_etd](https://digitalcommons.utep.edu/open_etd)



Part of the [Materials Science and Engineering Commons](#), and the [Mechanics of Materials Commons](#)

---

## Recommended Citation

Portillo, Benedict Isabel, "Development and Characterization of the Oxidation Behavior of Various High Temperature Niobium Based Alloys" (2011). *Open Access Theses & Dissertations*. 2366.  
[https://digitalcommons.utep.edu/open\\_etd/2366](https://digitalcommons.utep.edu/open_etd/2366)

This is brought to you for free and open access by DigitalCommons@UTEP. It has been accepted for inclusion in Open Access Theses & Dissertations by an authorized administrator of DigitalCommons@UTEP. For more information, please contact [lweber@utep.edu](mailto:lweber@utep.edu).

DEVELOPMENT AND CHARACTERIZATION OF THE OXIDATION  
BEHAVIOR OF VARIOUS HIGH TEMPERATURE  
NIOBIUM BASED ALLOYS

BENEDICT I PORTILLO II  
Materials Science and Engineering

APPROVED:

---

Shailendra K. Varma, Ph.D., Chair

---

Lawrence E. Murr, Ph.D.

---

Felicia S. Manciu, Ph.D.

---

Russell R. Chianelli, Ph.D.

---

Benjamin C. Flores, Ph.D.  
Acting Dean of the Graduate School

Copyright  
by  
Benedict I Portillo II  
2011

## **Dedication**

Dedicated to my Parents and the Almighty.

Everything should be made as simple as possible, but not simpler.  
-Albert Einstein



DEVELOPMENT AND CHARACTERIZATION OF THE OXIDATION  
BEHAVIOR OF VARIOUS HIGH TEMPERATURE  
NIOBIUM BASED ALLOYS

by

BENEDICT I PORTILLO II, MS. BS.

DISSERTATION

Presented to the Faculty of the Graduate School of

The University of Texas at El Paso

in Partial Fulfillment

of the Requirements

for the Degree of

DOCTOR OF PHILOSOPHY

Materials Science and Engineering Program

THE UNIVERSITY OF TEXAS AT EL PASO

December 2011

## **Acknowledgements**

I would like to acknowledge the guidance and support the faculty of the Materials and Science Engineering program have provided me while I pursued my degree at UTEP. I would also like to acknowledge the financial support of the Office of Naval Research through the grant number N00014-08-1-0506. The contributions made to the Murchison Graduate Engineering Scholarship Fund by Mr. Eric Pearson, Mrs. Patricia M. Babel, Ms. Dede Rogers, and Mr. Jonathan W. Rogers, Jr. were also greatly appreciated.

## Abstract

The oxidation response of various niobium based refractory alloys from the Nb-Mo-Si-B-X alloy system has been examined at temperatures between 700 and 1400°C in air. The development of these alloys was part of an ongoing effort to develop and discover a new materials system capable of replacing nickel based super alloys. Additions of titanium were found to provide limited oxidation resistance. A discontinuous layer of  $\text{TiO}_2$  was observed to form at temperatures above 1100°C. Alloys containing titanium additions were observed to suffer from pest oxidation at low and intermediate temperatures due to the development of  $\text{Nb}_2\text{O}_5$ . Poor oxidation resistance at intermediate temperatures for alloys with titanium additions was attributed to a transformation in the structure of  $\text{Nb}_2\text{O}_5$  formed. Additions of chromium were observed to increase oxidation resistance through the development of a layered oxide structure containing  $\text{SiO}_2$  and  $\text{CrNbO}_4$ . An intermediate oxidation layer was observed to develop along the oxide metal interface in which the solid solution was not oxidized. These alloys were found to be susceptible to pest oxidation at intermediate and low oxidation temperatures between 700 and 1000°C. Boron and molybdenum content was modified and shown to suppress pest oxidation at 700°C. Modified molybdenum content led to the development of molybdenum based  $\alpha$  primary solid solution instead of niobium. Alloys with modified molybdenum and boron content were found to have the best oxidation resistance surviving 168 hours of cyclic oxidation at 1400°C. Transient oxidation behavior was observed in thermal gravimetric results collected at 1200°C in the alloys with modified boron and molybdenum content and attributed to the preferential oxidation of  $\text{Nb}_5\text{Si}_3$ . Oxidation behavior was characterized by the weight change per surface area method and by thermal gravimetric analysis. Oxidation products were characterized by x-ray diffraction and scanning electron microscopy in several modes including backscatter imaging, secondary imaging, energy dispersive x-ray spectroscopy, and x-ray mapping.

## Table of Contents

Acknowledgements.....	v
Abstract.....	vi
Table of Contents.....	vii
List of Tables .....	ix
List of Figures.....	x
Chapter 1: INTRODUCTION .....	1
1.1 Justification.....	3
1.2 References.....	4
Chapter 2: LITURATURE REVIEW .....	5
2.1 Refractory Metals .....	5
2.1 Oxidation of Pure Niobium .....	6
2.2 Laves Phases .....	8
2.3 Oxidation of Nb-Cr alloys containing Laves phase.....	10
2.4 Oxidation of Mo-Si-B.....	11
2.5 Oxidation of Nb-Mo-Si.....	12
2.6 Oxidation of Nb-Si-B .....	12
2.7 Oxidation of Nb-Cr-Si .....	13
2.8 Oxide Volatilization.....	13
2.9 Characterization of Oxidation Curves .....	15
2.10 References.....	17
Chapter 3: Experimental Procedure.....	21
3.1 Sample Preparation.....	21
3.2 Short Term Oxidation .....	21
3.3 Cyclic Oxidation.....	22
3.4 Oxide Scale Development .....	22
3.5 Thermal Gravimetric Studies.....	22
3.6 X-ray Diffraction Analysis .....	22
3.7 Scanning Electron Microscopy.....	23

Chapter 4: Preliminary Studies .....	24
4.1 Oxidation behavior of Nb-Mo-Si-B with titanium additions .....	24
4.1.1 As Cast Microstructures .....	25
4.1.2 Short Term Oxidation Results .....	27
4.1.3 Short Term Cyclic Oxidation Results .....	29
4.1.4 Oxide Scale Development .....	30
4.1.5 Long Term Cyclic Oxidation Results .....	32
4.1.6 Comparison of Titanium Additions and Chromium Additions ..	33
4.2 Oxidation Behavior of Nb-Mo-Si-B With Chromium Additions.....	35
4.2.1 As Cast Microstructures .....	36
4.2.2 Short Term Oxidation Results .....	39
4.2.3 Discussion.....	49
4.3 Summary.....	52
4.3 References.....	53
Chapter 5: Results and Discussion .....	55
5.1 Characterization of The As-cast Microstructure.....	55
5.2 Short Term Oxidation Results .....	63
5.3 Thermal Gravimetric Characterization .....	72
5.4 Oxide Scale Development .....	76
5.5 Long Term Cyclic Oxidation.....	82
5.6 Summary.....	89
5.7 Recommendations.....	90
5.8 References.....	91
Curriculum Vita .....	92

## List of Tables

Table 1.1	Preliminary experimental alloy compositions .....	4
Table 2.1	Select physical properties of refractory metals and nickel for comparison.....	5
Table 3.1	Compositions of experimental alloys .....	21
Table 4.1	Alloy compositions intended to study the effects of chromium composition and boron additions.....	36
Table 4.2	Phase fractions calculated for preliminary alloys studied containing various chromium and boron additions. ....	38
Table 5.1	Image analysis results of the as-cast microstructures of the 10Mo5B, 15Mo5B and 10B alloys.....	59

## List of Figures

Figure 1.1	Specific power as a function of temperature .....	2
Figure 2.1	Linear rate constants for the oxidation of niobium as a function of temperature.....	6
Figure 2.2	Tetrahedra formed by the B atoms in the three different Laves structures (a) C15 MgCu <sub>2</sub> , (b) C14 MgZn <sub>2</sub> , and (c) C36 MgNi <sub>2</sub> . ....	9
Figure 2.3	Arrangement of the A atoms in the three Laves phase lattices (a) C14 MgZn <sub>2</sub> , (b) C15 MgCu <sub>2</sub> , and (c) C36 MgNi <sub>2</sub> .....	9
Figure 2.4	Illustration of a typical logarithmic and inverse logarithmic oxidation curves .....	15
Figure 2.5	Representation of typical linear and parabolic oxidation curves .....	17
Figure 4.1	Calculated isothermal sections from the Nb-20Mo-15Si-5B-20Ti alloy at 800°C (a) and 1300°C. Sections were calculated using Pandat <sup>TM</sup> software. ....	26
Figure 4.2	As cast microstructure shown in backscatter of 20Ti alloy solid solution and Nb <sub>5</sub> Si <sub>3</sub> identified [4]. ....	26
Figure 4.3	XRD spectra of as received Nb-20Mo-15Si-5B-20Ti alloy. ....	26
Figure 4.4	Short term oxidation results from the Nb-20Mo-15Si-5B-20Ti alloy obtained after 24 hours of oxidation in air.....	27
Figure 4.5	Oxide metal interface shown at 800 to 1000°C after short term oxidation, the large amounts of Nb <sub>2</sub> O <sub>5</sub> developed are attributed to the oxidation of the niobium solid solution. ....	28
Figure 4.6	Layered oxide developed at 1300°C after 24 hours of oxidation. (a) dense oxide layer developed at the oxide metal interface, (b) second layer consisting of Nb <sub>2</sub> O <sub>5</sub> and TiO <sub>2</sub> oxide grains dispersed in SiO <sub>2</sub> , and (c) oxide developed at air oxide interface consisting of Nb <sub>2</sub> O <sub>5</sub> and SiO <sub>2</sub> . ....	28
Figure 4.7	Short term cyclic oxidation of Nb-20Mo-15Si-5B-20Ti .....	29
Figure 4.8	Oxide metal interface developed at (a) 700, (b) 900, (c) 1100, and (d) 1300°C after 5 minutes of oxidation in air followed by an air quenching .....	30
Figure 4.9	20Ti alloy x-ray maps showing molybdenum rich layer along the oxide metal interface at 250X after oxidation at 1300°C. ....	31
Figure 4.10	Long term cyclic oxidation of 20Ti alloy in air for 168 hours. ....	32
Figure 4.11	20Cr alloy as cast microstructure containing NbCr <sub>2</sub> Laves phase, Nb <sub>5</sub> Si <sub>3</sub> , Nb <sub>3</sub> Si and a niobium solid solution. ....	33
Figure 4.12	Comparison of short term oxidation data of Nb-20Mo-15Si-5B-20X alloy with chromium and titanium additions .....	34
Figure 4.13	Oxide metal interfaces developed on the 20Cr alloy after short term oxidation at 800, 900, and 1300°C .....	35
Figure 4.14	Phase fractions as a function of temperature calculated using Pandat <sup>TM</sup> for alloy compositions containing (a) 20 and (b) 25Cr additions. ....	36
Figure 4.15	As cast microstructures for preliminary alloys in collected in back scatter mode. ....	37
Figure 4.16	Isothermal sections calculated for the Nb-Mo-Si-Cr system at 700 and 1300°C while holding 25at.%Cr constant .....	39
Figure 4.17	Short term oxidation results for the 25Cr, and the 25Cr5B alloy .....	40
Figure 4.18	Thermal gravimetric data collected over 24 hours of oxidation of the 25Cr and 25Cr5B alloys in air at 800, 1000, and 1200°C. ....	41
Figure 4.19	Oxide metal interfaces developed on both the 25Cr and 25Cr5B alloy at 700, 800, and 900°C after short term oxidation.....	43

Figure 4.20	Closer examination of the oxide metal interface and intermediate oxide layer developed on the 25Cr5B alloy after short term oxidation at 900°C. ....	44
Figure 4.21	X-ray maps collected from the oxide metal interface developed on the 25Cr5B alloy after short term oxidation at 900°C showing the chromium depletion and molybdenum enrichment of the intermediate oxidation layer. ....	45
Figure 4.22	EDS spectra collected for SiO <sub>2</sub> matrix developed in the oxide scale of the 25Cr5B alloy after short term oxidation at 900°C .....	46
Figure 4.23	Oxide metal interfaces developed after short term oxidation at 1000 and 1100°C for the 25Cr and 25Cr5B alloys. ....	46
Figure 4.24	X-ray maps collected along the oxide metal interface developed on the 25Cr alloy after short term oxidation at 1000°C. Voids in the oxide scale are shown to be lined with SiO <sub>2</sub> . ....	47
Figure 4.25	Oxide metal interface and oxide air interface developed on the 25Cr and 25Cr5B alloys after short term oxidation at 1300°C showing the spalling of the oxide from the 25Cr alloy. ....	48
Figure 4.26	High magnification micrograph of the dense oxide scale developed on the 25Cr alloy after short term oxidations showing the composition of the fine oxide structure. ....	49
Figure 4.27	X-ray diffraction spectra collected from surface oxides developed on both 25Cr and 25Cr5B alloy after short term oxidation. ....	50
Figure 5.1	Calculated isothermal sections for Nb-25Cr-20Mo-15Si-10B, Nb-25Cr-15Mo-20Si-5B, and Nb-25Cr-10Mo-15Si-5B alloys at (a) 700 and (b) 1300°C. Three common phases were predicted a solid solution, NbCr <sub>2</sub> Laves phase, and Nb <sub>5</sub> Si <sub>3</sub> . ....	56
Figure 5.2	Back scatter micrographs of as cast microstructures at 1000x mag (a) Nb-25Cr-15Mo-20Si-5B, (b) Nb-25Cr-20Mo-15Si-10B, and (c) Nb-25Cr-10Mo-15Si-5B alloys.....	57
Figure 5.3	XRD spectra collected for Nb-25Cr-15Mo-20Si-5B, Nb-25Cr-20Mo-15Si-10B, and Nb-25Cr-10Mo-15Si-5B alloys. alloy comps in the as cast condition. ....	58
Figure 5.4	X-ray map of Nb-25Cr-15Mo-20Si-5B alloy in the as cast condition at 1500X magnification. ....	60
Figure 5.5	X-ray map of Nb-25Cr-20Mo-15Si-10B alloy in the as cast condition at 1500X magnification. ....	61
Figure 5.6	X-ray map of Nb-25Cr-10Mo-15Si-5B alloy in the as cast condition at 1500X magnification. ....	62
Figure 5.7	Short term oxidation results for 10Mo5B, 15Mo5B, and the 10B alloys from 700 to 1400°C. ....	63
Figure 5.8	Oxide metal interfaces developed after short term oxidation at 800, 900, 1000°C for the 10B, 15Mo5B, and 10Mo5B alloys micrographs collected in back scatter imaging mode.....	67
Figure 5.9	Oxide metal interfaces developed after short term oxidation at 1100, 1200, 1300°C for the 10B, 15Mo5B, and 10Mo5B alloys micrographs collected in back scatter imaging mode. White parentheses indicate location of intermediate oxide phase .....	68
Figure 5.10	Oxide metal interfaces developed after short term oxidation at 1400°C for the (a) 10B alloy and (b) the 15Mo5b alloy. ....	69
Figure 5.11	XRD spectra collected at 800°C of the surface oxides after short term oxidation of the 10B, 15Mo5B, and 10Mo5B alloys.....	70



Figure 5.12	XRD spectra collected at 1200°C of the surface oxides after short term oxidation of the 10B, 15Mo5B, and 10Mo5B alloys.....	71
Figure 5.13	EDS spectra collected from the Nb-25Cr-20Mo-15Si-10B alloy after 244 hrs of oxidation at 1200°C. The SiO <sub>2</sub> matrix spectra was collected from the SiO <sub>2</sub> layer with dispersed CrNbO <sub>4</sub> oxide. The solid solution spectra was collected from the remaining molybdenum solid solution in the intermediate oxidation layer. The Nb <sub>2</sub> O <sub>5</sub> spectrum was collected near the SiO <sub>2</sub> matrix closest to the air oxide interface. ....	72
Figure 5.14	Thermal gravimetric results collected for Nb-25Cr-15Mo-20Si-5B and Nb-25Cr-20Mo-15Si-10B alloys at 800°C for 24 hours. ....	73
Figure 5.15	Thermal gravimetric results collected for Nb-25Cr-15Mo-20Si-5B and Nb-25Cr-20Mo-15Si-10B alloys at 1000°C for 24 hours. ....	74
Figure 5.16	Thermal gravimetric results collected for Nb-25Cr-15Mo-20Si-5B and Nb-25Cr-20Mo-15Si-10B alloys at 1200°C for 24 hours. ....	75
Figure 5.17	Micrographs at 250X and 1000X of the surface oxides developed on the 10B, 15Mo5B, and 10Mo5B alloys after a 10°C/min ramp to 900°C and 10 minutes of oxidation followed by an air quench. ....	77
Figure 5.18	Micrographs at 250X and 1000X of the surface oxides developed on the 10B, 15Mo5B, and 10Mo5B alloys after a 10°C/min ramp to 1200°C and 10 minutes of oxidation followed by an air quench. ....	78
Figure 5.19	Back scatter micrographs of oxide metal interface developed on the 10B alloy after 10 minutes of oxidation at 900 and 1200°C.....	79
Figure 5.20	Back scatter micrographs of oxide metal interface developed on the 15Mo5B alloy after 10 minutes of oxidation at 900 and 1200°C. A thin layer of CrNbO <sub>4</sub> is observed to form over the Laves phase and solid solution phases at 900°C. ....	80
Figure 5.21	Closer examination of the SiO <sub>2</sub> Nb <sub>2</sub> O <sub>5</sub> oxide mixture developed on the 15Mo5B alloy after 10 minutes of oxidation at 1200°C. The mixture was observed to form from the Nb <sub>5</sub> Si <sub>3</sub> silicide.....	81
Figure 5.22	Back scatter micrographs of oxide metal interface developed on the 10Mo5B alloy after 10 minutes of oxidation at 900 and 1200°C.....	81
Figure 5.23	Schematic representation of rapid oxidation process responsible for transient oxidation behavior indicated by thermal gravimetric results.....	82
Figure 5.24	700°C long term cyclic oxidation results for the 10B alloy. ....	83
Figure 5.25	1000°C long term cyclic oxidation results for the 10B, 15Mo5B, and 10Mo5B alloy. ....	84
Figure 5.26	1300°C long term cyclic oxidation results for the 10B, 15Mo5B, and 10Mo5B alloy..	85
Figure 5.27	1400°C long term cyclic oxidation results for the 10B, 15Mo5B, and 10Mo5B alloy..	86
Figure 5.28	Oxidation products after long term cyclic oxidation at 700°C for (a) 10B, (b) 15Mo5B, and (c) 10Mo5B alloys. ....	86
Figure 5.29	Oxidation products after long term cyclic oxidation at 1000°C for (a) 10B, (b) 15Mo5B, and (c) 10Mo5B alloys. ....	86
Figure 5.30	Oxidation products after long term cyclic oxidation at 1300°C for (a) 10B, (b) 15Mo5B, and (c) 10Mo5B alloys. ....	87
Figure 5.31	Oxide metal interfaces developed for the 10B alloy after long term cyclic oxidation at (a) 1300°C and (b) 1400°C. ....	87
Figure 5.32	XRD spectra collected from oxide products after long term cyclic oxidation at 700, 1000, and 1300°C of the 10B alloy.....	88

Figure 5.33	XRD spectra collected from oxide products after long term cyclic oxidation at 700, 1000, and 1300°C of the 15Mo5B alloy .....	88
Figure 5.34	XRD spectra collected from oxide products after long term cyclic oxidation at 700, 1000, and 1300°C of the 10Mo5B alloy .....	89

## **Chapter 1: INTRODUCTION**

Discovering and developing materials systems capable of offering high strength and stiffness at the highest temperatures possible has always been a fundamental concern of the materials science community. Specifically in the aerospace industry in which current nickel based super alloys are operating within 200°C of their melting points. This has been made possible by advances in both process and design technologies. Such advances have led to the development of internally cooled single crystal components within turbines which are protected by advanced ceramic thermal barrier coatings [1]. A trend can be observed in the contributions each development has made in terms of power produced and turbine rotor inlet temperature as shown in Figure 1.1 [2]. Turbine rotor inlet temperature is the hottest part of the turbine where combustion occurs. A few initial observations can be made from Figure 1.1 which indicate that despite an increase in turbine rotor inlet temperature the amount of specific core power increased deviates farther from the ideal gas-turbine engine relationship leading to lower efficiency, hence the need for advanced high temperature materials systems.

There are many constraints that guide the search for new materials such as melting point, cost, and density to list a few. However, two prevalent approaches can be observed in the studies conducted in the search for these high temperature materials that involve developing either high temperature creep resistance and other related mechanical properties or high temperature oxidation resistance. The latter of which is very important in developing alloys from niobium and molybdenum. Systems that incorporate these two metals potentially represent the next generation of high temperature materials given their high melting points and comparable density to nickel. Unfortunately like most of other refractory metals niobium suffers from catastrophic

oxidation at elevated temperatures. Molybdenum also suffers from catastrophic oxidation. However, volatilization of oxides also leads to mass loss issues.

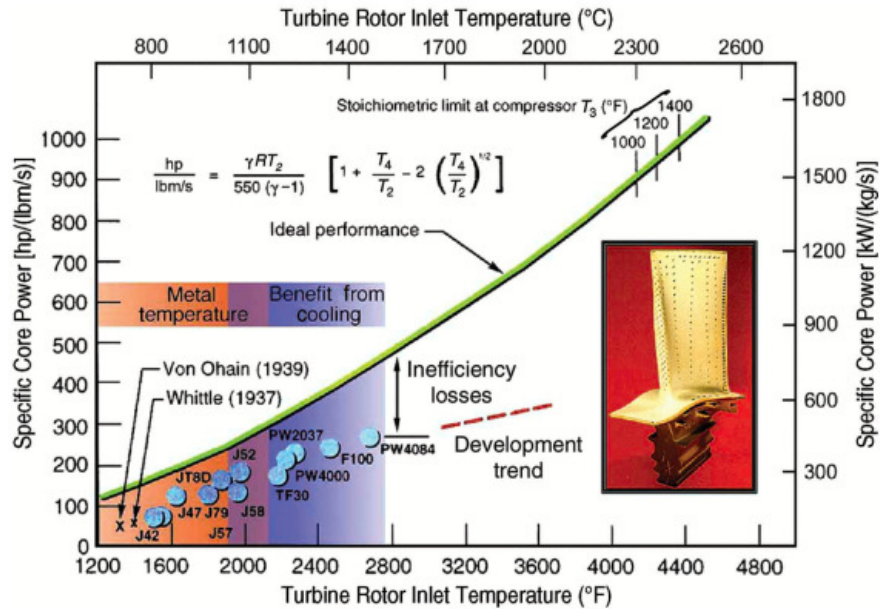


Figure 1.1 Specific power as a function of temperature. Ideal gas-turbine relationship  $T_2$ -turbine rotor inlet temperature,  $T_4$ -turbine exhaust gas temperature, and  $T_3$  represents stoichiometric temperatures, adopted from [2]

Other requirements that need to be satisfied include high melting points, comparable density to that of nickel, and several mechanical properties such as creep resistance and fracture toughness at ambient temperature. Niobium based refractory metal matrix composites are prime candidates to fill this need due to their comparable density to nickel alloys (density of Ni = 8.912g/cm<sup>3</sup> and Nb = 8.57g/cm<sup>3</sup>) and high melting points [3]. However niobium based alloys typically suffer from catastrophic oxidation at high temperatures and pest oxidation at intermediate temperatures [4-6].

Over the years many approaches have been taken to overcome this issue such as alloying niobium to alter oxidation kinetics. Other avenues of research involved the development of complex microstructures with high volume fractions of intermetallic compounds and silicides.

Development of refractory niobium based alloys can be traced as far back as the early 1950s, granting some perspective on the complexity of problems that have been encountered.

Despite these short comings the development of refractory metal alloys capable of operating in aggressive oxidizing environments at temperatures exceeding the operational limit of nickel based super alloys (1150°C) is still needed. Specifically in the aerospace industry where the development of an alloy capable of operating at 1300°C without any auxiliary cooling equipment could result in 50% more power output from turbo jet engines [7].

## **1.1 JUSTIFICATION**

Recent developments in the Mo-Si-B system have led to the development of borosilicate glass layers on molybdenum alloys. These glass layers provide some degree of oxidation protection. However there are still material loss issues associated with the formation and subsequent volatilization of molybdenum oxides. Limited efforts have been made to explore the possibility of similar developments in Nb based alloy systems. It will be the focus of this research to examine the oxidation behavior of several alloys from the Nb-Mo-Cr-Si-B system as well as the influence different silicon, molybdenum, and boron concentrations have on the scale morphology and oxidation kinetics.

Several alloys have been examined in preliminary studies. Compositions are listed in Table 1.1. Preliminary findings will be summarized in a later section along with what major contributions each made to the development of the final three alloys developed in this study. As cast microstructure, oxide scale morphology, and oxidation kinetics were compared to determine what characteristics of each composition provided the best oxidation resistance. These alloy systems attempt to combine several of the benefits afforded by intermetallic phase, silicides, and the possible formation of a protective borosilicate glass layer.

Table 1.1 Preliminary experimental alloy compositions

Alloy	Composition (% at.)						Composition (% weight)					
	Nb	Cr	Ti	Mo	Si	B	Nb	Cr	Ti	Mo	Si	B
20Ti	40	0	20	20	15	5	52.578	0.000	13.544	27.153	5.960	0.765
25Cr	40	25	0	20	15	0	50.518	17.671	0.000	26.084	5.727	0.000
25Cr5B	35	25	0	20	15	5	46.816	18.715	0.000	27.626	6.065	0.778

All of these oxidation enhancing mechanisms have been previously studied or developed in the pursuit of a niobium based refractory alloys. Each generation of alloys contributed to the development and course this project has followed in the search of a new high temperature materials system. However, there still remain several aspects of this alloy system that remain to be explored, in particular the effects silicon to boron ratios might play on the development of the oxide scale. Silicon to boron ratios were studied to a small extent in the Mo-Si-B system but have not been explored in the Nb-Mo-Cr-Si-B alloy system. An understanding of what effects boron to silicon ratios have on the oxidation behavior of the Nb-Mo-Cr-Si-B alloy system warrants this research. This would also contribute to the overall understanding of the oxidation behavior of the Nb-Mo-Cr-Si-B alloy system.

## 1.2 REFERENCES

1. N. P. Padture, M. Gell, E. H. Jordan: *Science*, 2002, vol.296, pp. 280- 284.
2. Dimiduk D.M. and Perepezko J.H. *MRS Bulletin*, 2003, vol. 28, pp. 639-645.
3. *CRC Handbook of Chemistry and Physics*. Ohio: CRC Press, 1995.
4. Subramanian P.R., Mendiratta M.G., Dimiduk D.M., and Stucke M.A. *Mater. Sci. Eng., A*, 1997, vol. 239, pp. 1-13.
5. Bewlay B.P., Lewandowski J.J., and Jackson M.R. *JOM*, 1997, vol. 49, pp. 45.
6. Bewlay B.P., Jackson M.R., Zhao J.C. and Subramanian P.R. *Metall. Mater. Trans. A*, 2003, vol. 34, pp. 2003-2043.
7. Perepezko J.K. *Science*, 2009, vol. 326, pp. 1068-1069.

## Chapter 2: LITURATURE REVIEW

### 2.1 REFRACTORY METALS

The term “refractory metal” is often associated with a very specialized application whether it is in the lining of a nuclear reactor or as a structural component in a next generation aerospace engine. There are several prerequisites a metal must meet before it is referred to as a refractory metal. Of those the most widely accepted is that the metal must have a melting point and chemical resistance surpassing those of typical stainless steel, cobalt or nickel based alloys [1]. Stricter definitions of the term “refractory metal” require the metal to have a melting temperature above 2200°C and have a body centered crystal structure. There is an additional definition requiring that the ratio of the melting point of the metal and of its oxide be less than one [2]. Typically though despite these definitions there are six elements that are often referred to as refractory metals those being molybdenum, niobium, tantalum, rhenium (even though it is hexagonal closed packed), and vanadium. Select properties of refractory materials are presented in Table 2.1 nickel is included in this table for comparison purposes.

Table 2.1 Select physical properties of refractory metals and nickel for comparison.

Element	Density	Crystal Structure	Melting Point °C
V	6.11	BCC	1910
Ni	8.91	FCC	1455
Nb	8.57	BCC	2477
Mo	10.28	BCC	2623
Ta	16.69	BCC	3017
Re	21.02	HCP	3186

## 2.1 OXIDATION OF PURE NIOBIUM

The oxidation of pure niobium has been studied extensively to reveal complex oxidation behaviors that can be broken down into several different partial processes. The generally accepted oxidation behavior of pure niobium as presented by Kofstad [3] involves oxygen saturation of the niobium lattice which leads to the formation of metal oxides. As temperature increases the amount of time needed to saturate the metal matrix with oxygen becomes shorter beyond 500°C. Metal oxides formed above 600°C include NbO and NbO<sub>2</sub> often found growing along grain boundaries. At temperatures exceeding 650°C the formation of Nb<sub>2</sub>O<sub>5</sub> takes place in several steps involving the saturation of the lattice with oxygen followed by the nucleation of NbO then NbO<sub>2</sub> and finally Nb<sub>2</sub>O<sub>5</sub>. It must also be noted that at 700°C, Figure 2.1, a maximum in linear rate constants of oxidation has been observed and corresponds to the rapid oxidation of NbO<sub>2</sub> to form non protective Nb<sub>2</sub>O<sub>5</sub>.

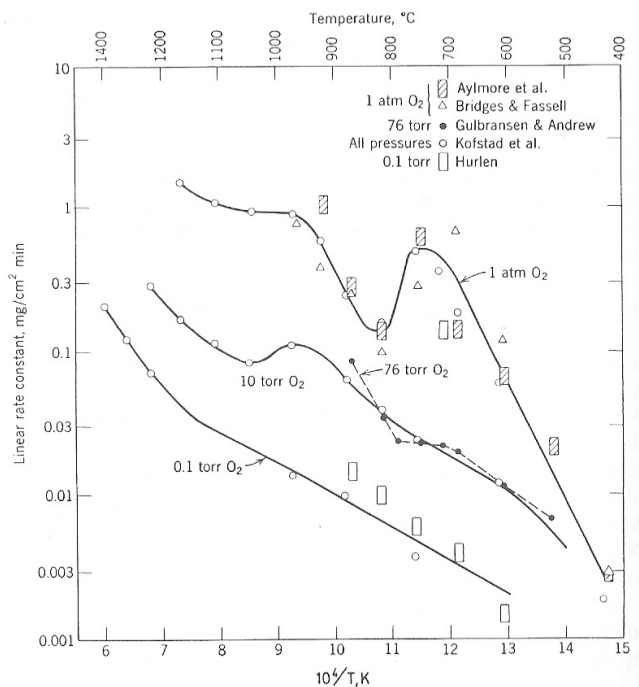


Figure 2.1 Linear rate constants for the oxidation of niobium as a function of temperature, adopted from Kofstad [3]



Also worth noting is the polymorphic nature of  $\text{Nb}_2\text{O}_5$ , several forms have been observed, a low temperature form often termed  $\gamma$ -  $\text{Nb}_2\text{O}_5$  transforms to  $\alpha$ -  $\text{Nb}_2\text{O}_5$  at temperatures between 800 and 900°C. Various other transformations of  $\text{Nb}_2\text{O}_5$  have been reported many of which are irreversible and often are not detectable by calorimetry [4]. Very little data is available about the oxidation of niobium above 1200°C, due to rapid reaction rates. In some cases niobium can ignite in pure oxygen with a pressure of 1 atm at temperatures exceeding 1200°C. This type of behavior is not uncommon since a recent study of stainless steels and other refractory alloys revealed similar results as the temperature was increased lower oxygen pressures were required to maintain self-sustained combustion. [5]

Oxide scale morphology and kinetics of pure niobium have been shown, to be temperature dependent as a result of the various partial processes previously discussed. At elevated temperatures, the scale exclusively transforms to  $\text{Nb}_2\text{O}_5$ , and at temperatures near 600°C a layered structure develops. Oxygen tracer studies confirmed the general oxidation behavior presented by Kofstad,  $\text{Nb}_2\text{O}_5$  was observed growing on a layer of NbO and  $\text{NbO}_2$  at 600°C. [6] An oxygen isotope was used to observe the diffusion progression through the oxide scale in this case  $^{18}\text{O}$  was used. At temperatures exceeding 700°C the oxidation kinetics observed were par linear, as a result of a dense  $\text{Nb}_2\text{O}_5$  oxide scales growing to a critical thickness and then spalling off and cyclically repeating. Oxygen was found to be the most mobile species in the  $\text{Nb}_2\text{O}_5$  scale and to move uniformly through the scale without any preference for grain boundaries according to the distribution of the  $^{18}\text{O}$  in the scale. The morphology of the high temperature  $\text{Nb}_2\text{O}_5$  oxide scales developed was examined in detail by Valot et al [7]. Oxide spalling was attributed to compressive stresses developing in the oxide scale and tensile stresses developing in the metal. Cracks formed in the oxide scale typically due to the accelerated oxidation at the edges of the

samples. Accelerated oxidation was attributed to heat buildup, which resulted in increased diffusion rates leading to thicker oxide scales which resulted in a curvature of the oxide where cracks would eventually form.

Unfortunately very little detailed data about oxide morphology and kinetics is available on niobium based alloy systems. However there is some information available on a few key systems such as Nb-Si, Nb-Cr, as well as limited information on various other important ternary systems such as Nb-Si-Cr, Mo-Si-B, Nb-Si-B, and Nb-Mo-Si-B. Molybdenum systems are worth mentioning due to the large amount of data available and the concepts may be useful in understanding the oxidation kinetics of niobium based alloys. The Mo-Si-B system has been under development since the early 90s and there are hopes that similar developments can be made on niobium based systems.

## **2.2 LAVES PHASES**

The term Laves phase is often used to describe a group of related intermetallic compounds,  $AB_2$ , having either an  $MgZn_2$  type hexagonal structure,  $MgCu_2$  type cubic structure, or an  $MgNi_2$  type hexagonal structure [8]. The C14  $MgZn_2$  hexagonal type structure belongs to the  $P6_3/mmc$  space group and contains four A atoms and eight B atoms. In this structure the smaller B atoms are located at the corners of tetrahedra that are joined in an alternating manner at the base and point to point. The A atoms occupy the areas enclosed by the B atom tetrahedra, each A atom is coordinated to four other A atoms. The tetrahedral views of each form of Laves phase are shown in Figure 2.2. The C15  $MgCu_2$  type cubic structure belongs to the  $Fd3m-O_h$  space group and contains eight A atoms and sixteen B atoms. The structure can be thought of as two interpenetrating lattices of both A and B atoms where the B atoms lie at the corners of the tetrahedra connected at the points and the A atoms occupy the resulting enclosed structure created by the B atom tetrahedra. The C36  $MgNi_2$  type hexagonal structure belongs to the  $P6_3/mmc$  space group and contains eight A atoms and sixteen B atoms. The B atoms are located

at the corners of tetrahedra however the arrangement of the tetrahedra joining is a mixture of the C14 and C15 structures. The arrangement of the A atoms in the three Laves phase lattices are presented in Figure 2.3.

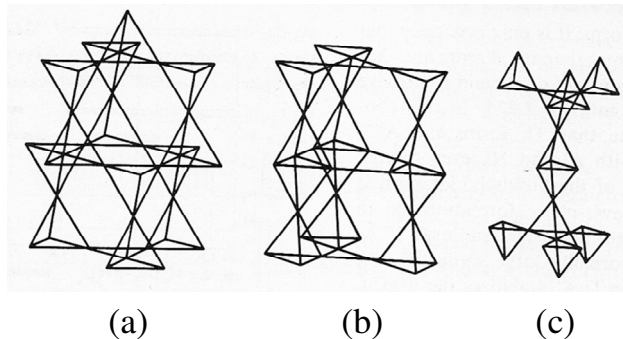


Figure 2.2 Tetrahedra formed by the B atoms in the three different Laves structures (a) C15  $\text{MgCu}_2$ , (b) C14  $\text{MgZn}_2$ , and (c) C36  $\text{MgNi}_2$ . Adopted from [8]

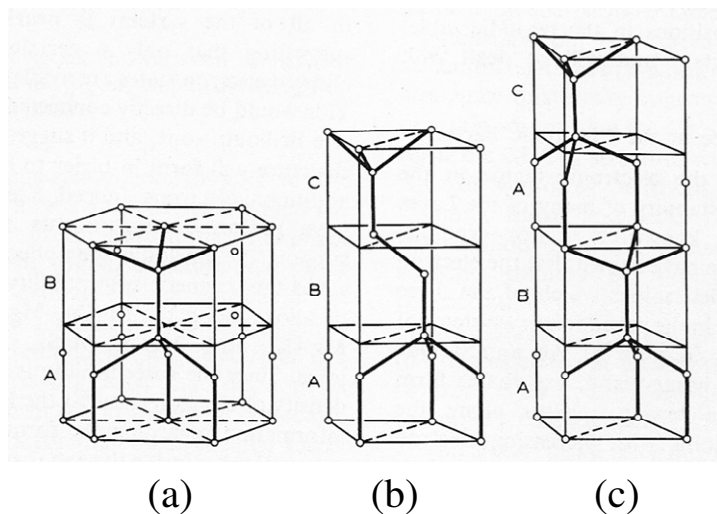


Figure 2.3 Arrangement of the A atoms in the three Laves phase lattices (a) C14  $\text{MgZn}_2$ , (b) C15  $\text{MgCu}_2$ , and (c) C36  $\text{MgNi}_2$ . Adopted from [8]

The atomic size factor was hinted at early on in this section. A determining factor in the formation of Laves phases was found to be related to the atomic size of the constituent atoms. An ideal atomic radii ratio has been determined based on studies of hard sphere packing models to be,  $r_A/r_B$ , approximately 1.255. Actual Goldschmidt radii of pure elements known to form Laves phases found  $r_A/r_B$  varies between 1.05 and 1.68. It was postulated by various authors that the

$r_A/r_B$  determined what type of Laves phase structure would form, however others have indicated that valence electron to atom ratios determine the Laves phase structure [9-10].

Of the many known Laves phases  $NbCr_2$  is of significant importance to this study due to the many desirable physical and mechanical qualities [9].  $NbCr_2$  C15 Laves phase has a melting point of  $1730^\circ\text{C}$  and a density of  $7.7\text{g/cm}^3$  and offers some oxidation resistance up to  $1100^\circ\text{C}$ . Interestingly when silicon is introduced into the binary Nb-Cr system a C14 type structure can be obtained. Silicon was observed to occupy B atom positions reducing the effective electron concentration in the structure allowing for a stable C14 phase [11]. Additionally by introducing substitutional soluble atoms into the A and or B lattice sites the Laves phase deformability may be enhanced [12].

### **2.3 OXIDATION OF Nb-Cr ALLOYS CONTAINING LAVES PHASE**

Nb-Cr alloys contain various amounts of Laves phase  $NbCr_2$  and a solid solution whether it be Cr based or Nb based and are often the foundation of the more complex alloy systems under development. An understanding of the kinetics of Laves phase alloys needed before kinetics and oxide scale structures can be discussed or characterized. Brady et al. studied the mechanical properties of Laves phase reinforced composites and reported the scale formed on the alloy in various layers [13]. The layer closest to the oxide metal interface was composed largely of  $CrNbO_4$  while above that at the oxide air interface a layer of loosely adherent ruffled  $Cr_2O_3$  was formed. Nitrogen embrittlement was also observed by Brady, it is a well-known and documented occurrence in pure chromium [14], however in the Laves phase reinforced composites it was found that not only did the solid solution become embrittled but the Laves phase did so as well. The embrittlement of the Laves phase, however, is of little consequence given its inherently high hardness and brittleness. Zheng et al. reported the development of similar layered structures on mechanically alloyed hot pressed Laves phase [15, 16]. The molar

volume change from  $\text{NbCr}_2$  to  $\text{Cr}_2\text{O}_3$  and  $\text{Nb}_2\text{O}_5$  was also reported and indicated to be nearly 376% leading to the development of internal stresses within the oxide scales. Coupled with mismatches in thermal expansion coefficients these stresses were indicated to be responsible for the oxide scale spallation. In this case the solid solution was niobium based and no mention of nitridation was made. However, a correlation between the growth of the ruffled loosely adherent chromium scale and the diffusion of chromium is made. The exclusive formation of  $\text{Cr}_2\text{O}_3$  over the  $\text{CrNbO}_4$  oxides implies that chromium ions diffuse outwards at a much higher rate than niobium ions. This kind of outward diffusion has been observed in the oxidation of pure chromium in early studies as well as by subsequent oxygen isotope tracer studies which report that newly developed  $\text{Cr}_2\text{O}_3$  occurs near the oxide air interface indicating the outward diffusion of chromium ions took place [17-19].

## **2.4 OXIDATION OF MO-SI-B**

$\text{Mo}_5\text{Si}_3$  and  $\text{Mo}_2\text{Si}$  are two silicides of interest in the Mo-Si system.  $\text{Mo}_5\text{Si}_3$  suffers from catastrophic oxidation and mass loss at elevated temperatures ( $T > 800^\circ\text{C}$ ) but provides excellent creep resistance.  $\text{MoSi}_2$  offers oxidation resistance up to temperatures as high as  $1700^\circ\text{C}$ , but suffers from pest oxidation at intermediate temperatures. [20] Boron additions were found [21, 22] to increase the oxidation resistance of molybdenum silicides, and pest oxidation resistance resulting in a large research effort focused on studying the Mo-Si-B system.  $\text{Mo}_5\text{Si}_x\text{B}_x$  type phases develop a layer of borosilicate glass upon oxidation resulting in high oxidation resistance. [23-27] Additions of ductile phases, typically molybdenum solid solution [28], are required to enhance the fracture toughness but result in unacceptable material recession typically caused by the formation and subsequent volatilization of  $\text{MoO}_3$  at above  $700^\circ\text{C}$ . [29]

## 2.5 OXIDATION OF Nb-MO-Si

The Nb-Si-Mo alloys were examined by Chattopadhyay et al. [30] The authors determined that the oxidation behavior was dependant on the hypo-, hyper-eutectic character of the alloy at intermediate temperatures due to the accelerated oxidation of  $(\text{Nb},\text{Mo})_5\text{Si}_3$  in hypereutectic alloys. Molybdenum was found to increase oxidation resistance at temperatures exceeding  $1000^\circ\text{C}$  by increasing sinterability of the oxide scale effectively lowering the porosity of the scale. By reducing the porosity the rate at which oxygen could diffuse into the base metal was also lowered resulting in the higher activity of silicon which leads to the development of a layer of  $\text{SiO}_2$ . A characteristic multi layer oxide scale is developed on samples which consist of dispersed  $\text{Nb}_2\text{O}_5$  particles in a borosilicate glass matrix when boron is added. However, the beneficial effects of the borosilicate glass may be reduced due to an increased viscosity caused by dispersed  $\text{Nb}_2\text{O}_5$  oxide particles. [31-32]

## 2.6 OXIDATION OF Nb-Si-B

An attempt was made to study the oxidation behavior of the alloys from Nb-Si-B system to determine whether  $\text{Nb}_5\text{Si}_x\text{B}_x$  phases may offer similar oxidation resistance to their molybdenum counterparts. Oxidation resistance of  $\text{Nb}_5\text{Si}_3\text{B}_2$  was found to be superior to undoped  $\text{Nb}_5\text{Si}_3$  as reported by Murakami et al. [33] Unlike the  $\text{Mo}_5\text{Si}_x\text{B}_x$  type silicides which develop volatile  $\text{MoO}_3$  the development of a continuous borosilicate glass layer from  $\text{Nb}_5\text{Si}_3\text{B}_2$  type silicides was not possible due to the development of non-volatile  $\text{Nb}_2\text{O}_5$ . On a side note Behrani et al. attempted to promote the volatilization of  $\text{Nb}_2\text{O}_5$  through a chlorination treatment to develop a continuous layer of borosilicate glass [34]. The treatments resulted in limited success and only marginal gains in oxidation resistance.

## 2.7 OXIDATION OF Nb-Cr-Si

The Nb-Cr-Si system has also been examined and often, the alloys with the best oxidation resistance had microstructures containing large volume fractions of silicides ( $\text{Nb}_5\text{Si}_3$ ) and Lave phases ( $\text{NbCr}_2$ ). It was determined by Chan [35] that the oxidation resistance of multi-phase alloys containing solid solution,  $\text{NbCr}_2$  and  $\text{Nb}_5\text{Si}_3$  depends on their volume fractions. Compositions with high volume fractions of  $\text{NbCr}_2$  and  $\text{Nb}_5\text{Si}_3$  were observed to have higher oxidation resistance than alloys with higher concentrations of solid solution. Higher concentrations of chromium in the solid solution phase as well as higher volume fractions of both silicides and Laves phases resulted in improved oxidation resistance which has also been reported by several other authors [36-38].

## 2.8 OXIDE VOLATILIZATION

Volatilization of refractory metal oxide layers intended to provide some measure of oxidation resistance can have extremely detrimental effects on refractory metals. Those effects include modification of oxidation kinetics, material loss/metal recession, and pitting of the sample as well as localized modification of alloy chemistry near oxide metal interfaces. Volatilization of chromium scales has been studied due to its abundant use in refractory alloys. Caplan et al. [39] concluded that volatilization occurred only in oxidizing environments by heating pure  $\text{Cr}_2\text{O}_3$  samples to 1000-1200°C and passing oxygen over pellets after which a weight loss was observed, however no weight loss observed with pure argon. Oxidation kinetics of alloys that form adherent protective  $\text{Cr}_2\text{O}_3$  scales were shown to transform from parabolic to linear, transitions in the kinetics are often called par linear, after the scale has grown to a critical thickness [40]. Pujilaksono et al. studied the effects of moisture on the oxidation of chromium and reported similar shifts in oxidation kinetics due to the evaporation or volatilization of

protective  $\text{Cr}_2\text{O}_3$  oxide scales [41]. The presence of moisture was found to result in a layered oxide structure, one protective and one non-protective, and evaporation of the  $\text{Cr}_2\text{O}_3$  scale was accelerated by the energetically favorable conversion to a  $\text{CrO}_2(\text{OH})_2$ .

The volatilization of oxide products formed on commercial nickel and iron based super alloys was studied by Zaplatynsky at  $1200^\circ\text{C}$  in static air [42]. It was determined that elements preferentially lost from the oxide scales included tungsten, molybdenum, niobium, manganese, and chromium. Microstructural cross-sections of oxide metal interfaces revealed pitting and localized modification of alloy chemistry in many cases resulting in depletion of alloying element. Elements that were not detected in the oxide vapor deposits were silicon and aluminum. Alloy that formed spinels and protective alumina scales were found to be less susceptible to oxide volatilization.

Volatilization of molybdenum has also been studied at various temperatures and oxygen pressures. Volatilization of  $\text{MoO}_3$  has been reported to occur at temperatures above  $600^\circ\text{C}$  in air. As previously mentioned molybdenum based alloys although promising suffer from metal recession which limits their applications. Several studies have investigated the volatilization of  $\text{MoO}_3$ . Gulbransen et al. studied the oxidation of molybdenum and volatilization of  $\text{MoO}_3$  in a temperature range from  $550$  to  $1704^\circ\text{C}$  at pressures between  $5$  to  $76$  Torr ( $0.066$  to  $0.1$  atm) [43]. At temperatures above  $800^\circ\text{C}$  the volatilization of  $\text{MoO}_3$  occurred as fast as  $\text{MoO}_3$  was grown on the surface. A more recent study conducted by Smolik et al. on the volatilization and re-deposition of oxide scales formed on a molybdenum based alloy termed TZM alloy indicated other non-stoichiometric oxides might change the volatilization process at temperatures between  $600$  and  $800^\circ\text{C}$  . [44]



## 2.9 CHARACTERIZATION OF OXIDATION CURVES

Commonly encountered rate equations and kinetics can typically be described as logarithmic, linear, parabolic, or in some cases a combination [3]. Logarithmic reactions typically have a high initial rate of weight gain followed by a decrease to lower weight gain rates in some cases the rate of weight gain can be negligible. The equations needed to describe both logarithmic and inverse logarithmic oxidation curves are provided below. Figure 2.4 provides a visual representation of typical logarithmic and inverse logarithmic oxidation curves.

Logarithmic rate equation:

$$x = k_{\log} \log(t + t_o) + A$$

Where  $x$  is weight gain,  $t$  is time, and  $A$  is a constant.

$k_{\log}$  is the logarithmic rate constant

Inverse Logarithmic rate equation:

$$\frac{1}{x} = B - k_{\ln} \log(t)$$

Where  $x$  is weight gain,  $t$  is time, and  $B$  is a constant.

$k_{\ln}$  is the inverse logarithmic constant

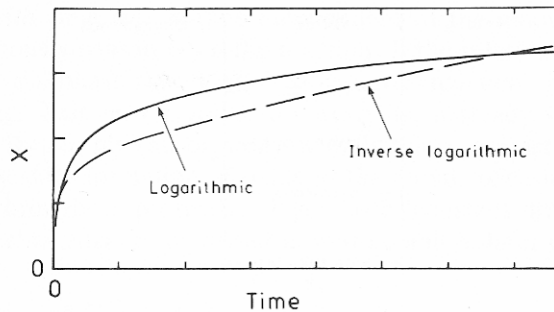


Figure 2.4 Illustration of a typical logarithmic and inverse logarithmic oxidation curves, adopted from Kofstad [3]

Parabolic rate reactions typically describe high temperature oxidation curves, and signify that a thermal diffusion process is rate limiting. The rate limiting mechanisms typically involve

the uniform diffusion of one or more reactants through a growing compact scale. A typical parabolic oxidation curve can be described by the parabolic rate equations provided below, the differential version is also listed.

Parabolic rate equation:

$$x^2 = 2k_p' t + C = k_p t + C$$

Differential integral form:

$$\frac{dx}{dt} = \frac{k_p}{x}$$

Where  $k_p$  and  $k_p'$  are parabolic rate constants and  $C$  is a constant.

Linear oxidation indicates constant weight gain with time and indicates that the rate of oxidation is not influenced by any previous amount of gas or metal consumed in the reaction. Linear oxidation may also indicate that the rate limiting mechanism can be a reaction at a phase boundary whether it is the oxide air interface or the oxide metal interface. Linear oxidation may also occur when oxygen is diffused through a continuous layer of oxide with uniform thickness. Figure 2.5 shows typical linear and parabolic oxidation curves. Linear oxidation curves can be described by the linear rate equations provided below.

Linear rate equations:

$$x = k_l t + C$$

$$\frac{dx}{dt} = k_l$$

Where  $x$  is weight gain,  $t$  is time,  $C$  is a constant, and  $k_l$  is a linear oxidation rate constant.

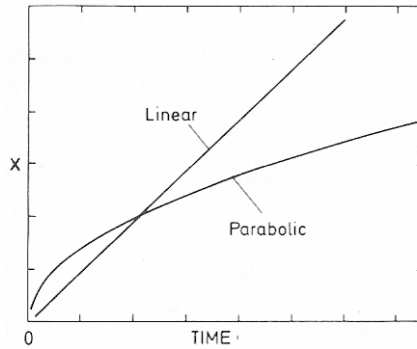


Figure 2.5 Representation of typical linear and parabolic oxidation curves adopted from Kofstad [3]

## 2.10 REFERENCES

1. Briant C.L. *JOM*, 2000, vol. 52, pp. 36.
2. Lipetzky P. *JOM*, 2002, vol. 54, pp. 47-49.
3. Kofstad, Per. High Temperature Corrosion. New Yourk: Elsevier Applied Science, 1988.
4. T. Hurlen. *Journal of the Institute of Metals*, 1960, vol. 89, pp. 273-280.
5. Michael J. Slockers and Rosemary Robles-Culbreth. *Journal of ASTM International*, 2006, vol. 9, pp. 1-18.
6. J.S. Sheasby and W. W. Smeltzer. *Oxidation of Metals*, 1981, vol. 15, pp. 215-229.
7. C. Valot, D. Ciosmak, and M. Lallemand. *Oxidation of Metals*, 1994, vol. 41, pp. 235-250.
8. Westbrook J.H. *Intermetallic Compounds*. New York: Wiley, 1967.
9. Chu F., Thoma D.J., Kotula P.G., Gerstl S, Michell T.E., Anderson I.M., and Bentley J. *Acta Mater*, 1998, vol. 46, pp. 1759-1769.
10. Stein F., Palm M., and Sauthoff G. *Intermetallics*, 2005, vol. 13, pp. 1056-1074.
11. Thoma D.J. and Perepezko J.H. *J. Alloys Compd.*, 1995, vol. 224. Pp. 330-341.
12. Linvingston J.D., and Hall E. L. *J. Mater. Res.*, 1990, vol. 5, pp. 5-8.
13. T. Liu and R. Bautista. *Oxidation of Metals*, 1979, vol. 15, pp. 277-268.

14. B. Pujilaksono, T. Jonsson, M. Halvarsson, I. Panas, J. Svensson, and L. Johansson. *Oxid Met*, 2008, vol. 70, pp. 163-188.
15. I. Zaplatynsky. *Oxidation of Metals*, 1977, vol. 11, pp. 289-305.
16. E. A. Gulbransen, K. F. Andrew, and F. A. Brassart. *Journal of the Electro Chemical Society*, vol. 9, pp. 952-959.
17. G. R. Smolik, D. A. Petti, and S.T. Schuetz. *Journal of Nuclear Materials*, 2000, vol. 283, pp. 1458-1462.
18. M.P. Brady, J.H. Zhu, C.T. Liu, P.F. Tortorelli, and L.R. Walker. *Intermetallics*, 2000, vol. 8, pp. 1111-1118.
19. L. Royer, X. Ledoux, S. Mathieu, and P. Steinmetz. *Oxidation of Metals*, 2010, vol. 74, pp. 79-92.
20. M. Akinc, M. K. Meyer, M. J. Kramer, A. J. Thom, J. J. Huebsch, and B. Cook: *Materials Science and Engineering A*, 1999, vol. 261, pp. 16-23 .
21. M. K. Meyer, M. Akinc: *Journal of the American Ceramic Society*, 1986, vol. 79, pp. 938-944.
22. M. K Meyer, M. Akinic: *Journal of the American Ceramic Society*, 1996, vol. 79, pp. 2763-2766 .
23. M. K. Meyer, A. J. Thom, M. Akinc: *Intermetallics*, 1999, vol. 7, pp. 153-162 .
24. K. Ito, T. Murakami, K. Adachi, and M. Yamaguchi: *Intermetallics*, 2003, vol. 11, pp. 763-772.
25. M. G. Mendiratta, T. A. Parthasarathy, D. M. Dimiduk: *Intermetallics*, 2002, vol. 10, pp. 225-235.
26. V. Supatarawanich, D. R. Johnson, C. T. Liu: *Materials Science and Engineering A*, 2003, vol. 344, pp. 328-339.
27. S. Paswan, R. Mitra, S. K. Roy: *Materials Science and Engineering A*, vol. 424, pp. 251-265.

28. J.H. Schneibel, R. O. Ritchie, J.J. Kruzic, and P. F. Tortorelli: Metallurgical and Materials Transactions A, vol. 36, pp. 525-531.
29. G. R. Belton, A. S. Jordan: The Journal of Physical Chemistry, vol. 69, pp. 2065-2071.
30. K. Chattopadhyay, R. Mitra, K. K. Ray: Metallurgical and Materials Transactions A, 2008, vol. 39, pp. 577-592.
31. Y. Liu, M. J. Kramer, A. J. Thom, M. Akinc: Metallurgical and Materials Transactions A, 2006, vol. 36, pp. 601-607.
32. V. Behrani, A. J. Thom, M. J. Kramer, M. Akinc: Intermetallics, vol. 14, pp. 24-32.
33. T. Murakami, C. N. Xu, A. Kitahara, M. Kawahara, Y. Takahashi, H. Inui, M. Yamaguchi: Intermetallics, 1999, vol. 7, pp. 1043-1048.
34. V. Behrani, A. J. Thom, M. J. Kramer, and M. Akinc. Metallurgical and Materials Transactions A, 2005, vol. 36A, pp. 609-615.
35. K. S. Chan: Metallurgical and Materials Transactions A, vol. 35, pp. 589-597.
36. M. D. Gonzales, S.K. Varma. Supplemental Proceedings: Volume I: Materials Processing and Properties TMS, 2008, pp. 455-460.
37. J. Ventura, B. Portillo, S. K. Varma, R. N. Mahapatra: ECS Transactions, 2009, vol. 16, pp. 157-166.
38. H. Zheng, S. Lu, Z. Jianye, and L. Guangming. Int. Journal of Refractory Metals & Hard Materials, 2009, vol. 27, pp. 659-663.
39. D. Caplan and M. Cohem. Journal of the Electrochemical Society, 1961, vol. 108, pp. 438-442.
40. H. Zheng, S. Lu, Q. Su, F. Quan. *International Journal of Refractory Metals & Hard Materials*, 2008, vol. 26, pp. 1-4.
41. H. Zheng, S. Lu, Z. Jianye, and L. Guangming. *International Journal of Refractory Metals & Hard Materials*, 2009, vol. 27, pp. 659-663.
42. K.P. Lillerud and P. Kofstad. *Journal of the Electrochemical Society*, 1980, vol 127, pp. 2397-2410.

43. P. Kofstad and K.P. Lillerud. *Journal of the Electrochemical Society*, 1980, vol 127, pp. 2410-2419.
44. M. Skeldon, J.M. Calvert, and D.G. Lees. *Oxidation of Metals*, 1987, vol. 28, pp. 109-125.

## Chapter 3: Experimental Procedure

### 3.1 SAMPLE PREPARATION

Alloys were fabricated by the Ames laboratory of Iowa State University by a triple arc melt method on a water cooled copper hearth under a high purity argon atmosphere. Niobium, molybdenum, and chromium metals used were of 99.9% minimum purity. The boron and silicon used were 99.5% in purity. 5 – 50 gram alloy buttons were melted several times and then machined into 5x5x5 mm cubes by electronic discharge machining (EDM). Samples were polished to a 600 grit finish with silicon carbide emery paper, and then ultrasonically cleaned in ethanol for 15 minutes. Surface area was calculated and samples were weighed before oxidation. Several compositions were examined in the course of this study all are listed in table 4.1 in both atomic and weight percent.

Table 3.1 Compositions of experimental alloys

Alloy	Composition (% at.)					Composition (% weight)				
	Nb	Cr	Mo	Si	B	Nb	Cr	Mo	Si	B
10Mo 5B	45	25	10	15	5	60.456	18.797	13.873	6.092	0.782
15Mo 5B	35	25	15	20	5	49.220	19.676	21.783	8.502	0.818
10B	30	25	20	15	10	42.648	19.891	29.361	6.446	1.654

### 3.2 SHORT TERM OXIDATION

Short term oxidation experiments were carried out in air in computer controlled furnaces. Samples were placed in dry covered crucibles and then heated at a rate of 10°C/min to designated temperatures and held there for 24hrs after which samples were allowed to furnace cool and weighed again to determine the weight change due to oxidation. Auxiliary thermocouples were used to monitor the temperature of the crucible. Adjustments were made to keep the temperature within 5°C of experiment temperatures.

### **3.3 CYCLIC OXIDATION**

Long term cyclic experiments were carried out in air in computer controlled furnaces. Samples were placed in dry covered crucibles and then ramped at 10°C/min to designated temperatures and held for 24 hours then allowed to furnace cool. After furnace cooling the samples were weighted and then optically examined in the crucible for changes in the sample morphology. The samples were then reintroduced into a cool furnace for another 24 hour cycle of oxidation. The samples were cycled at 24 hour intervals till a total of 168 hours had been achieved.

### **3.4 OXIDE SCALE DEVELOPMENT**

Oxide scale development studies were carried out on select alloys of interest in air in computer controlled furnaces. Polished samples with dimensions of 5x5x2.5mm were placed in dry covered crucibles and ramped to 10°C/min to a designated temperature and held for 15 minutes. The samples were then removed from the furnace and air quenched to conserve high temperature structures.

### **3.5 THERMAL GRAVIMETRIC STUDIES**

Oxidation kinetics were characterized by thermo gravimetric studies, carried out in a LabSys evo. Samples were cut in half (2.5x5x5mm) using a diamond wheel in a liquid cooled precision saw. Samples were then prepared in the same fashion as the short term oxidation samples were. Samples were ramped at 30°/min instead of 10°/min and isothermal data was collected. Samples were held in an alumina crucible with air allowed into the chamber. Data was collected from the scale every 15 seconds for the duration of the oxidation experiment.

### **3.6 X-RAY DIFFRACTION ANALYSIS**

Oxide scales that were not thick enough to be removed without damaging the remaining metal were characterized in situ. Oxide products that had either spalled or were the result of pest oxidation were ground as finely as possible in a clean pestle and mortar prior to XRD analysis. XRD analysis was carried out on the D8 Discovery using a scan rate of 5°/min, the 0.8mm slit on



the x-ray source, and an 8mm slit on the detector. It was determined by trial and error that this combination gave the best results, acceptable resolution and intensity. For calibration purposes powder oxides were laced with  $\text{Al}_2\text{O}_3$ , the polymer mounting media was also laced with  $\text{Al}_2\text{O}_3$ .

### **3.7 SCANNING ELECTRON MICROSCOPY**

To expose the oxide metal interface when a sample did not spall or pest oxidize samples were mounted in an epoxy resin and then sectioned in half by a liquid cooled precision diamond saw. The halves were remounted in epoxy resin and polished to reveal the oxide metal interface for SEM examination. This was done in order to ensure that a true cross-section of the oxide metal interface could be observed. Simply polishing the oxide off one surface of the sample would not guarantee that a true cross-section was being observed since it was unknown whether or not any sort of micro structural changes had taken place due to localized changes in chemistry due to the oxidation process. The mounted samples were polished to 1200 grit silicon carbide emery paper and then ultrasonically cleaned in ethanol. After grinding at 600 grit silicon carbide had been completed the samples were ultrasonically cleaned to remove any loose carbide that may have remained on the sample. No alumina slurries or diamond pastes were used to prevent any contamination of the oxide scale. Polished samples were then sputter coated with gold to eliminate charging of the sample. SEM characterization was carried out on the samples in BSE (back scatter mode) as well as EDS (electron dispersion spectroscopy) at 20Kev and 20 $\mu\text{A}$  at a working distance of 15mm. To ensure reasonable accuracy of the EDS analysis the equipment was routinely calibrated with an aluminum and copper sample while the back scatter detector was inserted.

## Chapter 4: Preliminary Studies

Preliminary studies will be presented in this section. Initial studies were centered on additions of titanium instead of chromium to the Nb-Mo-Si-B system. However, initial evaluations of additions to the alloy system indicated that chromium provided the best potential oxidation resistance. Modifications to the composition of the alloy were made to increase both the amounts of laves phase and silicides that formed while reducing the amount of primary solid solution.

### 4.1 OXIDATION BEHAVIOR OF Nb-Mo-Si-B WITH TITANIUM ADDITIONS

Additions of titanium to the Nb-Mo-Si-B system had not been explored and it was determined that the possible development of a layer of  $\text{TiO}_2$  merited this study. Research available in literature had been conducted on niobium based alloys but often incorporated additions of aluminum as well which were found to be detrimental to oxidation resistance and lower the overall melting point of the resulting alloys. Two oxides containing titanium were observed to develop on niobium based alloys i.e.  $\text{TiO}_2$  at high concentrations of titanium and  $\text{TiNb}_2\text{O}_7$  for alloys containing high concentrations of niobium [1,2]. It was also shown that the simultaneous development of both of these oxides resulted in parabolic oxidation kinetics [1]. The development of  $\text{Ti}_5\text{Si}_3$  in the alloy and subsequent oxidation was also of interest in this study. Previous studies attributed parabolic oxidation behavior at  $1200^\circ\text{C}$  in alloys that contained  $\text{Ti}_5\text{Si}_3$  as a result of a layered scale consisting of an inner  $\text{SiO}_2$  layer and an outer  $\text{TiO}_2$  oxide layer [3]. A composition of Nb-20Mo-15Si-5B-20Ti (20Ti alloy) was chosen to explore the effects titanium additions had on the oxidation behavior, oxide scale development and microstructural stability in a temperature range of  $700 - 1300^\circ\text{C}$  on the Nb-Mo-Si-B system.

Samples were prepared by the Ames Laboratory of Iowa State University by a triple arc melt method in an inert argon atmosphere. Samples were electron discharged machined into cubes of  $5 \times 5 \times 5$  mm. Samples were polished to 600 grit and then ultrasonically cleaned, weighed, and surface area was determined. Three experiments were conducted to study oxide scale

development, short term oxidation behavior (24 hour oxidation), and cyclic oxidation response. To study oxide scale development samples were allowed to ramp at a rate of 10°C/min and held at peak temperatures and then air quenched. To study the short term oxidation behavior samples were ramped at a rate of 10°C/min and held for 24 hours at temperatures between 700 and 1300°C then allowed to furnace cool. The cyclic oxidation response was studied for 24 hours and 168 hours, samples in both cases were ramped at 10°C/min and held for a specified period and then allowed to furnace cool. Samples were then weighed and reintroduced for another cycle of oxidation.

#### **4.1.1 As Cast Microstructures**

Isothermal sections were calculated by a thermodynamic software suit called Pandat<sup>TM</sup> in an effort to predict phase changes within the experimental temperature range. It must be mentioned that these calculated isothermal sections do not take into account the effects boron might have given data base limitations. No phase changes were reported in the experimental temperature range, two phases were predicted to exist in the alloy those being  $\alpha$  solid solution and Nb<sub>5</sub>Si<sub>3</sub> as shown in Figure 4.1 [4]. Both EDS and XRD analysis were used to characterize the as cast microstructures which was found to contain a niobium based solid solution and the Nb<sub>5</sub>Si<sub>3</sub> silicide as shown in Figure 4.2. Results from the x-ray diffraction are presented in Figure 4.3 and indicate the presence of the niobium solid solution and Nb<sub>5</sub>Si<sub>3</sub>, and a few peaks that appear to match Nb<sub>3</sub>Si. The presence of Nb<sub>3</sub>Si was confirmed by EDS and is believed to be present due to the none equilibrium condition in which the microstructure is present after casting.

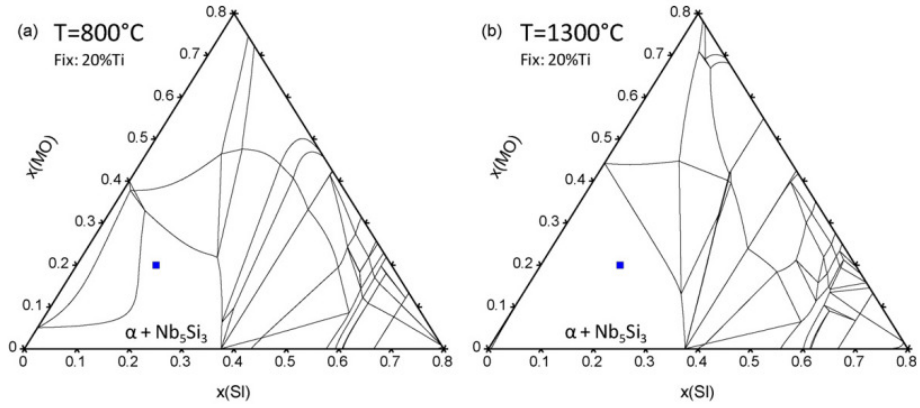


Figure 4.1 Calculated isothermal sections from the Nb-20Mo-15Si-5B-20Ti alloy at 800°C (a) and 1300°C. Sections were calculated using Pandat<sup>TM</sup> software [4].

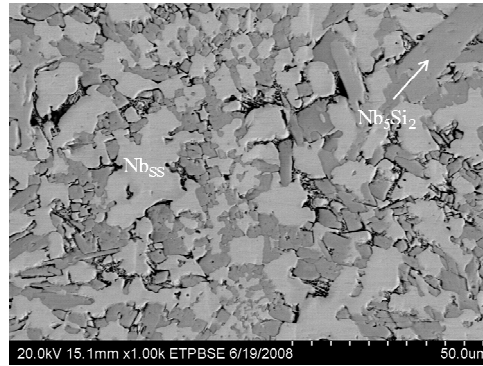


Figure 4.2 As cast microstructure shown in backscatter of 20Ti alloy solid solution and Nb<sub>5</sub>Si<sub>3</sub> identified [4].

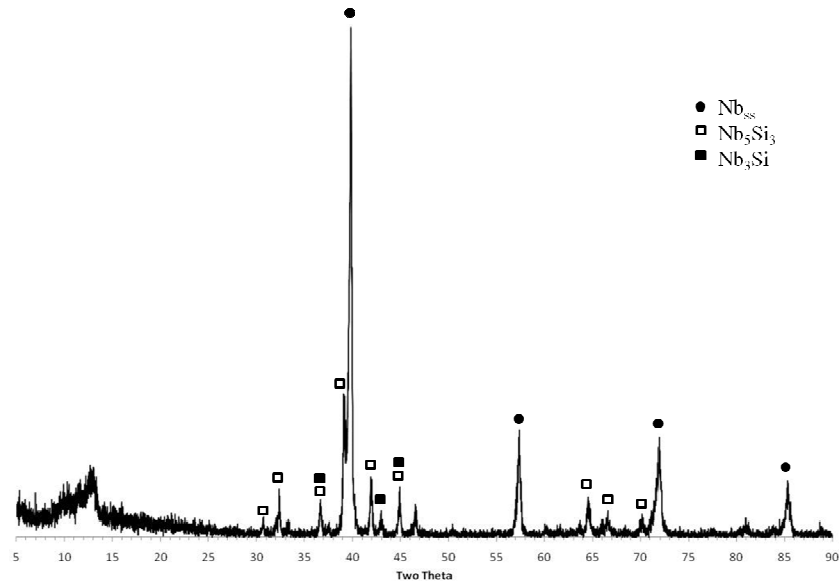


Figure 4.3 XRD spectra of as received Nb-20Mo-15Si-5B-20Ti alloy.

#### 4.1.2 Short Term Oxidation Results

Short term oxidation results are presented in Figure 4.4. The curve shows various details about the final condition of the alloy after oxidation. At lower temperatures, 700 to 900°C, the alloy was observed to develop a thin porous oxide scale consisting largely of  $\text{Nb}_2\text{O}_5$  and what appeared to be  $\text{SiO}_2$  with a large amount of niobium.

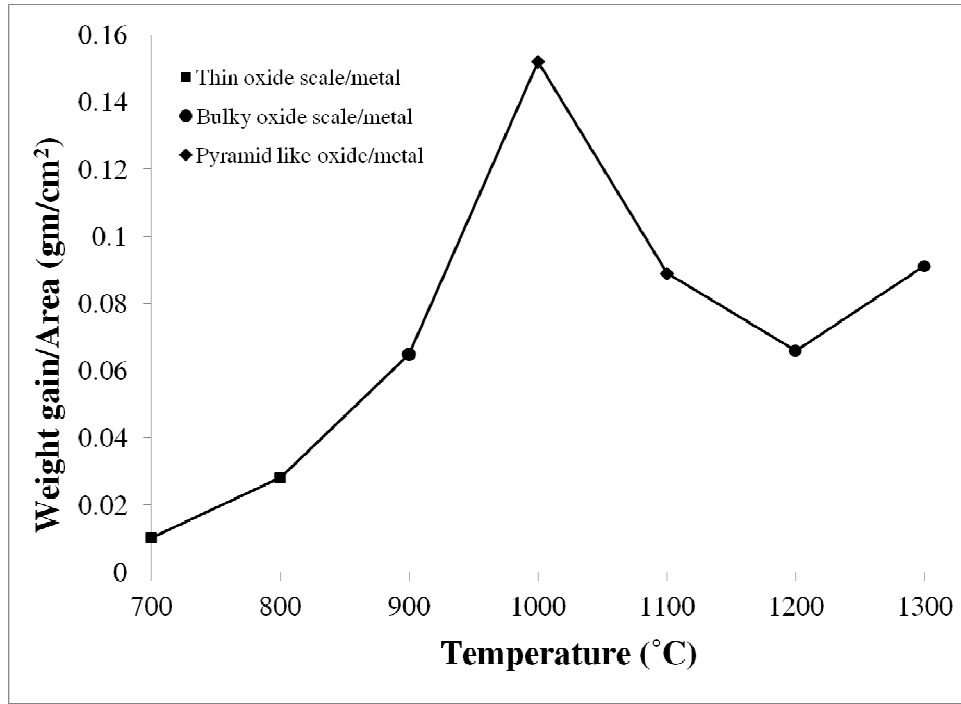


Figure 4.4 Short term oxidation results from the Nb-20Mo-15Si-5B-20Ti alloy obtained after 24 hours of oxidation in air adopted from [4]

At intermediate oxidation temperatures, 1000 and 1100°C, the alloy was observed to contain bulky oxides in the forms of pyramids. The base of each of these oxide pyramids had the same characteristics square face from which it seemed to have developed. The pyramids like oxide structure was also associated with a large weight gain. It must be noted that at both 1000 and 1100°C very large portions of the base metal were consumed at 1000°C approximately 20% of the original sample remained after oxidation at 1100°C. This scale was later determined to be composed primarily of  $\text{Nb}_2\text{O}_5$ . Micrographs of low and intermediate oxide metal interfaces are presented in Figure 4.5. At elevated temperatures between 1200 and 1300°C a bulky thick oxide

scale was observed to develop. Closer examination of the scaled developed at 1300°C revealed a layered oxide structure. There appeared to be a dense layer growing along the oxide metal interface composed of a matrix of niobium rich  $\text{SiO}_2$  and large grains of  $\text{Nb}_2\text{O}_5$  with high concentrations of molybdenum. A layer composed of  $\text{Nb}_2\text{O}_5$  and  $\text{TiO}_2$  grains embedded in a matrix of  $\text{SiO}_2$  is observed to develop next in between the oxide metal and air oxide interfaces. The  $\text{Nb}_2\text{O}_5$  developed in this layer does not contain molybdenum. The oxide layer developed at the oxide air interface is composed of  $\text{Nb}_2\text{O}_5$  needles and a  $\text{SiO}_2$  matrix. The different oxide layers are presented in Figure 4.6 including backscatter micrographs of the oxides developed along the oxide metal interface, the middle layer, and the oxide air interface. Despite the development of the  $\text{SiO}_2$  matrix there was no indication borosilicate glass had been formed.

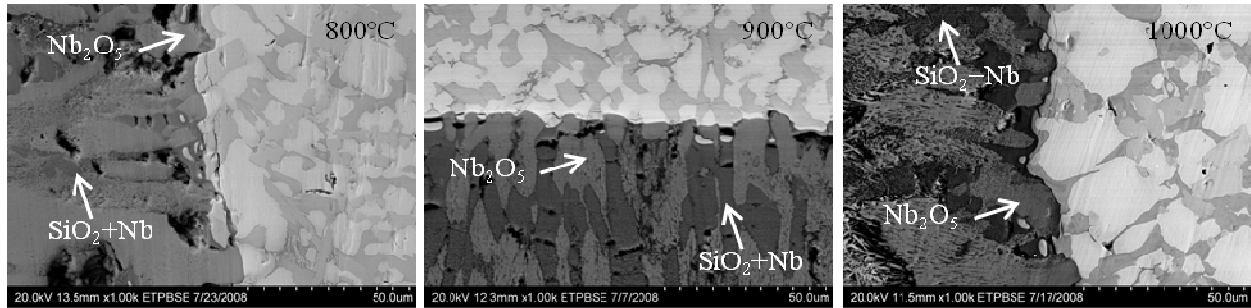


Figure 4.5 Oxide metal interface shown at 800 to 1000°C after short term oxidation, the large amounts of  $\text{Nb}_2\text{O}_5$  developed are attributed to the oxidation of the niobium solid solution.

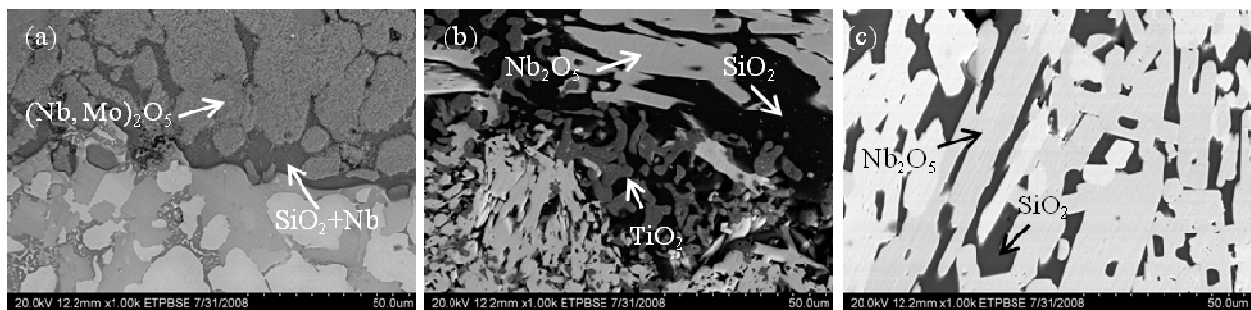


Figure 4.6 Layered oxide developed at 1300°C after 24 hours of oxidation. (a) dense oxide layer developed at the oxide metal interface, (b) second layer consisting of  $\text{Nb}_2\text{O}_5$  and  $\text{TiO}_2$  oxide grains dispersed in  $\text{SiO}_2$ , and (c) oxide developed at air oxide interface consisting of  $\text{Nb}_2\text{O}_5$  and  $\text{SiO}_2$ . Adopted from [4]

### 4.1.3 Short Term Cyclic Oxidation Results

Given the limited understanding gained from characterizing the oxide metal interfaces formed after short term oxidation it was determined that an additional short term oxidation cyclic study was needed. The data presented in Figure 4.7 was collected over a 24 hours period each data point was collected after a set time interval and after the sample had furnace cooled.

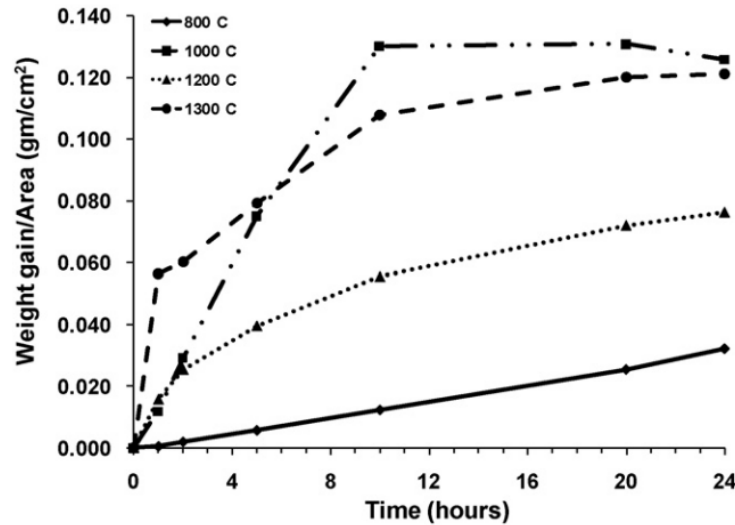


Figure 4.7 Short term cyclic oxidation of Nb-20Mo-15Si-5B-20Ti adopted from [4]

Initial observations of the cyclic data indicate linear oxidation took place at 800°C which can be related to the porous oxide layer that developed which was found to be composed primarily of  $\text{Nb}_2\text{O}_5$  and niobium rich  $\text{SiO}_2$ . At 1000°C the oxidation process appears to be linear however during the first 10 hours the rate is considerably higher than the rest of the data. This can be interpreted as an indication as to when the sample was completely consumed. At 1200°C the cyclic data indicates there was a parabolic response which may indicate that the scale developed at 1200°C afforded some protection over a longer period of time the oxidation rate should have become diffusion controlled through the oxides scale. This may be related to the formation of the layer consisting of dispersed  $\text{Nb}_2\text{O}_5$  and  $\text{TiO}_2$  in the  $\text{SiO}_2$  matrix. The linear rate constants of the 800 and 1000°C curve were reported to be 1.3 and 14.2  $\text{mg}/\text{cm}^2\text{h}$  [4]. The parabolic oxidation curves observed both at 1200 and 1300°C were found to have parabolic rate constants of 200 and 2000  $\text{mg}^2/\text{cm}^4\text{hr}$  respectively [4].

#### 4.1.4 Oxide Scale Development

Valuable insight was gathered from the two shorter oxidation experiments however there was no clear understanding of the development of the oxide scale itself which lead to oxide scale growth experiments. The oxide scale development results which were carried out at 700, 900, 1100, and at 1300°C are presented in Figure 4.8.

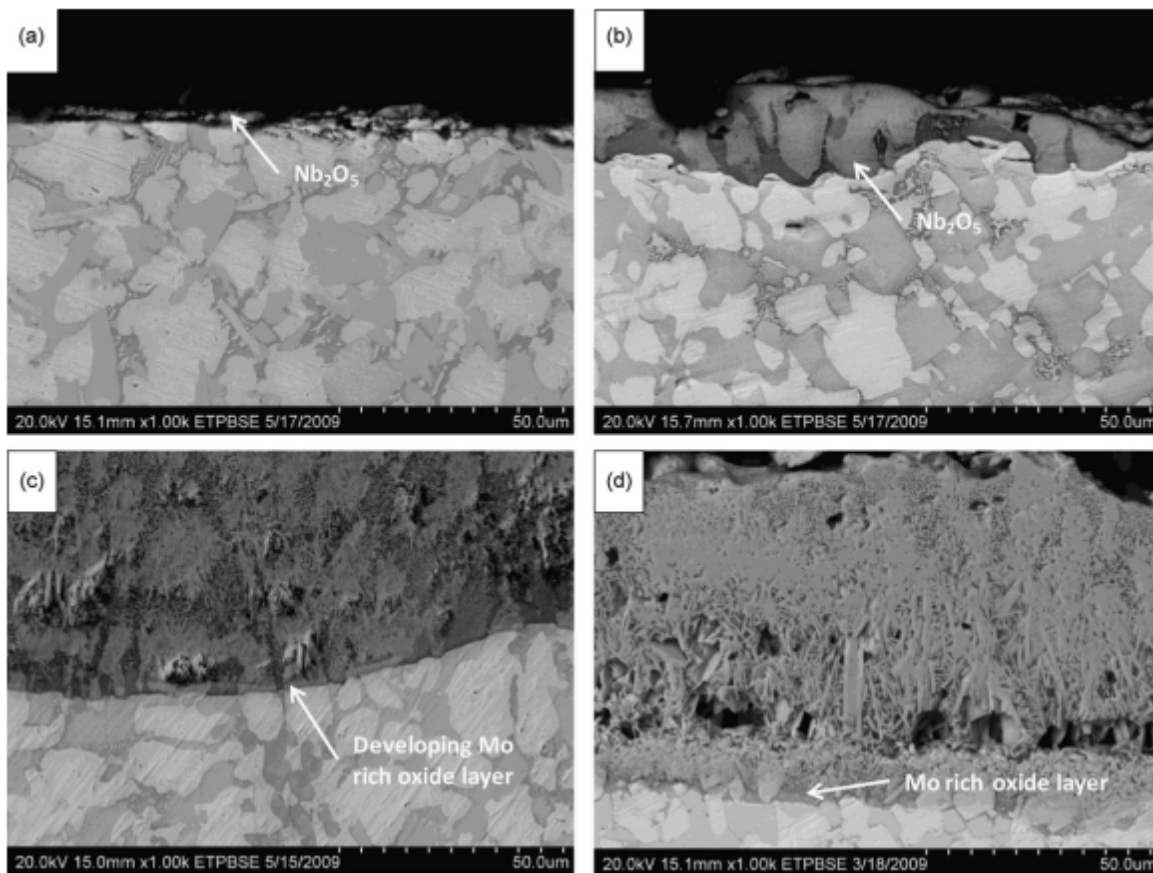


Figure 4.8 Oxide metal interface developed at (a) 700, (b) 900, (c) 1100, and (d) 1300°C after 5 minutes of oxidation in air followed by an air quenching [4].

The porosity found at lower temperatures was also visible in the oxide scale development samples. It appears as though the solid solution phase is being preferentially attacked causing the rapid growth of  $\text{Nb}_2\text{O}_5$ . Another issue that came to light was the apparent lack of molybdenum oxides present in the scale and it is believed that  $\text{MoO}_3$  formed and then volatilized further exacerbating the porosity issues caused by the rapid growth of  $\text{Nb}_2\text{O}_5$ . The oxide metal interface



developed at 900°C shows that the scale developed is almost continuous however the scale developed does not have a uniform composition. After oxidation at 1100°C the oxide formed is observed to be continuous, however, along the metal oxide interface a molybdenum rich layer appears to have begun developing. The molybdenum rich layer appears to be fully formed along the oxide metal interface after oxidation at 1300°C. When the short term cyclic oxidation data is re-examined it becomes apparent that linear oxidation behavior changes to parabolic behavior at temperatures in which the molybdenum rich layer forms along the oxide metal interface. When none cyclic short term oxidation data was reviewed this molybdenum rich layer was found to be best understood by x-ray mapping. An example of x-ray maps showing the molybdenum rich oxidation layer is can be observed in Figure 4.9.

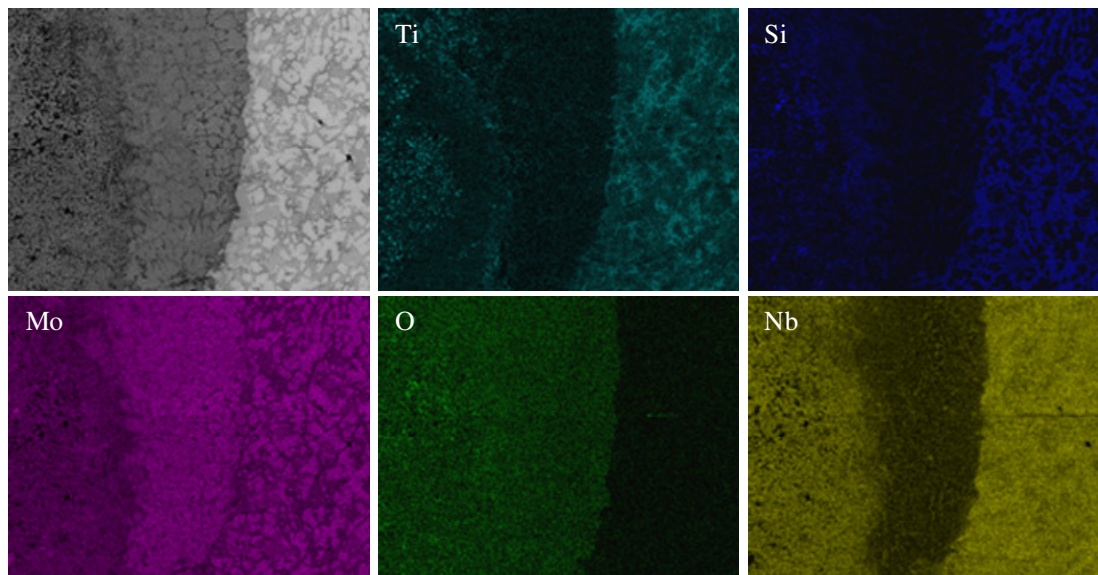


Figure 4.9 20Ti alloy x-ray maps showing molybdenum rich layer along the oxide metal interface at 250X after oxidation at 1300°C.

#### 4.1.5 Long Term Cyclic Oxidation Results

Long term cyclic oxidation was also carried out for a total of 168 hrs in 24 hour cycles. The oxidation curves are presented in Figure 4.10. Linear oxidation behavior was observed for the entire 168 hr test period for both 700 and 800°C which indicates that the alloy was unable to grow a protective scale. At all other temperatures a common trend can be observed which includes rapid weight gain within the first 48 hours of oxidation followed by weight loss. The rapid weight gain curve was found to correspond to the consumption of the sample followed by the volatilization of oxides developed. Two oxides that could possibly be responsible for the volatilization weight loss observed are  $\text{MoO}_3$  and  $\text{B}_2\text{O}_3$  both of which are volatile at 1000°C and above. The presence of either oxide could not be confirmed by EDS or XRD, however, x-ray maps and EDS analysis indicate an enrichment of molybdenum along the metal oxide interface at 1200 and 1300°C after this layer the amount of molybdenum present in the oxide scale diminishes rapidly as the oxide air interface is approached.

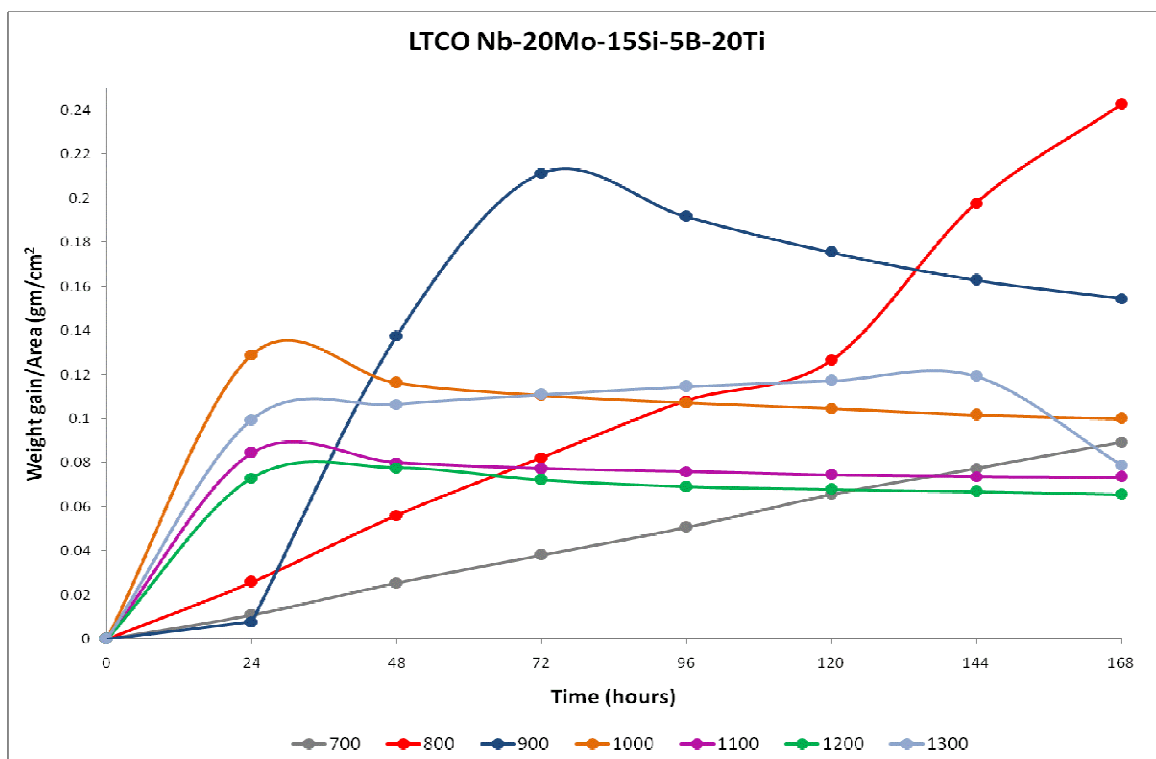


Figure 4.10 Long term cyclic oxidation of 20Ti alloy in air for 168 hours.

#### 4.1.6 Comparison of Titanium Additions and Chromium Additions

This preliminary study was conducted in parallel with another study in which titanium additions were substituted by chromium [5]. The alloy studied with chromium additions had a composition of Nb-20Mo-15Si-5B-20Cr (20Cr alloy). After results were compared [5] it was determined that chromium additions offered better results due to the development of  $\text{CrNbO}_4$  an oxide that has been shown to offer better oxidation resistance than  $\text{Nb}_2\text{O}_5$  [5]. As cast microstructures are presented in Figure 4.11. The 20Cr alloy was found to contain a niobium solid solution,  $\text{NbCr}_2$  Laves phase,  $\text{Nb}_3\text{Si}$ , and  $\text{Nb}_5\text{Si}_3$ .

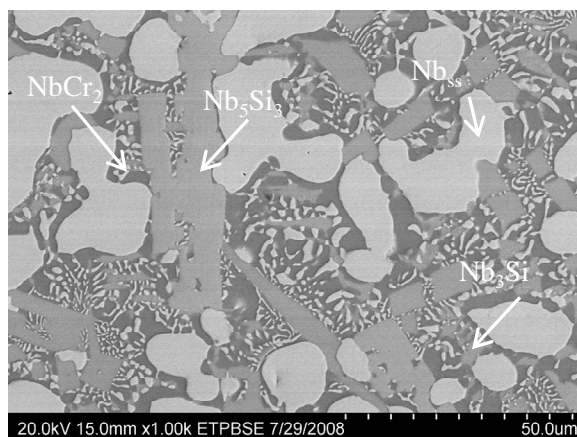


Figure 4.11 20Cr alloy as cast microstructure containing  $\text{NbCr}_2$  Laves phase,  $\text{Nb}_5\text{Si}_3$ ,  $\text{Nb}_3\text{Si}$  and a niobium solid solution [5].

Short term oxidation results are compared in Figure 4.12. The chromium (20 at%) additions were found to give better results throughout the temperature range tested. Layered oxide structures were observed to develop as well. When the short term oxidation data collected for both alloys is compared it becomes clear that the chromium additions provided better oxidation resistance throughout the experimental temperature range, comparison of the short term oxidation data presented in Figure 4.12. The 20Cr alloy did show signs of pest oxidation at low temperatures between 700 and 800°C. Pest oxidation leads to the disintegration of alloys into powder oxides. At intermediate temperatures between 900 and 1000°C the alloy developed a thin

oxide scale consisting of  $\text{CrNbO}_4$  and  $\text{Nb}_2\text{O}_5$ . At high temperatures between 1100 and 1300°C the 20Cr alloy developed a thick bulky oxide scale that contained  $\text{CrNbO}_4$ ,  $\text{Nb}_2\text{O}_5$ , and  $\text{SiO}_2$ .

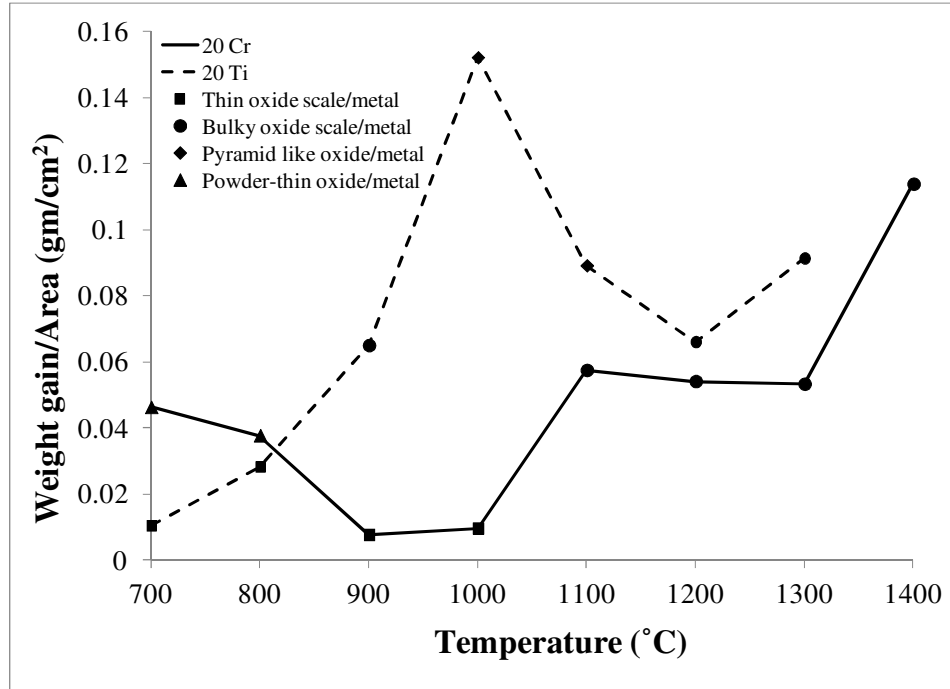


Figure 4.12 Comparison of short term oxidation data of Nb-20Mo-15Si-5B-20X alloy with chromium and titanium additions [5].

It should also be noted that at every temperature, with exception of 1400°C, there was sample remaining after oxidation for the studies conducted on the 20Cr alloy in contrast to the limited survivability of the 20Ti alloy. Several oxide metal interfaces developed by the 20Cr alloy are presented in Figure 4.13. At lower temperatures, 700 and 800°C, the oxide scale developed is porous and consist mainly of  $\text{Nb}_2\text{O}_5$  and  $\text{CrNbO}_4$ . At intermediate temperatures 1000 to 1100 the oxide scale developed is much denser and consist of  $\text{Nb}_2\text{O}_5$  with molybdenum,  $\text{CrNbO}_4$ , and  $\text{SiO}_2$  with  $\text{CrNbO}_4$  dispersed in it. A similar oxide scale can be observed to develop at 1200°C and above the oxide scale however develops in layers. At the metal oxide interface a layer of  $\text{CrNbO}_4$  is observed followed by  $\text{Nb}_2\text{O}_5$  and  $\text{CrNbO}_4$  dispersed in  $\text{SiO}_2$ .

After comparing the oxide scales developed and short term oxidation data it was clear that Cr additions provided better oxidation resistance than titanium additions. It was determined that the development of a  $\text{TiO}_2$  oxide layer would not be possible with the dominant growth of  $\text{Nb}_2\text{O}_5$  without drastically altering the composition of the 20Ti alloy. This would lead to a lower melting point [6]. During this study samples were oxidized at  $1400^\circ\text{C}$  but no results could be obtained from these samples since they appeared to have melted. The preliminary study on titanium additions provided invaluable insight on characterization methods as well as experience in characterizing the high temperature oxidation behavior of refractory metal alloys. The results and observed oxidation behavior were all taken into consideration in the development of the subsequent set of alloys containing boron and higher chromium additions.

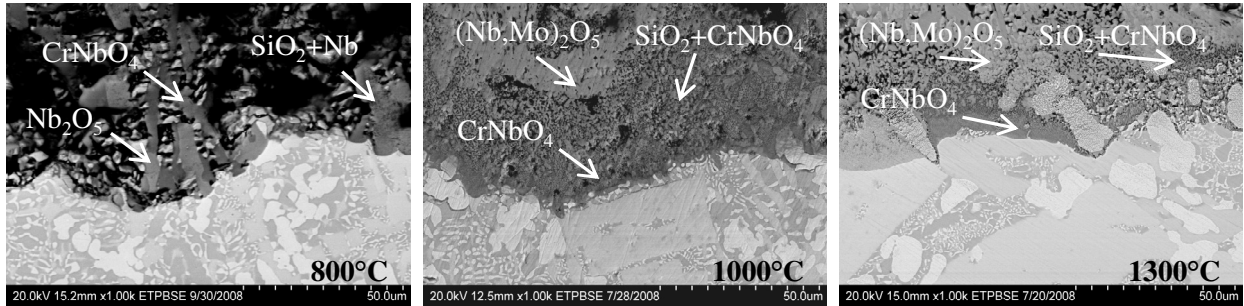


Figure 4.13 Oxide metal interfaces developed on the 20Cr alloy after short term oxidation at 800, 900, and  $1300^\circ\text{C}$  [5].

#### 4.2 OXIDATION BEHAVIOR OF Nb-Mo-Si-B WITH CHROMIUM ADDITIONS

The second oxidation study in the preliminary work was carried out on three alloys from the Nb-Mo-Si-Cr system with boron additions and modified chromium content, compositions are presented in table 4.1 [7]. It was necessary to understand the effects boron additions had on the oxidation response of alloy from this system. This work was largely inspired by the limited success several authors had developing a borosilicate glass layer on alloys from the Mo-Si-B alloy system. The previous study comparing titanium and chromium additions also indicated that a change in the alloy composition was needed to reduce the amount of primary alpha in the microstructure which seemed to be the largest source of  $\text{Nb}_2\text{O}_5$  growth.

Table 4.1 Alloy compositions intended to study the effects of chromium composition and boron additions.

Alloy	Composition (% at.)					Composition (% weight)				
	Nb	Cr	Mo	Si	B	Nb	Cr	Mo	Si	B
25Cr	40	25	20	15	0	50.518	17.671	26.084	5.727	0.000
25Cr5B	35	25	20	15	5	46.816	18.715	27.626	6.065	0.778

Other authors who studied similar niobium based multiphase alloys have reported improvements in oxidation resistance by reducing the volume fraction of primary solid solution and increasing the volume fraction of both silicides and Laves phases [8]. Increases in chromium were shown to both increase the amount of Laves phase and reduce the amount of niobium solid solution according to composition calculations by Pandat<sup>TM</sup> presented in Figure 4.14. Initial observations indicate that an addition of 5 atomic percent could reduce the fraction of solid solution by almost 10% throughout the test temperature range. In a similar fashion a larger fraction of Laves phase is predicted.

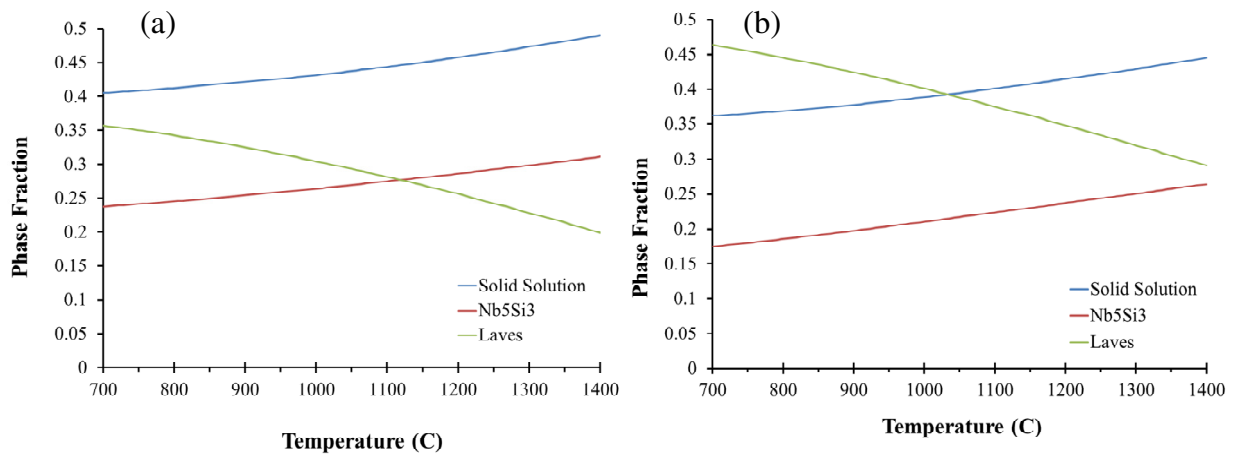


Figure 4.14 Phase fractions as a function of temperature calculated using Pandat<sup>TM</sup> for alloy compositions containing (a) 20 and (b) 25Cr additions.

#### 4.2.1 As Cast Microstructures

As cast microstructures in back scatter contrast are presented in Figure 4.15. Three common phases were present in all of the alloys those being a niobium solid solution, Nb<sub>5</sub>Si<sub>3</sub>,

and  $\text{NbCr}_2$  Laves phase. An additional silicide,  $\text{Nb}_3\text{Si}$ , is observed in the 25Cr 5B alloy and has a large blocky morphology with smooth interfaces. In both alloys the  $\text{Nb}_5\text{Si}_3$  silicide is observed to develop in areas where the Laves phase coarsens around the solid solution interfaces. Further characterized by EDS analysis of the solid solution in both alloys found large amounts of molybdenum in excess of 50at Pct. Initial observations indicate that increased chromium content reduces the amount of primary solid solution present in the microstructures.

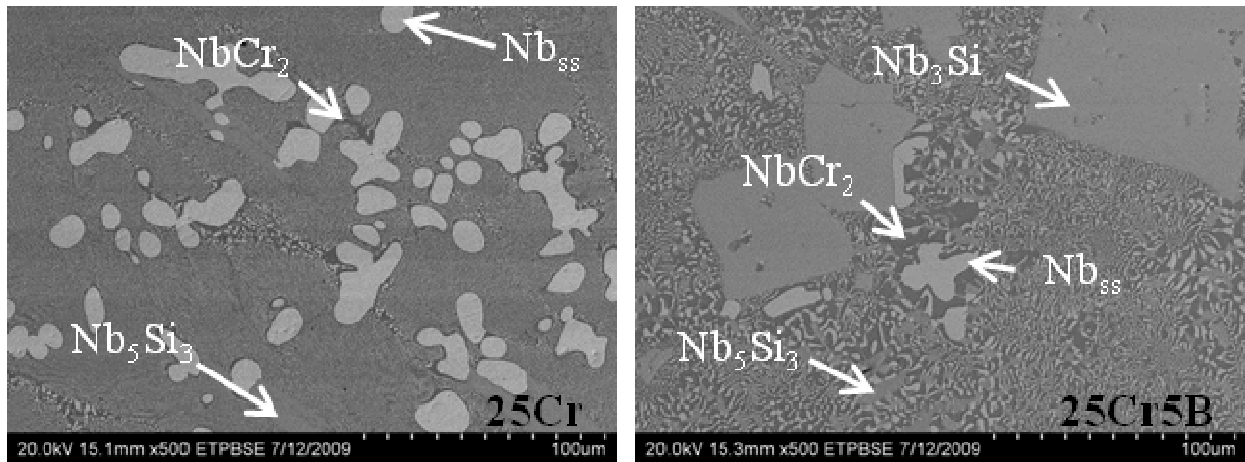


Figure 4.15 As cast microstructures for preliminary alloys in collected in back scatter mode [7].

Image analysis was carried out on each of the as cast microstructures, results are presented in table 4.2. Phase fractions were obtained by determining the fraction of each phase observed in the as cast microstructures at 500X. The fractions were calculated based on the contrast of each phase present given, that the micrographs were collected in back scatter imaging mode in which contrast is determined by mean atomic number. Similar results were obtained from previous alloy studied Nb-20Mo-15Si-5B-20Cr (20Cr5B) and are presented for comparison purposes.

Table 4.2 Phase fractions calculated for preliminary alloys studied containing various chromium and boron additions.

Phase Fractions Calculated at 500X			
Phase	25Cr	25Cr5B	20Cr5B
Laves	45	41	29
Solid Solution	36	19	38
Silicide	19	40	33

Two apparent trends related to the compositions of the alloys can be observed in the phase fractions. Additions of boron appear to lead to lower fractions of solid solution and higher fractions of silicides. Lower amounts of solid solution could be explained by the lower fraction of niobium present in the alloy since the 5at.% additions of boron lower the total amount of niobium in the alloy. However lower amounts of niobium in the alloy compositions do not account for the formation of larger fractions of silicide. Further investigation should be undertaken to determine the exact mechanisms involved. Additionally it should be noted that the microstructures are studied in the as cast conditions. Given the nature of refractory metals annealing should be undertaken at elevated temperatures in inert atmosphere for extended periods of time. Several authors have undertaken this type of heat treatment to determine equilibrium microstructures and various other properties with annealing times ranging from 100 to  $1 \times 10^3$  hours [9-11]. In either case the amount of solid solution in the microstructures was reduced and higher fractions of both NbCr<sub>2</sub> Laves phase and silicide were achieved.

Isothermal sections from the Nb-Cr-Mo-Si system were calculated for the increased amount of chromium and are presented in Figure 4.16. The calculated isotherms can be related to Figure 4.15 which shows various trends as a function of temperature in which amount of solid solution and Nb<sub>5</sub>Si<sub>3</sub> increase with temperature while the amount of Laves phase decreases. No phase changes were predicted throughout the experimental temperature range of 700 to 1300°C.



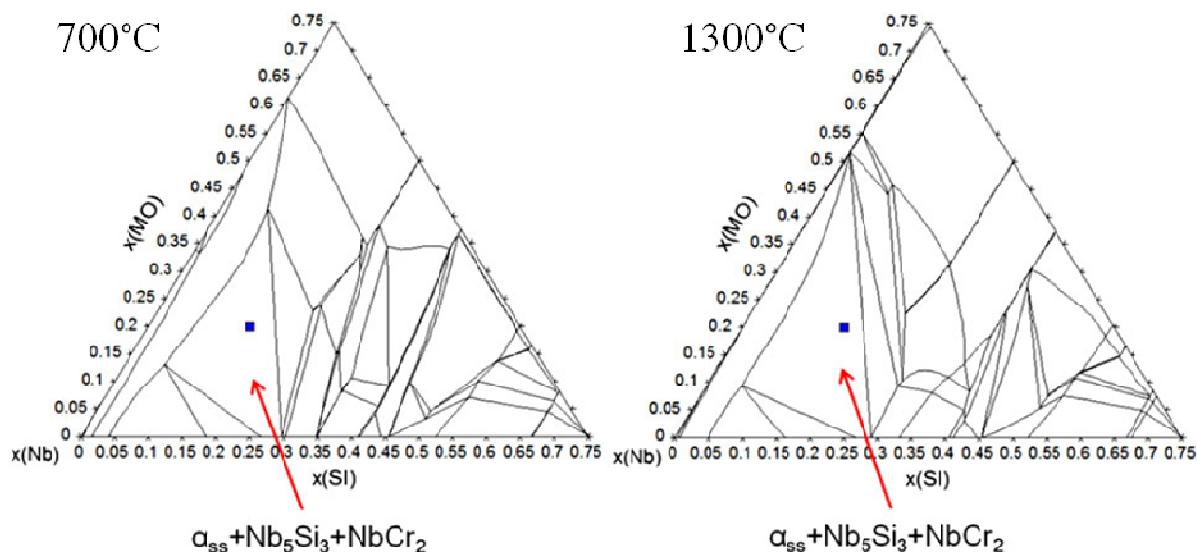


Figure 4.16 Isothermal sections calculated for the Nb-Mo-Si-Cr system at 700 and 1300°C while holding 25at.%Cr constant [7].

#### 4.2.2 Short Term Oxidation Results

Short term oxidation results are presented in Figure 4.17 which also includes information on the observed morphology of oxide products. Preliminary observations indicate that boron additions provide oxidation resistance through the entire experimental temperature range when compared to the 25Cr alloy with no boron additions. At elevated temperatures similar oxidation behavior is observed in both alloys. Samples were sectioned and polished to reveal the oxide metal interfaces. EDS analysis was used to identify phases and oxides present. XRD analysis was conducted to confirm the presence of phases and oxides identified by EDS analysis. The surface oxides were also characterized by XRD analysis to determine what oxides were present on the samples surface after oxidation.

Thermo gravimetric results are presented in Figure 4.18 in terms of weight change per unit area as a function of time for three temperatures 800, 1000, and 1200°C. The oxidation curves at 800°C indicate a linear oxidation behavior for both alloys. At 1000°C the oxidation behavior of the 25Cr indicates some mass loss for the first 12 hours after which weight gain increases linearly, the oxidation curve for the 25Cr5B alloy remains linear. At 1200°C the

oxidation curve for 25Cr indicates an initial increase in weight followed by a mass loss and almost linear weight gain. The oxidation curve for 1200°C indicates parabolic oxidation behavior which is indicative of diffusion controlled oxidation rate.

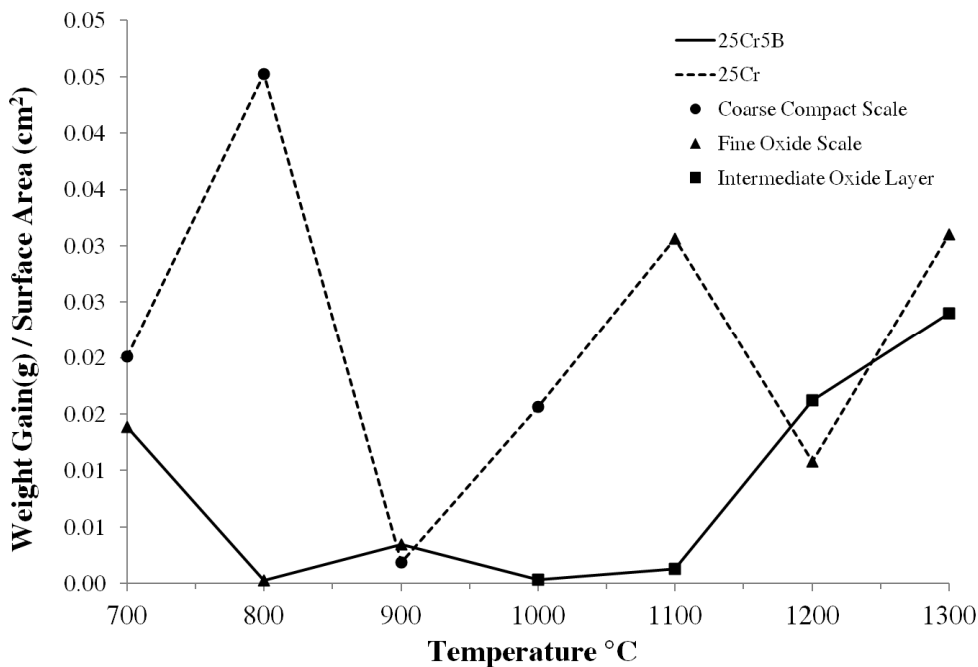


Figure 4.17 Short term oxidation results for the 25Cr, and the 25Cr5B alloy [7].

Coarse porous oxide scales were observed to develop on both alloys at low temperatures between 700 and 800°C as shown in Figure 4.19. In both alloys  $\text{Nb}_2\text{O}_5$  and  $\text{CrNbO}_4$  were identified. Additionally the presence of a mixed oxide was also detected. It is believed to be a mixture of  $\text{Nb}_2\text{O}_5$  and  $\text{SiO}_2$ . Scales developed at 800°C appear to be coarse, however this, seems to further exacerbate the porosity issues encountered in the scales developed at 700°C. At 900°C the morphology of the oxide scale developed on the 25Cr5B alloy changes while the scale developed on the 25Cr coarsens but is still porous. The  $\text{Nb}_2\text{O}_5$  developed in the 25Cr scale seems to retain the morphology the solid solution had in the remaining metal before oxidation. An intermediate oxide layer develops at 900°C at the metal oxide interface of the 25Cr5B alloy as shown in Figure 4.20, which provides a more detailed view of the oxide metal interface in

secondary electron imaging mode. A layer of chromium depleted, silicon rich oxides forms above this intermediate layer. Followed by a layer of  $\text{SiO}_2$  containing large amounts of dispersed  $\text{Nb}_2\text{O}_5$  and  $\text{CrNbO}_4$  oxides. Also observed was the preferential oxidation of the  $\text{Nb}_3\text{Si}$  phase which was made apparent by the formation of  $\text{Nb}_2\text{O}_5$  beneath the oxide metal interface also shown in Figure 4.20.

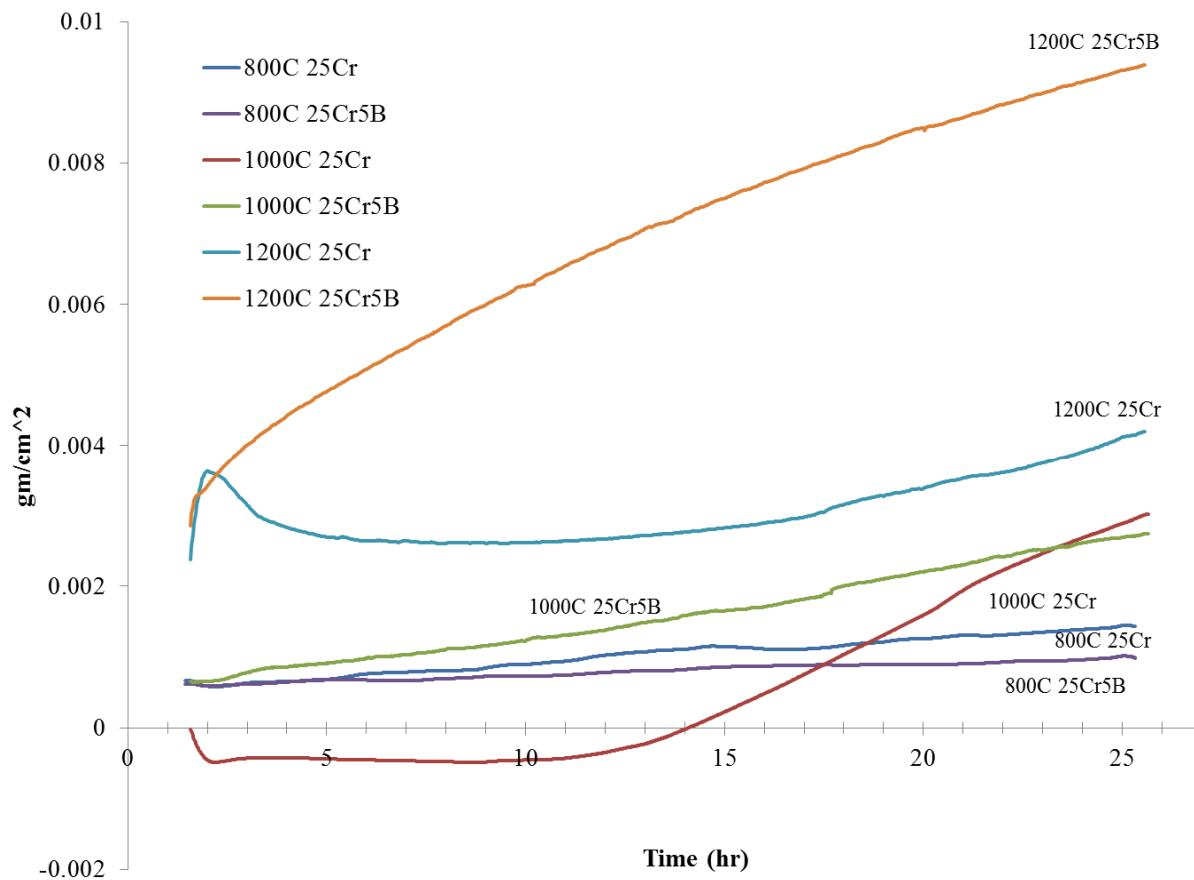


Figure 4.18 Thermal gravimetric data collected over 24 hours of oxidation of the 25Cr and 25Cr5B alloys in air at 800, 1000, and 1200°C.

To better understand the oxide morphology and the distribution of elements across the metal oxide interface x-ray maps were collected from the 25Cr5B oxide metal interface after oxidation at 900°C and are shown in Figure 4.21. The chromium depletion and the molybdenum enrichment are clearly visible in the corresponding x-ray maps. Maps pertaining to oxygen

distribution show contrast in the layer described as internal oxidation or the intermediate oxide layer indicating the presence of oxygen. Also observable when both oxygen and niobium maps are compared is the development of the  $\text{Nb}_2\text{O}_5$  beneath the oxide metal interface from the  $\text{Nb}_3\text{Si}$  grain. The outline of the  $\text{Nb}_3\text{Si}$  grain can be clearly seen in the chromium map indicating the absence of chromium in the silicide. When the silicon and oxygen maps are compared the locations where  $\text{SiO}_2$  has developed become evident. The development of  $\text{SiO}_2$  appears to take place after the intermediate oxidation layer. The  $\text{SiO}_2$  matrix developed was further characterized to determine whether or not the presence of borosilicate could be detected. EDS analysis was carried out in several places but no boron peak was observed an example of the spectra collected from the  $\text{SiO}_2$  matrix is presented in Figure 4.22. The presence of borosilicate cannot be verified or discounted at this time given the nature of EDS analysis the concentration of boron may have been too low to detect with the current interment. Areas with no contrast in all of the x-ray maps indicate the presence of a pore in the oxide scale.

The morphology of the oxide developed on the 25Cr alloy changes at  $1000^\circ\text{C}$  relative to the morphologies previously observed at lower temperatures between  $700$  and  $900^\circ\text{C}$ . A continuous oxide is developed containing  $\text{Nb}_2\text{O}_5$  and a mixed oxide as presented in Figure 4.23. Large voids were observed in the oxide scale developed on the 25Cr alloy after short term oxidation at  $1000^\circ\text{C}$  and were found to be lined with  $\text{SiO}_2$ . To better visualize the distribution of elements a x-ray map was collected at the oxide metal interface and is presented in Figure 4.24. Comparing the silicon and oxygen maps reveals the presence of  $\text{SiO}_2$  as evident by the contrast along the edges of the voids observed in the oxide scale. The scale developed after short term oxidation at  $1100^\circ\text{C}$  was also found to contain  $\text{Nb}_2\text{O}_5$  and a mixture of oxides believed to be  $\text{Nb}_2\text{O}_5$  and  $\text{SiO}_2$ , the scale was also much more compact and did not contain large voids.

Oxide morphologies of the scales developed on the 25Cr5B alloy at  $1000$  and  $1100^\circ\text{C}$  remain similar to the morphology observed at  $900^\circ\text{C}$ . With the exception of a thinner oxide scale with respect to previously observed scales developed at lower temperatures the morphology remained largely unchanged. The layered oxide structure maintained its previous ordering

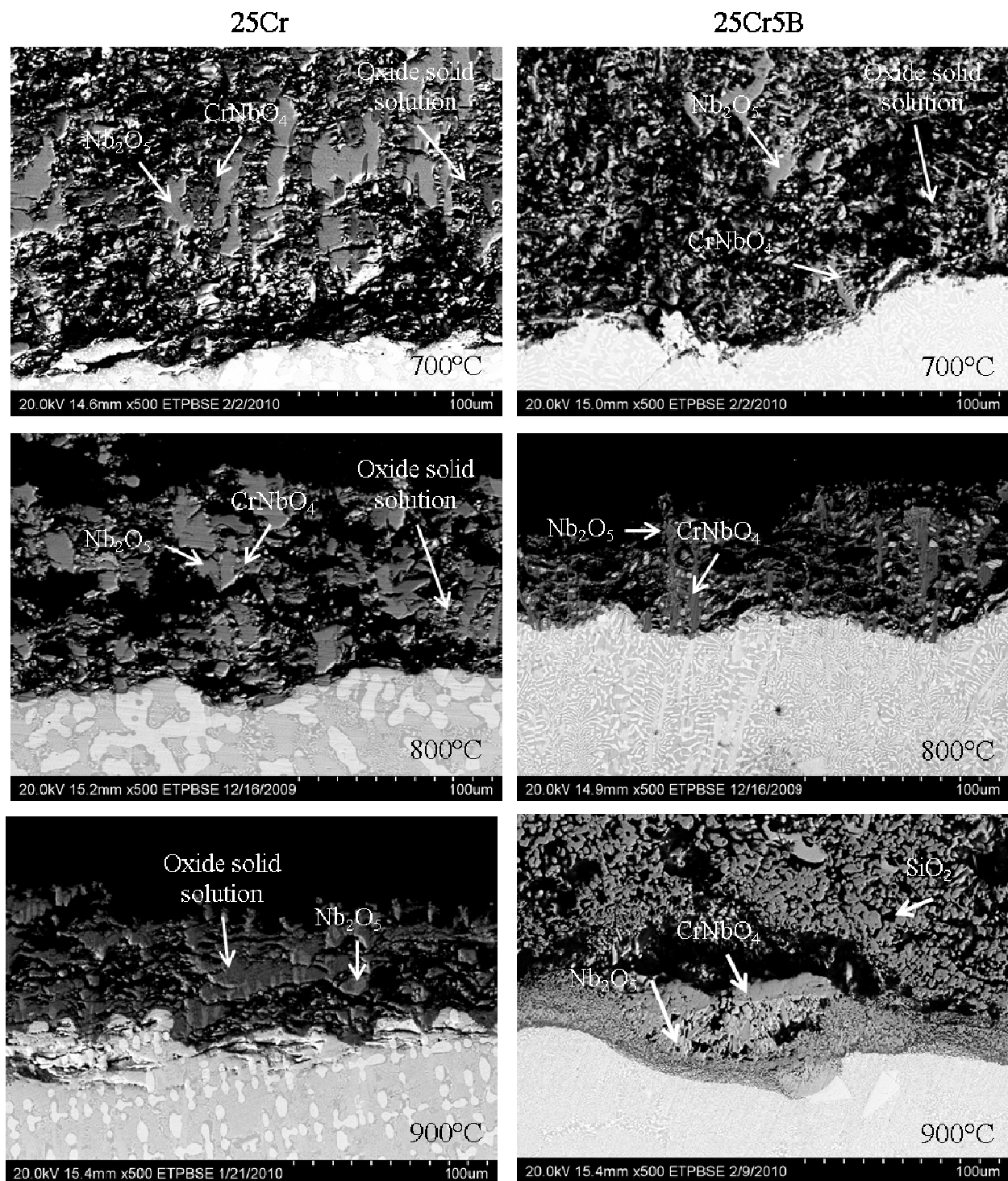


Figure 4.19 Oxide metal interfaces developed on both the 25Cr and 25Cr5B alloy at 700, 800, and 900°C after short term oxidation [7].

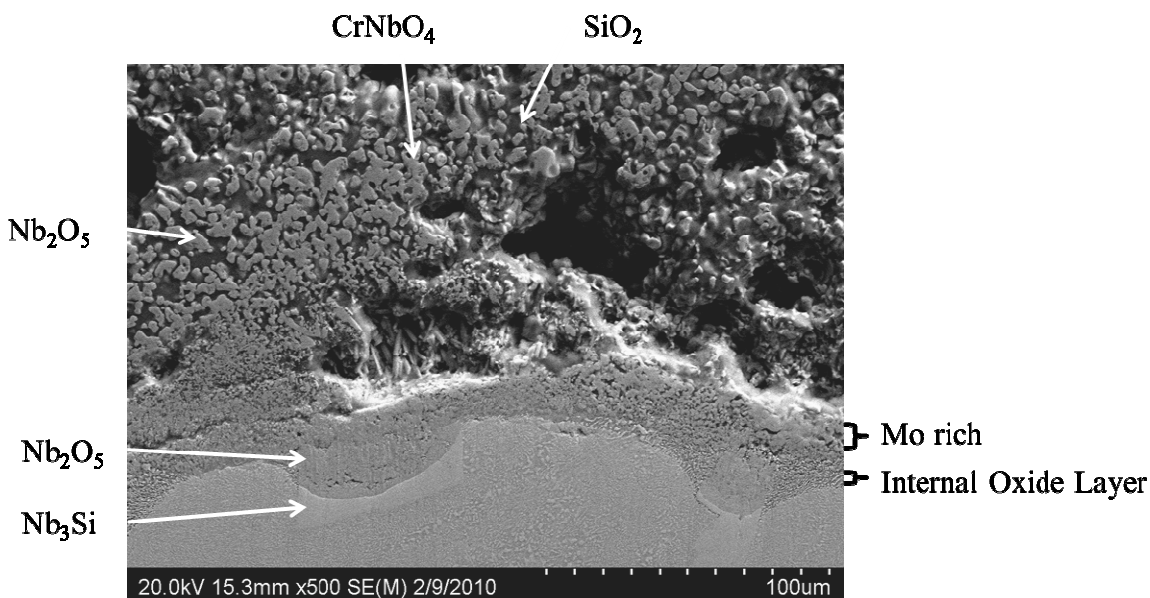


Figure 4.20 Closer examination of the oxide metal interface and intermediate oxide layer developed on the 25Cr5B alloy after short term oxidation at 900°C.

scheme. The presence of the intermediate oxidation layer is still observed, X-ray maps still indicate the intermediate oxidation layer is molybdenum rich and chromium depleted.

Oxide metal interfaces developed at 1300°C after short term oxidation are presented in Figure 4.25. The dense oxide consisting of a mixture of Nb<sub>2</sub>O<sub>5</sub> and SiO<sub>2</sub> developed on the 25Cr alloy was observed to spall off as a result of a crack along the oxide metal interface. A high magnification micrograph presented in Figure 4.26 along the oxide metal interface reveals the presence of both. The oxide scale developed on the 25Cr5B alloy remained the same with the exception of the development of a dense layer of Nb<sub>2</sub>O<sub>5</sub> and CrNbO<sub>4</sub> along the oxide air interface. A similar layer can be observed to develop on the 25Cr alloy however it does not appear to be as dense or well developed.



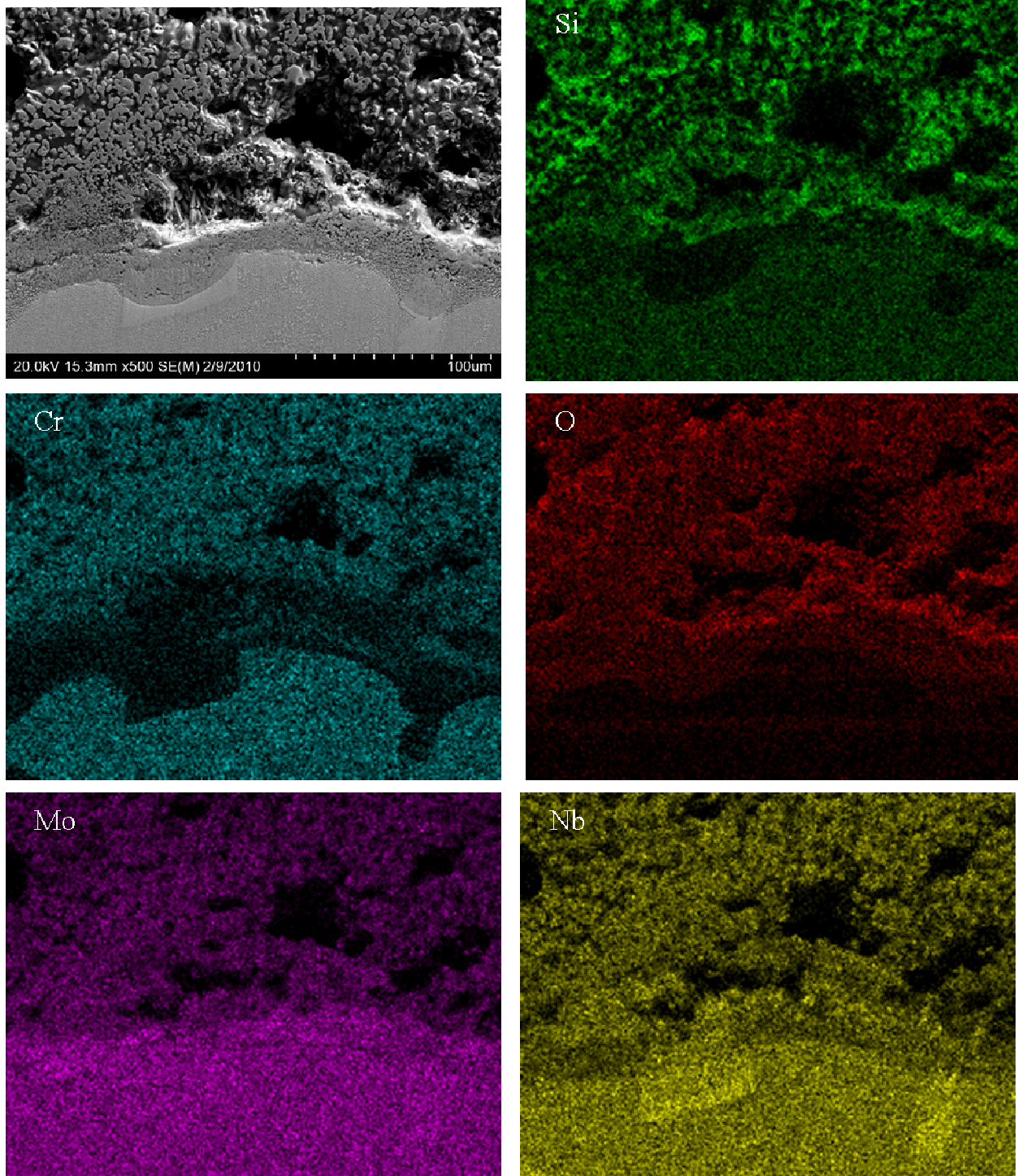


Figure 4.21 X-ray maps collected from the oxide metal interface developed on the 25Cr5B alloy after short term oxidation at 900°C showing the chromium depletion and molybdenum enrichment of the intermediate oxidation layer.

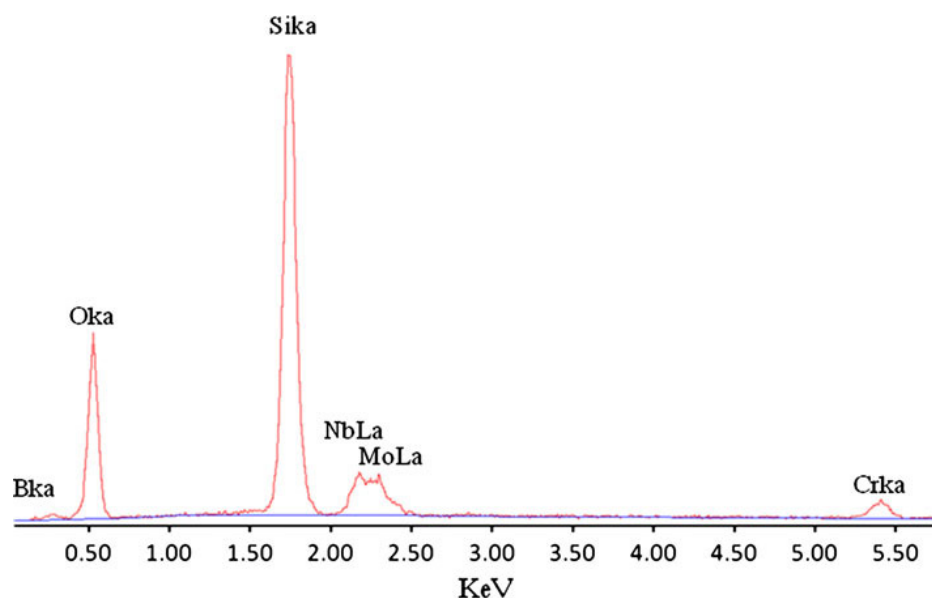


Figure 4.22 EDS spectra collected for  $\text{SiO}_2$  matrix developed in the oxide scale of the 25Cr5B alloy after short term oxidation at  $900^\circ\text{C}$  [7]

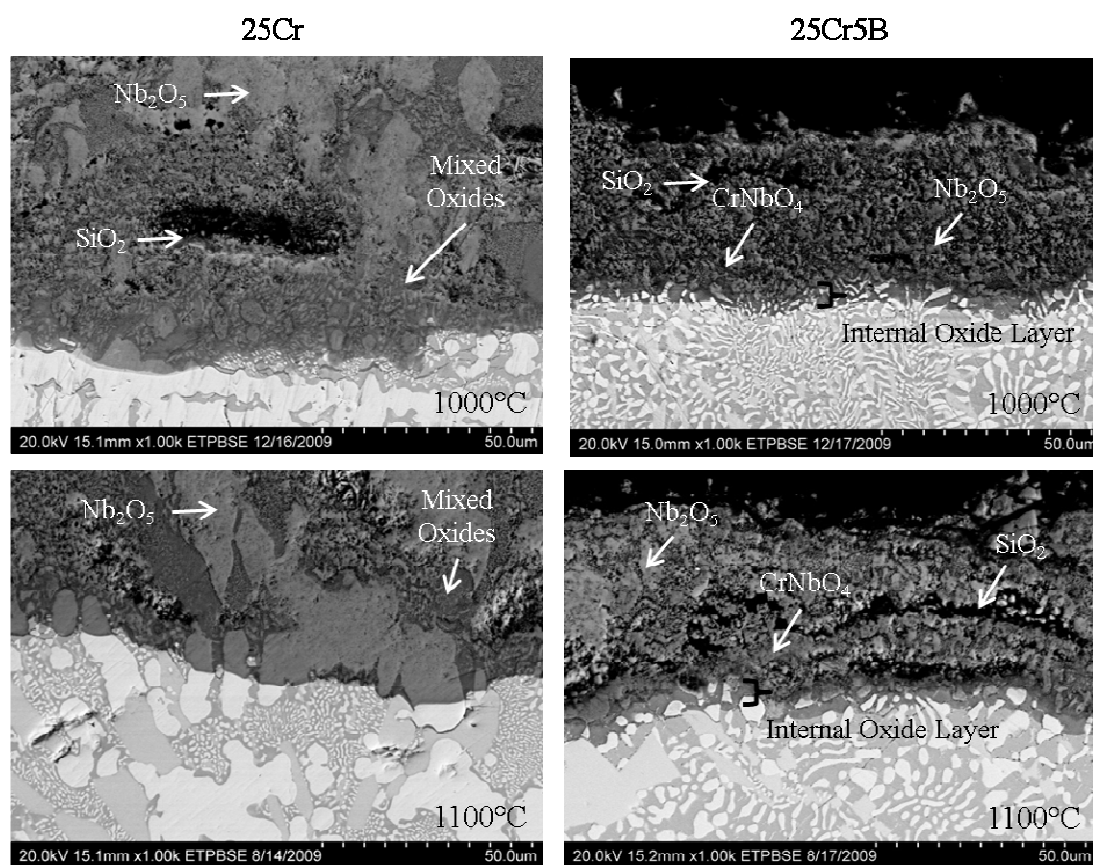


Figure 4.23 Oxide metal interfaces developed after short term oxidation at  $1000$  and  $1100^\circ\text{C}$  for the 25Cr and 25Cr5B alloys.



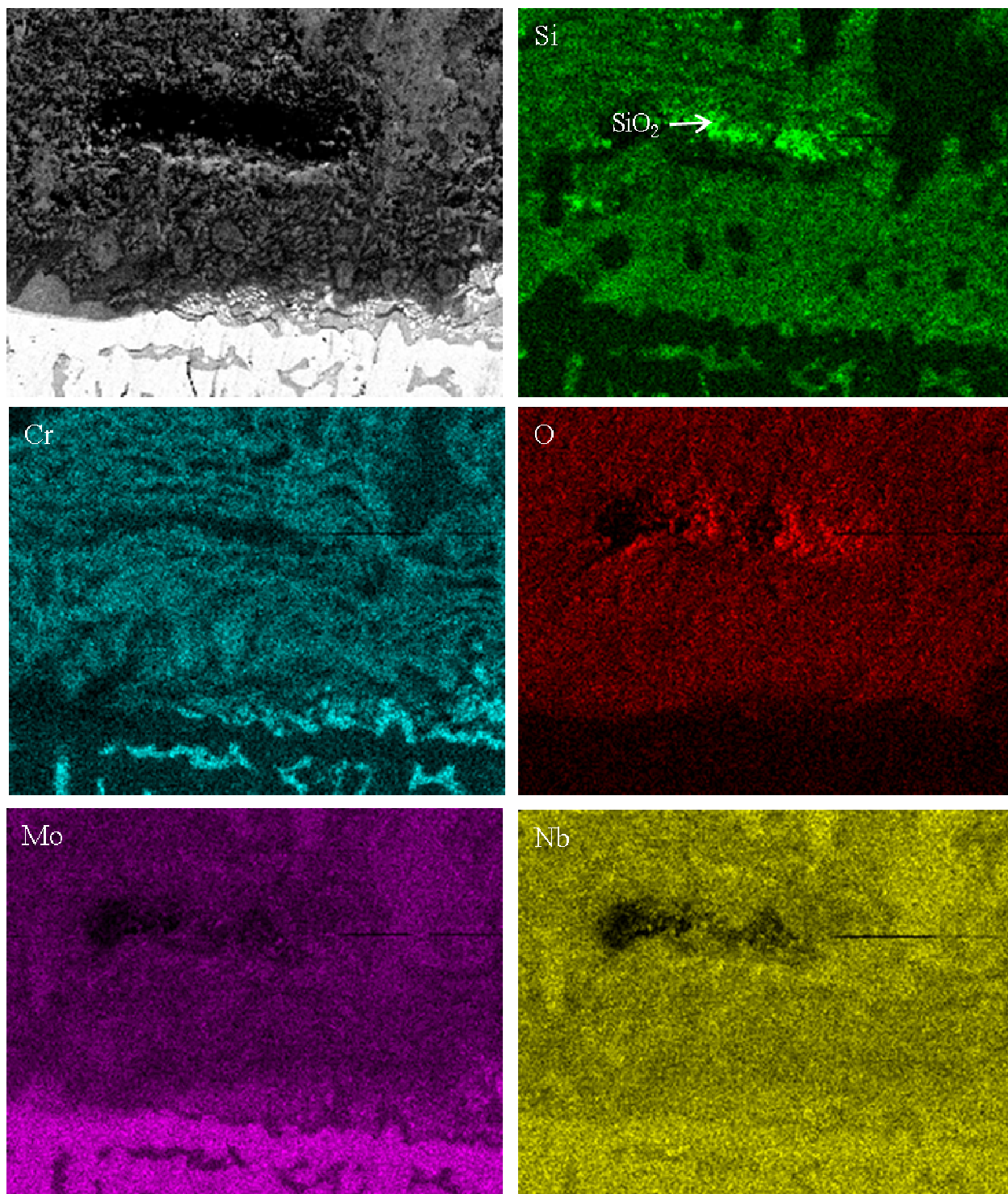


Figure 4.24 X-ray maps collected along the oxide metal interface developed on the 25Cr alloy after short term oxidation at 1000°C. Voids in the oxide scale are shown to be lined with SiO<sub>2</sub>.

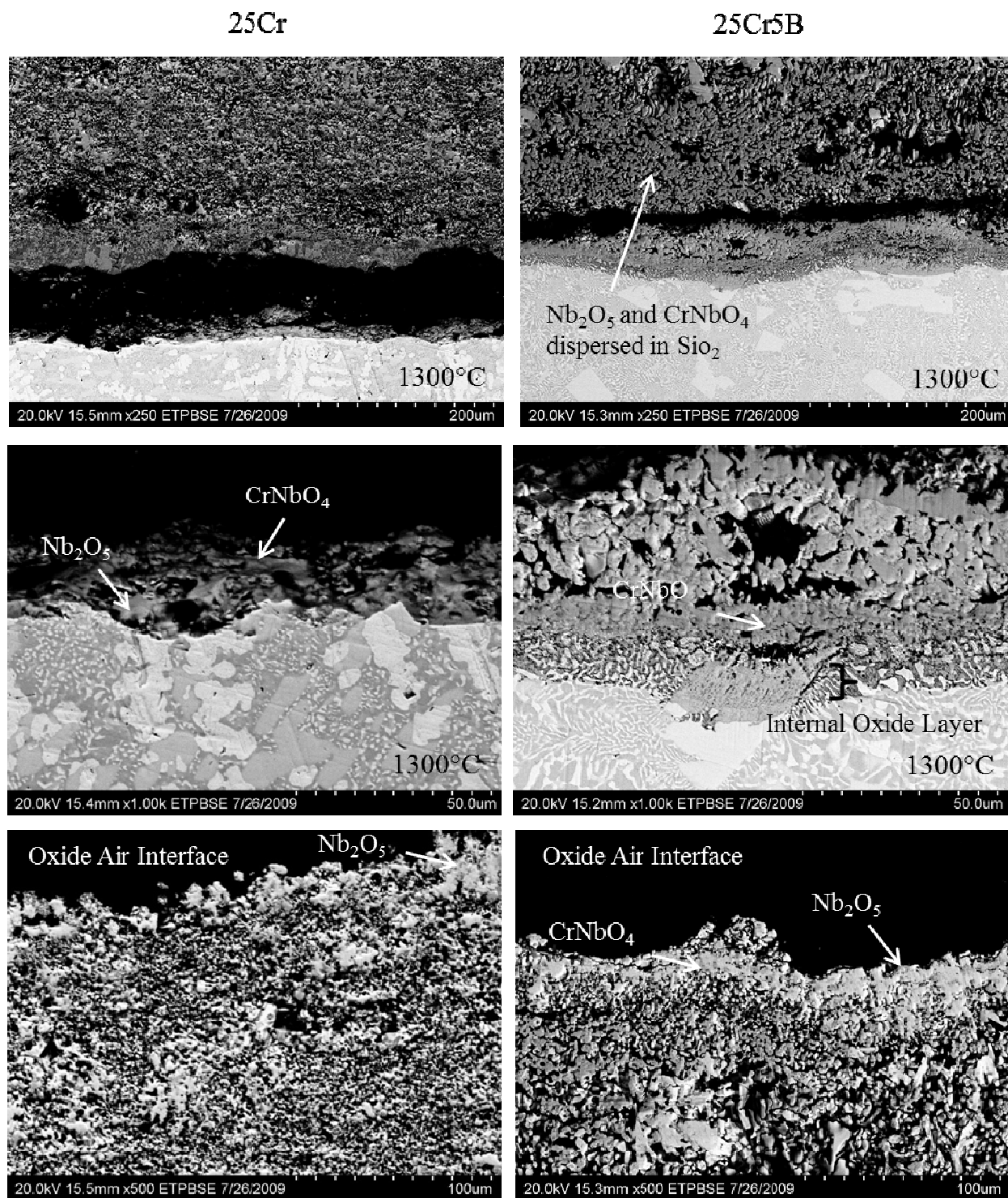


Figure 4.25 Oxide metal interface and oxide air interface developed on the 25Cr and 25Cr5B alloys after short term oxidation at 1300°C showing the spalling of the oxide from the 25Cr alloy.

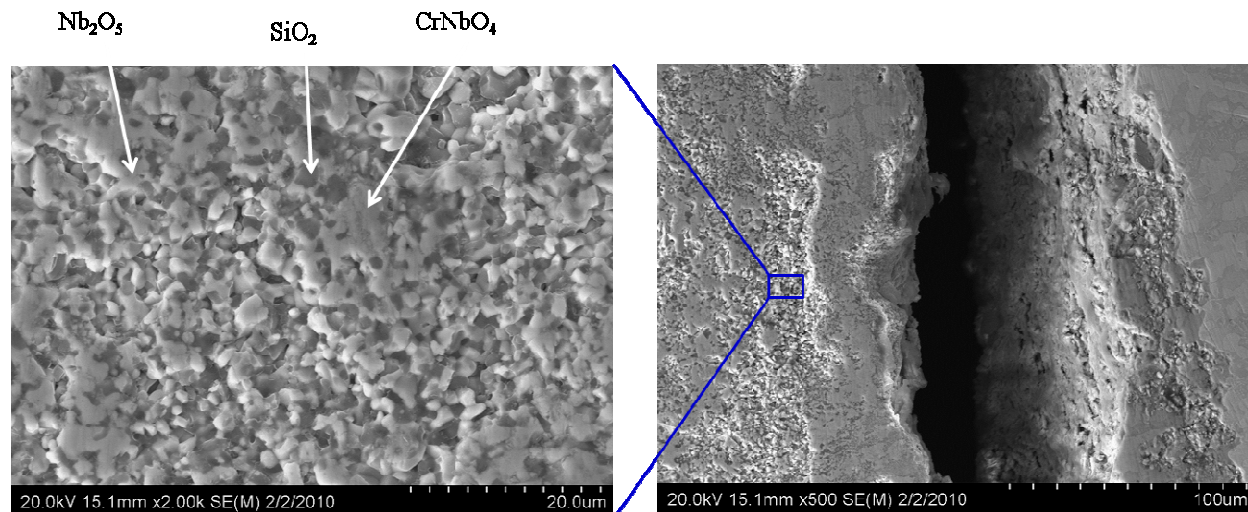


Figure 4.26 High magnification micrograph of the dense oxide scale developed on the 25C alloy after short term oxidations showing the composition of the fine oxide structure.

### 4.2.3 Discussion

XRD characterization of the surface oxides detected  $\text{Nb}_2\text{O}_5$  and  $\text{CrNbO}_4$  as shown in Figure 4.27. A transformation of  $\text{Nb}_2\text{O}_5$  was observed at  $900^\circ\text{C}$ . The peaks corresponding to a low temperature form of crystalline  $\text{Nb}_2\text{O}_5$  disappear from the XRD spectra in samples oxidized at temperatures above  $900^\circ\text{C}$  and the peaks corresponding to a high temperature monoclinic form were detected.  $\text{Nb}_2\text{O}_5$  has been shown to exist in its low temperature form as  $\beta\text{-Nb}_2\text{O}_5$  at temperatures below  $850^\circ\text{C}$ , as temperature increased it transformed into  $\gamma\text{-Nb}_2\text{O}_5$  which has a based centered monoclinic crystal structure [12]. It must also be noted that many of the  $\text{Nb}_2\text{O}_5$  polymorphic transformations are not reversible and are not detectible by calorimetry making their detection possible at room temperature [13]. No crystalline forms of molybdenum oxides were detected.  $\text{MoO}_3$  is expected to have volatilized.

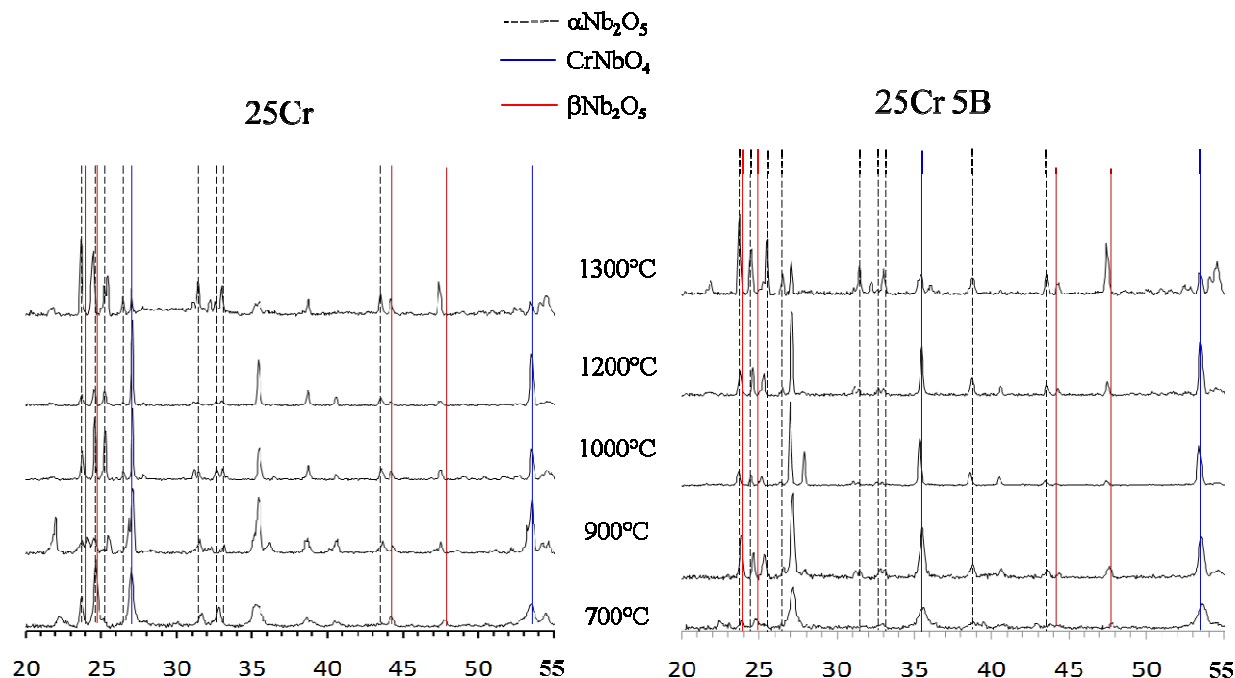


Figure 4.27 X-ray diffraction spectra collected from surface oxides developed on both 25Cr and 25Cr5B alloy after short term oxidation [7].

The coarse and porous oxide scales developed at 700°C, Figure 4.19, on both alloys are believed to be the result of the volatilization of  $\text{MoO}_3$ , dominant growth of  $\text{Nb}_2\text{O}_5$  and slow growth of  $\text{SiO}_2$ . The linear oxidation behavior observed at 800°C in the thermal gravimetric results presented in Figure 4.18 can be related to the growth of this non protective oxide scale. Linear oxidation kinetics are indicative of an oxidation process that is not diffusion controlled, in this case the large pores developed in the scale offer oxygen a path to the metal oxide interface.

The intermediate oxidation layer developed at 900°C on the 25Cr5B alloy is believed to be the result of boron additions to the alloy. A similar layered structure was observed by Liu et al. in Nb-Mo-Si-B hyper-eutectic alloys [14]. The current set of alloys are hyper-eutectic and also develop a similar layered oxide scale indicating that the formation of the intermediate oxidation zone may not be dependent on the hypo or hyper-eutectic nature of the alloy. EDS and x-ray mapping of the intermediate oxidation layer as well as areas adjacent to it reveal high concentrations of molybdenum and very low concentrations of chromium as shown in (Figure

4.21). Molybdenum concentrations were found to decrease drastically beyond the intermediate oxidation zone, in contrast concentrations of chromium were found to increase in  $\text{CrNbO}_4$ . The presence of molybdenum at temperatures greatly exceeding its volatilization temperature may be an indication that the layer of  $\text{SiO}_2$  developed may contribute to enhanced oxidation resistance.

The oxidation kinetics for the 25Cr5B alloy remains linear at  $1000^\circ\text{C}$  which indicates a rate limiting process that is not diffusion controlled. It may be possible that the oxidation rate is being limited by the intermediate layer. As previously mentioned linear oxidation can occur when oxygen has to diffuse through a layer of uniform thickness. In this case that layer is the intermediate oxide layer, since it is continuous and of uniform thickness. This would also indicate that the outer oxide scale is providing negligible oxidation protection. Longer oxidation studies may be necessary since the oxide scale may not be fully developed yet. The presence of the intermediate oxide layer may be present but the rest of the outer scale may not be fully developed yet. Earlier work on the Nb-Cr-Si-Ti-B system indicates that the intermediate oxide layer can be observed as soon as the ramping to the oxidation temperature is complete [4]. Kinetics for the 25Cr alloy indicate an initial mass gain followed by a loss that can be associated with the volatilization of both molybdenum and possibly chromium oxides. It is believed that eventually the oxide scale reaches a critical thickness at which point the rate at which oxides are volatilized no longer dominates the  $\text{Nb}_2\text{O}_5$  growth rate.

The role of molybdenum at the intermediate oxidation interface is still not understood. It was proposed by Chattopadhyay et al [15], that the substitution of Nb with Mo in  $\text{Nb}_2\text{O}_5$  results in lower anion vacancies resulting in slower diffusion of oxygen and an increased activity of silicon enhancing the preferential formation of  $\text{SiO}_2$  [16]. One might postulate similar effects on the activity of chromium and silicon in the 25Cr/5B alloy given the similarities in free energy of formations for  $\text{SiO}_2$  and  $\text{Cr}_2\text{O}_3$  ( $-700.3\text{kJ/mol}$  and  $-832.8\text{ kJ/mol}$  respectively) [17].  $\text{Cr}_2\text{O}_3$  although not detected by XRD is believed to be involved in the development of  $\text{CrNbO}_4$ . Information regarding the formation of  $\text{CrNbO}_4$  in multi-phase alloys is not available but studies



related to the development of dielectric ceramics report the formation of  $\text{CrNbO}_4$  after  $\text{Cr}_2\text{O}_3$  and  $\text{Nb}_2\text{O}_5$  powders calcined together at elevated temperature [17].

The oxidation kinetics observed at  $1200^\circ\text{C}$  for the 25Cr alloy indicate an initial mass gain possibly due to the diffusion of oxygen into the metal followed by a mass loss often associated with the volatilization of above mentioned oxides. The low weight gain that follows indicates that the rate of volatilization and oxidation are almost equal because if no oxidation were taking place then no scale would have developed on the sample. Eventually the scale reaches a critical thickness at which point the rate of volatilization is no longer comparable to that of the formation of non-volatile oxides. The oxidation kinetics for the 25Cr5B are parabolic indicating that diffusion controlled oxidation has been reached. Given the numerous complex reactions taking place it is very difficult to calculate the oxidation rates using typical methods established for single phase alloys.

#### **4.3 SUMMARY**

Additions of boron to the Nb-20Mo-15Si-25Cr were found to suppress the formation of solid solution in the as cast microstructure and promote the formation of silicides and  $\text{NbCr}_2$ . Oxide scales developed at lower temperatures on both alloys had a coarse and porous morphology resulting from the dominant growth of  $\text{Nb}_2\text{O}_5$  and volatilization of molybdenum oxides. Thermogravimetric studies of both alloys at  $800^\circ\text{C}$  also revealed linear oxidation kinetics at lower temperatures corresponding to non-protective oxide scales. The observed layered oxide structure and intermediate oxidation zone formed exclusively on the 25Cr5B alloy after 24hr of exposure at  $900^\circ\text{C}$  and above. Oxidation kinetics at intermediate temperatures indicated linear oxidation for both alloys. Further studies may be necessary to determine whether diffusion controlled oxidation can be achieved as a result of the intermediate oxidation interface. At elevated temperatures oxide scales that formed on the 25Cr alloy were pore free resulting in increased stresses developed along the metal oxide interface due to the mis-match of coefficients of thermal expansion between the oxide scale and remaining metal resulting in the formation of

cracks along the interface and spalling of the oxide scale. The high temperature oxidation kinetics indicate that the 25Cr5B alloy had reached a state in which oxidation was diffusion controlled. On the other hand the 25Cr alloy was believed to have several competing mechanisms, oxide volatilization and the growth of Nb<sub>2</sub>O<sub>5</sub> resulting in a plateau in the oxidation curve.

The results obtained in this preliminary study indicated that boron additions were beneficial to both oxidation resistance and in modifying the phase composition of the microstructure. The development of the intermediate oxidation layer is not entirely understood or the role molybdenum plays. Future work will be focused on silicon to boron ratios and the amount of molybdenum in the alloys. Thermal gravimetric results were also obtained offering another invaluable form of characterization and a better perspective on oxidation kinetics.

#### 4.3 REFERENCES

1. S.C. Parida, N.K. Gupta, K. Krishnan, G.A. Rama Rao, B.K. Sen, Metall. Mater. Trans. A 39 (2008) 2020–2025.
2. Y.S. Chen, C.J. Rosa, Oxid. Met. 14 (1980) 147–165.
3. R. Mitra, V.V. RamaRao, Metall. Mater. Trans. A. 29A (1998) 1665–1675.
4. B. I. Portillo and S.K. Varma. J. Alloys Compd. 497 (2010) 68-73.
5. J. Ventura, B. I. Portillo, S.K. Varma, and R.N. Mahapatra. ECS Transactions. 16 (2009) 157-166.
6. Y. Shen, X. Ding, F. Wang, Y. Tan, J.-M. Yang, J. Mater. Sci. 39 (2004) 6583–6589.
7. B. I. Portillo. and S.K. Varma. Metall. Mater. Trans. A. 42A (2011) in print.
8. K.S. Chan: Metall. Mater. Trans. A, 35A (2004) 589–97.
9. J. Geng, G. Shao, and P. Tsakiroopoulos. Intermetallics. 14 (2006) 832-837.
10. F. Chu, D.J. Thoma, P.G. Kotula, S. Gerstl, T.E. Michell, I.M. Anderson, and J. Bentley. Acta Mater. 46 (1998) 1759-1769.

11. P.R. Subramanian, T.A. Parthasarathy, M.G. Mendiratta, and D.M. Dimiduk. *Scripta Metallurgica*. 32 (1995) 1227-1232.
12. K. Chattopadhyay, R. Mitra, and K.K. Ray, *Metall. Mater. Trans. A*, 39A (2008) 577–92.
13. F. Holtzberg, A. Reisman, M. Berry, and M. Berkenblit. *J. Am. Chem. Soc.* 79 (1965) 2039–43.
14. Y. Liu, M.J. Kramer, A.J. Thom, and M. Akinc. *Metall. Mater. Trans. A*. 36A (2006) 601–07.
15. K. Chattopadhyay, R. Mitra, and K.K. Ray. *Metall. Mater. Trans. A*. 39A (2008) 577–92.
16. I. Barin. *Thermochemical Data of Pure Substances*, 2nd ed., Wiley VCH, Weinhiem, Germany, 1993, pp. 573–1505.
17. Y.-J. Hsiao, Y.-H. Chang, T.-H. Fang, Y.-S. Chang, and Y.-L. Chai: *J. Alloys Compd.* 421 (2006) 240–46.



## Chapter 5: Results and Discussion

Preliminary studies on the Nb-Cr-Si-Mo alloy system indicate that additions of boron promoted the growth of a layered oxide structure and suppressed both pest oxidation and oxide spalling [1]. Results from the preliminary studies conducted on the effects of boron additions on oxidation behavior indicated that the alloy composition Nb-25Cr-20Mo-15Si-5B at.% should be investigated further [1]. Three modified alloys based on the Nb-25Cr-20Mo-15Si-5B at.% alloy with modified molybdenum, silicon, and boron content are presented in Table 5.x. Boron and silicon content has been modified in an attempt to promote the development of borosilicate glass. Boron to silicon ratios have been reported to influence the development of borosilicate glass in studies based on Mo-Si-B alloys [2]. Molybdenum content has been modified to further reduce the amount of primary solid solution developed. Preliminary studies have indicated that higher compositions of molybdenum were found to reduce the amount of primary solid solution developed in the microstructure [1]. Primary niobium solid solution was observed to be preferentially attacked in preliminary studies resulting in the formation of un-protective Nb<sub>2</sub>O<sub>5</sub> [3]. The oxidation behavior of three alloys Nb-25Cr-15Mo-20Si-5B (15Mo5B alloy), Nb-25Cr-20Mo-15Si-10B (10B alloy), and Nb-25Cr-10Mo-15Si-5B (10Mo5B alloy) at.% which have modified silicon, molybdenum, and boron concentrations will be reported in this section.

### 5.1 CHARACTERIZATION OF THE AS-CAST MICROSTRUCTURE

Pandat<sup>TM</sup> was used to calculate isothermal sections from the Nb-Cr-Mo-Si system as shown in Figure 5.1, for the set of alloy compositions presented in Table 4.1. It must be noted that boron additions were not considered in the calculated isothermal sections due to database limitations. The isothermal sections predicted the stable formation of three common phases  $\alpha$  solid solution, Nb<sub>5</sub>Si<sub>3</sub>, and NbCr<sub>2</sub> Laves phase throughout the experimental temperature range, no phase changes were predicted.

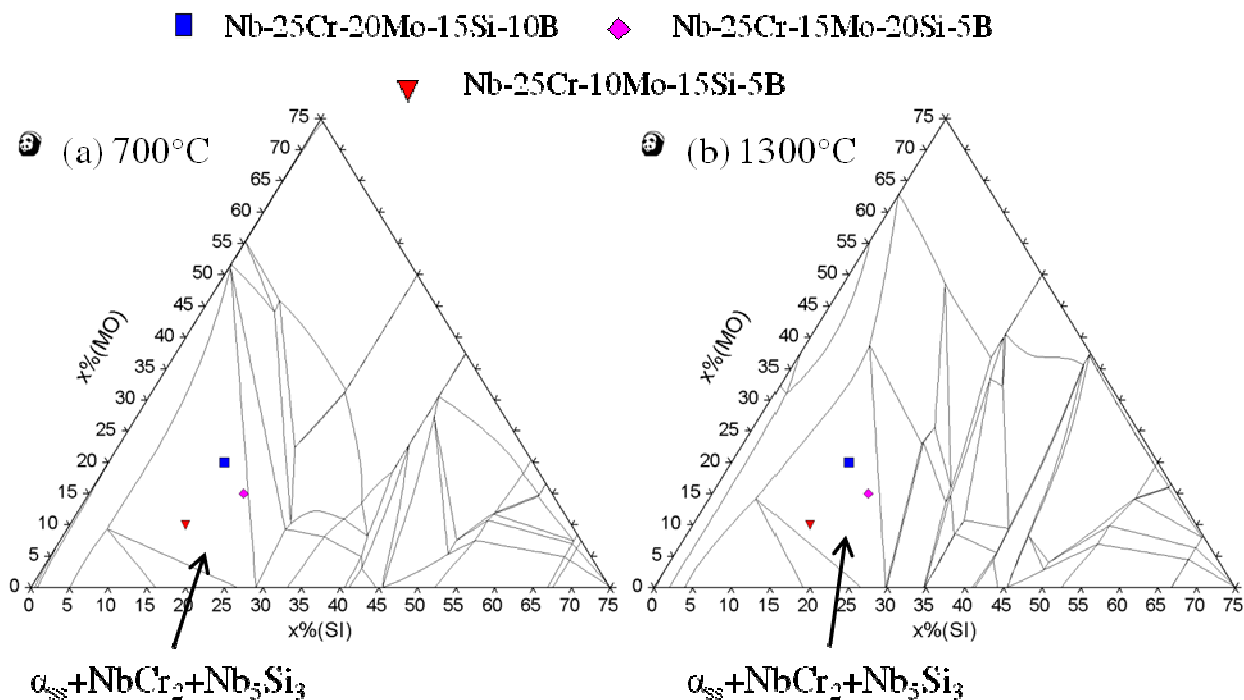


Figure 5.1 Calculated isothermal sections for Nb-25Cr-20Mo-15Si-10B, Nb-25Cr-15Mo-20Si-5B, and Nb-25Cr-10Mo-15Si-5B alloys at (a) 700 and (b) 1300°C. Three common phases were predicted a solid solution, NbCr<sub>2</sub> Laves phase, and Nb<sub>5</sub>Si<sub>3</sub>.

As-cast microstructures were characterized by scanning electron microscopy in various modes including back scatter, EDS analysis, and x-ray mapping. The as-cast microstructures are presented in Figure 5.2. Three common phases were identified a solid solution, NbCr<sub>2</sub> Laves phase, and the Nb<sub>5</sub>Si<sub>3</sub> silicide. Phases were identified by EDS analysis and then x-ray diffraction analysis confirmed their presence. The x-ray diffraction spectra collected from the as-cast microstructures are presented in Figure 5.3.

The as-cast microstructure morphology is different for each alloy. The 15Mo5B alloys appears to have a large fraction of NbCr<sub>2</sub> Laves phase and Nb<sub>5</sub>Si<sub>3</sub> silicide. Solid solution is observed to be distributed throughout the NbCr<sub>2</sub> phase. The 10B alloy appears to have a eutectic like morphology consisting of Laves phase and solid solution with relatively large silicides distributed throughout the microstructure. Morphology of the 10Mo5B alloy appears to be a

mixture of both the 10B and 15Mo5B alloys. A eutectic like structure composed of  $\text{NbCr}_2$  and solid solution provide a matrix in which  $\text{Nb}_5\text{Si}_3$  and primary  $\text{NbCr}_2$  are distributed within.

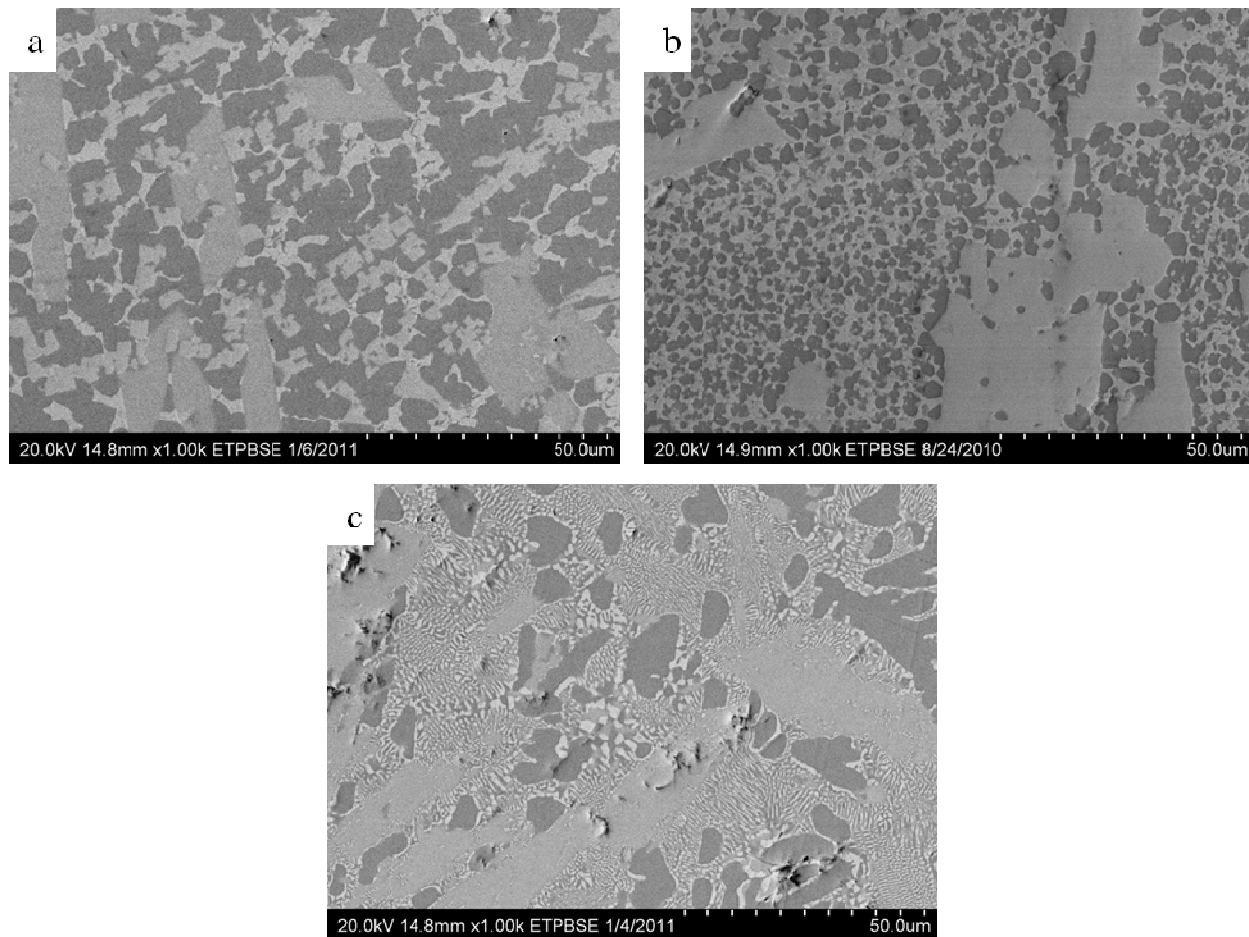


Figure 5.2 Back scatter micrographs of as cast microstructures at 1000x mag (a) Nb-25Cr-15Mo-20Si-5B, (b) Nb-25Cr-20Mo-15Si-10B, and (c) Nb-25Cr-10Mo-15Si-5B alloys.

Additional image analysis was performed on the as-cast microstructures in an attempt to quantitatively characterize the fractions of the phases present for each alloy. Image analysis results are presented in Table 5.1. Unfortunately the microstructures of the 10B alloy did not lend itself well to the image analysis process due largely in part to the fine structure of the solid solution and silicides in the eutectic like microconstituent. Only the  $\text{NbCr}_2$  Laves phase was able quantified given the difference in contrast with respect to the solid solution and silicides.

The image analysis results seemed to indicate relatively large fractions of Laves phase present in all three alloy compositions. When compared to the phase fractions observed in the preliminary studies presented in Table 4.2 it is apparent that lower molybdenum content promotes the growth of the  $\text{Nb}_5\text{Si}_3$  silicide. Solid solution fractions seemed to be unaffected by the changes molybdenum content when compared to the preliminary results for the 25Cr5B alloy.

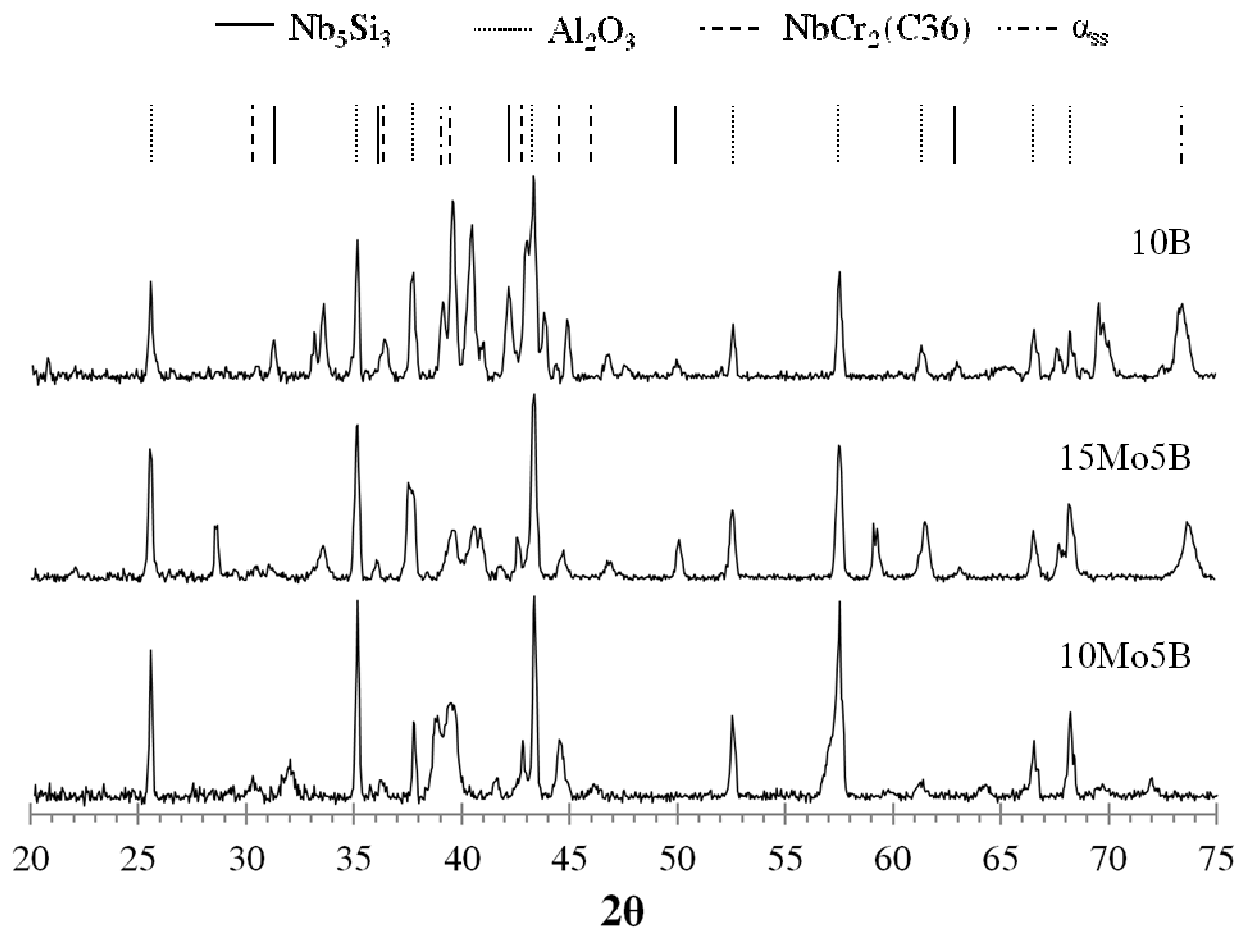


Figure 5.3 XRD spectra collected for Nb-25Cr-15Mo-20Si-5B, Nb-25Cr-20Mo-15Si-10B, and Nb-25Cr-10Mo-15Si-5B alloys. alloy comps in the as cast condition.

Table 5.1 Image analysis results of the as-cast microstructures of the 10Mo5B, 15Mo5B and 10B alloys.

Phase Fractions Calculated at 500X			
Phase	10Mo5B	15Mo5B	10B
Laves	37	48	43
Solid Solution	20	24	unknown
Silicide	43	28	unknown

X-ray mapping was carried out to better understand the distribution of the elements in the as-cast microstructure of each alloy. X-ray maps collected from the 15Mo5B, 10B, and the 10Mo5B alloys are presented in Figure 5.4, 5.5, and 5.6 respectively. The solid solution developed in all three alloys was observed to contain a large amount of molybdenum. Further EDS analysis indicates that the solid solution is molybdenum based in both the 10B and 15Mo5B alloys.

The x-ray maps collected for the 15Mo5B alloy are presented in Figure 5.4. A large concentration of molybdenum in the solid solution phase is clearly shown. The chromium map indicates that most of the chromium in the microstructure is concentrated in the Laves phase and in the solid solution. The niobium map indicates that niobium is mostly concentrated in the solid solution and silicides. Silicon is observed to be concentrated in the silicides as expected.

The x-ray maps collected from the as-cast microstructure of the 10B alloy are presented in Figure 5.5. The maps share many similarities with those of the 15Mo5B alloy with respect to the silicon and niobium distributions. The eutectic like microconstituent was too fine at 1500X to be properly mapped. The chromium map does indicate to some extent the locations of the Laves phase.

X-ray maps collected from the as-cast microstructure of the 10Mo5B alloy are presented in Figure 5.6. The maps share many of the same characteristics with respect to element distribution to those observed in the 15Mo5B alloy. The solid solution is observed to have a high concentration of molybdenum, chromium is observed to be concentrated in the Laves phase, and

silicon is observed to be concentrated in the silicides. Chromium is observed to be completely absent from the silicides this is common in all three alloys.

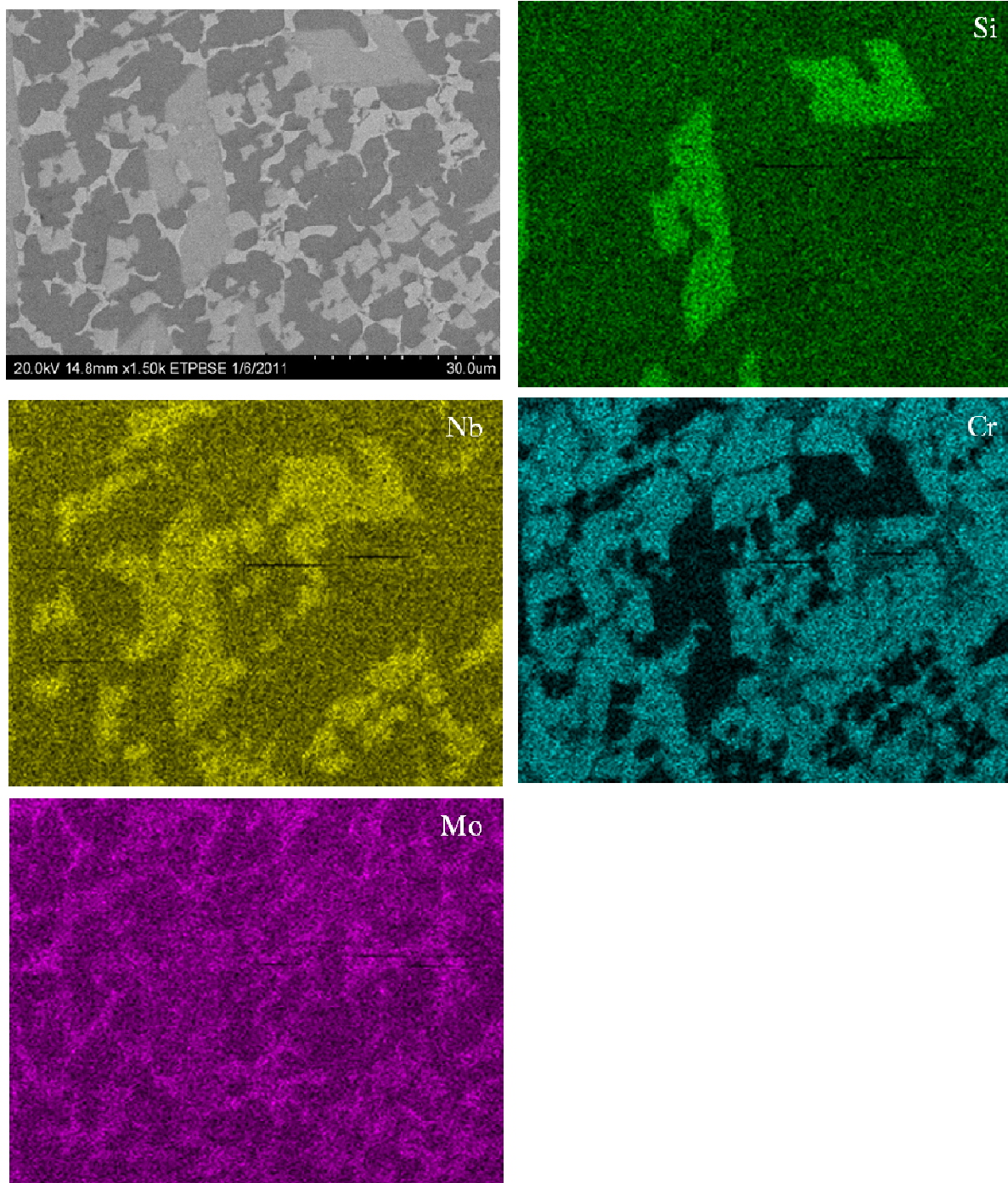


Figure 5.4 X-ray map of Nb-25Cr-15Mo-20Si-5B alloy in the as cast condition at 1500X magnification.



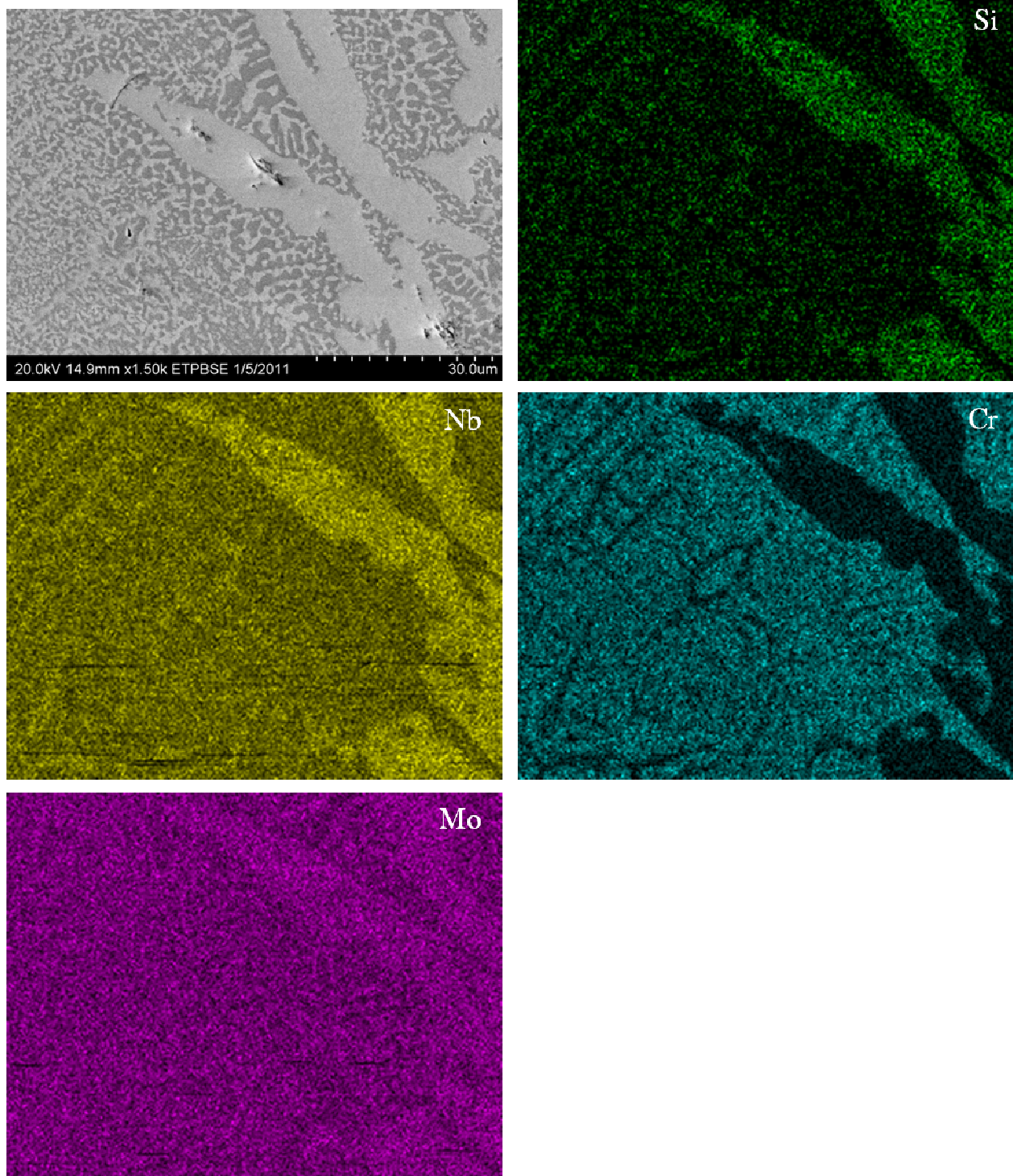


Figure 5.5 X-ray map of Nb-25Cr-20Mo-15Si-10B alloy in the as cast condition at 1500X magnification.

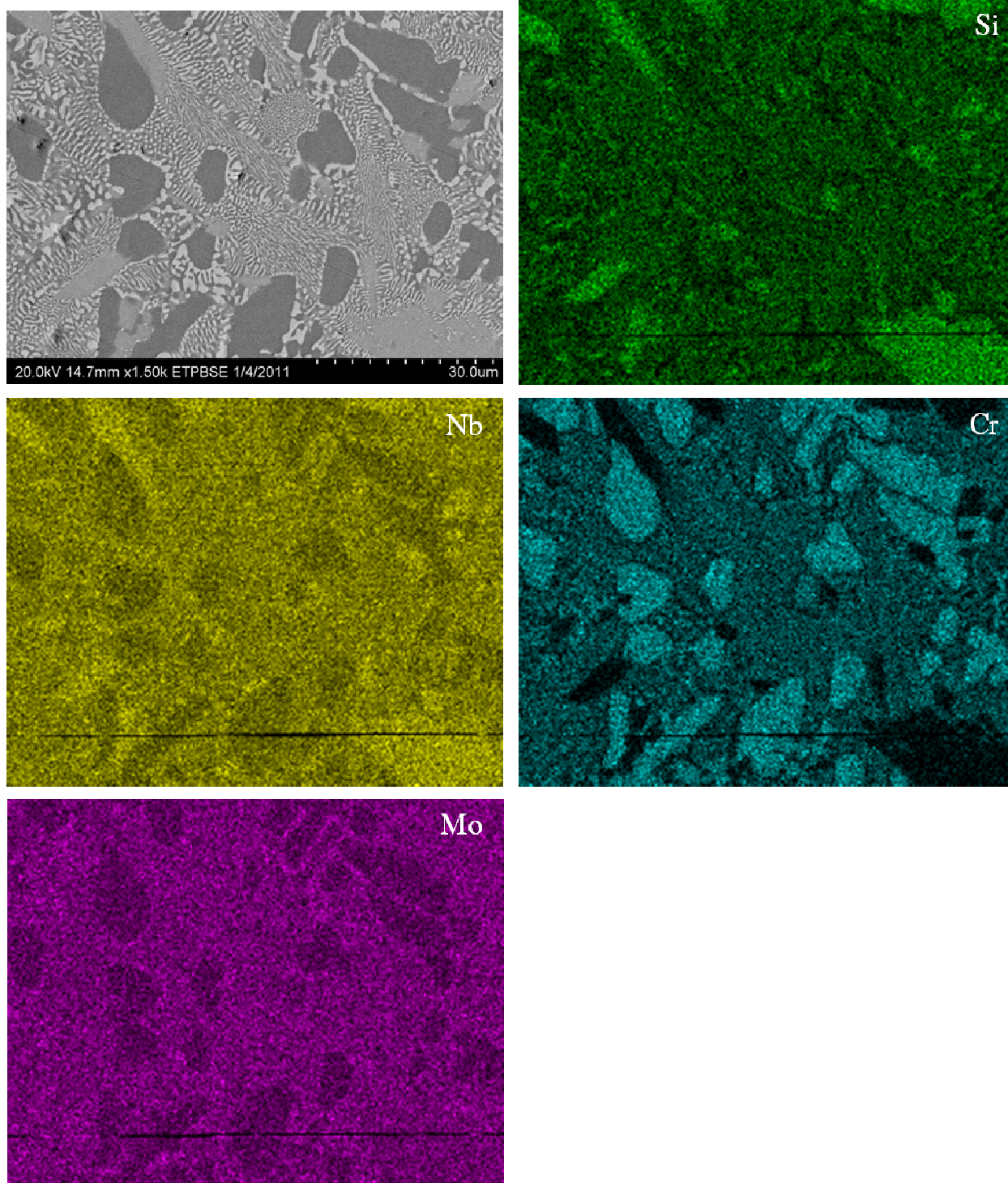


Figure 5.6 X-ray map of Nb-25Cr-10Mo-15Si-5B alloy in the as cast condition at 1500X magnification.



## 5.2 SHORT TERM OXIDATION RESULTS

Short term oxidation results for all three alloys in terms of weight gain per unit area as a function of temperature are presented in Figure 5.7. At 700°C pest oxidation was observed to take place in both the 10Mo5B and 15Mo5B alloys resulting in the disintegration of the entire sample into powder oxide. Oxide metal interfaces developed after short term oxidation at temperatures between 800 and 1000°C are presented in Figures 5.8 and oxide metal interfaces developed at temperatures between 1100 and 1300°C are presented in Figure 5.9. It must be noted that at 1200°C and above stains were observed along the insides of all the sample crucibles indicating that oxide volatilization may have taken place.

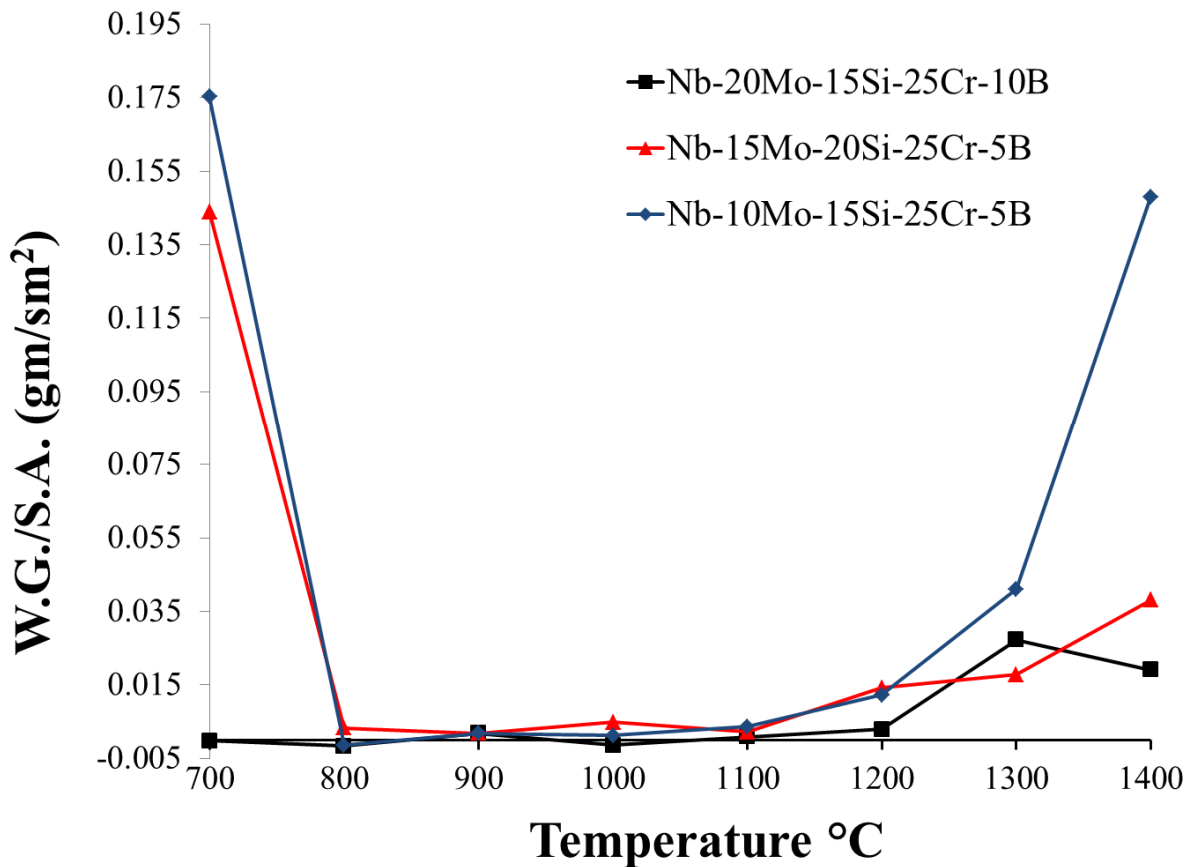


Figure 5.7 Short term oxidation results for 10Mo5B, 15Mo5B, and the 10B alloys from 700 to 1400°C.

Initial observations of the short term oxidation results indicate that the 10B alloy performed the best throughout the experimental temperature range. The oxide scale developed at 700°C could not be observed, there was no oxide metal interface when the sample was sectioned and polished. The oxide products may not have been able to withstand the sectioning and polishing processes. The oxide scales developed on the 10B alloy at temperatures between 800 and 900°C are not continuous as observed in Figure 5.8. The cracks developed at 800°C are believed to have developed upon cooling since no oxide is observed to have grown along the cracks. At 1000°C the oxide scale developed on the 10B alloy is semi continuous and oxides identified are  $\text{CrNbO}_4$  and  $\text{Nb}_2\text{O}_5$ .  $\text{SiO}_2$  is also observed to form amongst the  $\text{CrNbO}_4$  and  $\text{Nb}_2\text{O}_5$  oxides but not along the oxide metal interface. At temperatures between 1100 and 1300°C (Figure 5.9) the oxide developed on the 10B alloy is continuous and the formation of the intermediate oxidation zone previously reported in the preliminary studies can be observed [1]. The development of the intermediate oxidation layers is not completely understood but is believed to be attributed to the outward diffusion of chromium. Previous studies on the oxidation of  $\text{NbCr}_2$  Laves phase alloys indicated that the outward diffusion of chromium was faster than that of niobium [4]. A layer consisting of a matrix of  $\text{SiO}_2$  with dispersed  $\text{CrNbO}_4$  and  $\text{Nb}_2\text{O}_5$  is also observed to form over the intermediate oxidation layer at 1200 and 1300°C. At 1300°C molybdenum solid solution is observed along the intermediate oxidation layer. Cracks are also observed in the metal remaining along the metal oxide interface at 1200 and 1300°C and are also believed to have formed while cooling since no oxide was observed to grow along the cracks. At 1400°C the weight gain appears to drop off and may be related to the volatilization of oxides. The oxide scale and metal oxide interface are presented in Figure 5.10 (a). The intermediate oxidation layer is present and considerably thicker with respect to the morphology of the oxide scales formed at 1200 and 1300°C. Large amounts of  $\text{SiO}_2$  are observed to develop after the intermediate oxidation layer along with  $\text{CrNbO}_4$ . No outer layer of  $\text{Nb}_2\text{O}_5$  was observed much of the oxide scale appears to consist of  $\text{CrNbO}_4$ . Cracks and pores are observed to have developed

along the metal oxide interface and penetrate into the metal remaining. No oxide is observed to grow along the cracks indicating they formed upon cooling.

The large weight gain observed at 700°C in the short term oxidation results of the 15Mo5B alloy, presented in Figure 5.7, can be attributed to the pest oxidation observed and the complete oxidation of the sample. At temperatures between 800 and 1000°C (Figure 5.8) the oxide scales developed on the 15Mo5B alloy are not continuous. At 1000°C the preferential oxidation of the  $\text{Nb}_5\text{Si}_3$  silicide can be observed resulting in large amounts of  $\text{Nb}_2\text{O}_5$  and a discontinuous oxide scale. The oxide metal interfaces developed between 1100 and 1300°C (Figure 5.9) indicate the presence of the intermediate oxidation layer running along the metal oxide interface. At 1200 and 1300°C layered oxide scales are observed as well. Solid solution is observed to be present in the intermediate oxidation layers developed at 1100, 1200, and 1300°C. The morphology of the oxide metal interfaces developed on both the 10B and the 15Mo5b alloy appear to have several characteristics in common including the development of the intermediate oxidation layer along the metal oxide interface starting at 1100°C. At 1400°C the short term oxidation results indicate and increase in weight gain maintaining the steady trend in weight gain observed to start at 1100°C. The oxide metal interface developed at 1400°C presented in Figure 5.10 (b) shows large amounts of  $\text{Nb}_2\text{O}_5$  and  $\text{CrNbO}_4$  as well. The oxide was also observed to be loosely adherent and on the verge of spalling after short term oxidation. Large cracks with respect to those observed in the 10B alloy are observed to form along the metal oxide interface and are also believed to have formed after cooling since no oxide was observed to have developed along the cracks inner surfaces.

The oxide scale developed on the 10Mo5B alloy at 800°C (Figure 5.8) is discontinuous. At 900°C the oxide scale developed is observed to be semi continuous but severely cracked. At 1000°C a continuous oxide layer is developed and the intermediate oxidation layer is observed. The oxide metal interface is also observed to advance uniformly into the metal remaining. No preferential oxidation of the  $\text{Nb}_5\text{Si}_3$  silicide is observed. At 1100°C the oxide scale morphology remains the same as the morphology observed at 1000°C. At 1200°C the oxide scale is observed

to spall and the preferential oxidation of the  $\text{Nb}_5\text{Si}_3$  silicide is observed. The oxide metal interface developed at  $1300^\circ\text{C}$  reveals a crack that runs along the metal oxide interface and is an indication of that the stresses developed by mismatches of thermal expansion coefficients and the molar volume increase between oxide products and un-oxidized phases [5-6]. The  $1400^\circ\text{C}$  sample was unrecoverable, it appears to have melted and fused with the crucible. The data is kept for comparison purposes.

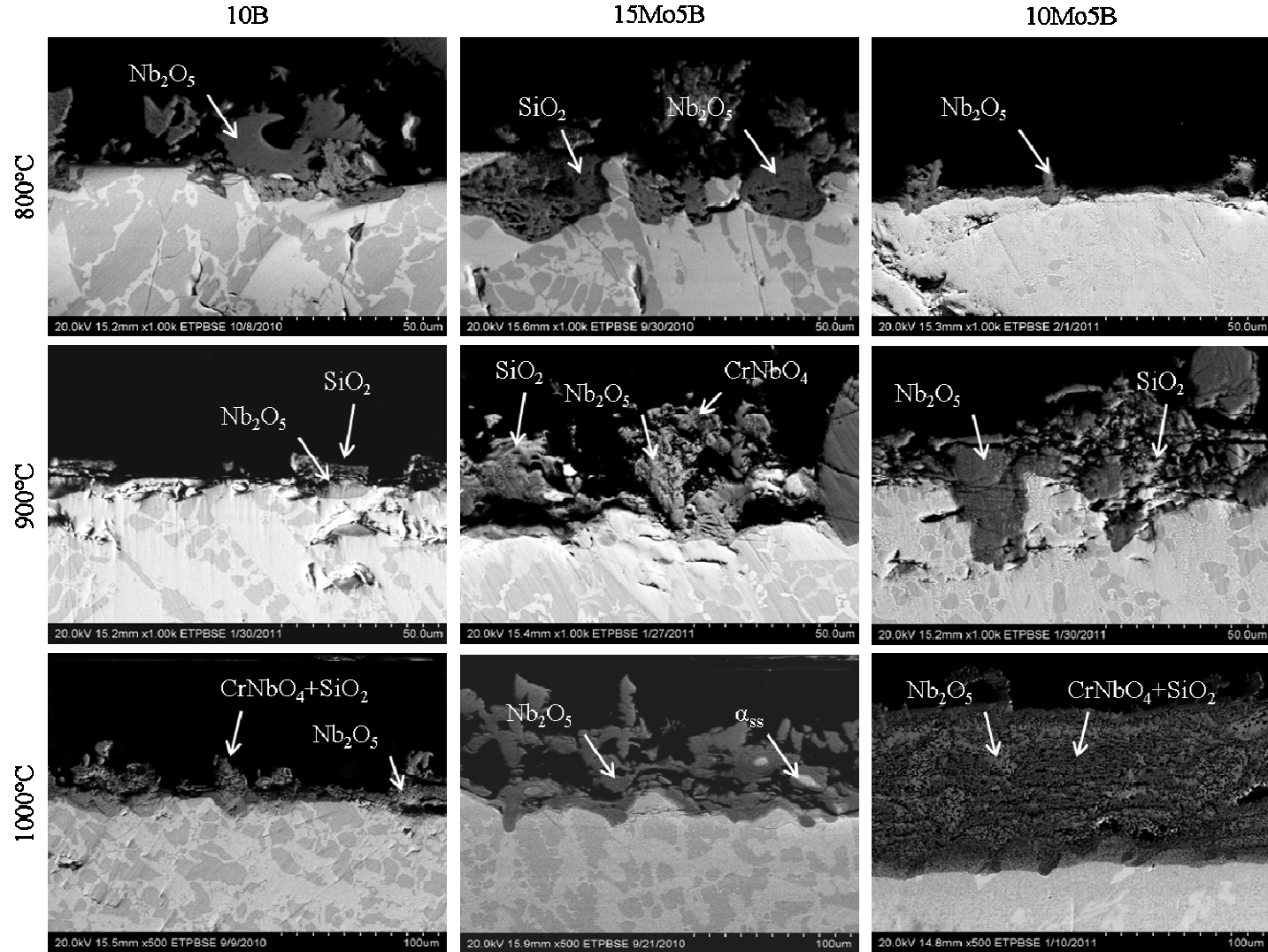


Figure 5.8 Oxide metal interfaces developed after short term oxidation at 800, 900, 1000°C for the 10B, 15Mo5B, and 10Mo5B alloys micrographs collected in back scatter imaging mode.

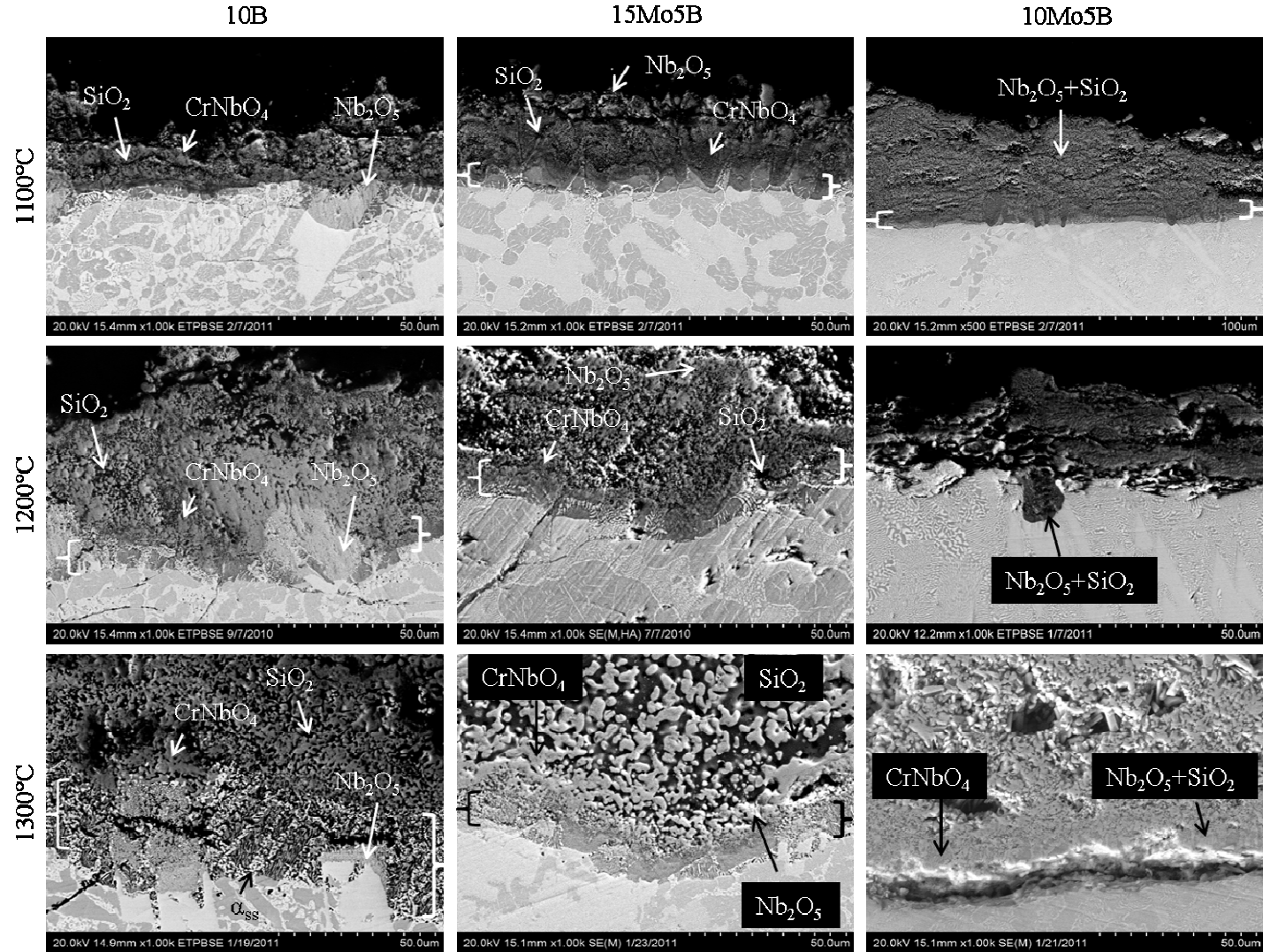


Figure 5.9 Oxide metal interfaces developed after short term oxidation at 1100, 1200, 1300°C for the 10B, 15Mo5B, and 10Mo5B alloys micrographs collected in back scatter imaging mode. White parentheses indicate location of intermediate oxide phase

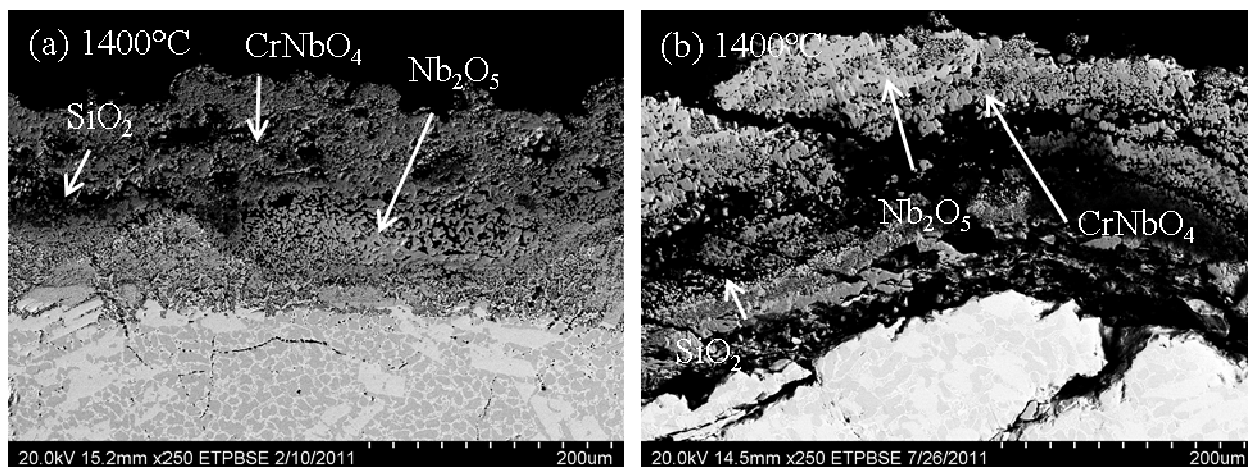


Figure 5.10 Oxide metal interfaces developed after short term oxidation at 1400°C for the (a) 10B alloy and (b) the 15Mo5b alloy.

X-ray diffraction spectra were collected from the surface oxide products at all temperatures. Two oxides were common at all temperatures those being  $\text{Nb}_2\text{O}_5$  in its monoclinic form and  $\text{CrNbO}_4$ . The spectra collected from the oxidation products after short term oxidation at 800°C are presented in Figure 5.11, and the spectra collected from the oxidation products after oxidation at 1200°C are presented in Figure 5.12. There was no indication of the presence of molybdenum based oxides, possibly due to the volatile nature of the  $\text{MoO}_3$  oxide which was reported to volatilize at temperatures above 600°C [7, 8]. No crystalline boron oxides are observed in the spectra. The volatilization of  $\text{B}_2\text{O}_3$  may have been possible at temperatures above 1200°C since it has been reported to volatilize at 1000°C [9]. The spectra collected at 1200°C shows lower intensities for the reflections associated with  $\text{Nb}_2\text{O}_5$  indicates that the outer oxide layer formed is  $\text{CrNbO}_4$ . No crystalline form of  $\text{SiO}_2$  was detected in the surface oxides even though it was identified by EDS analysis. EDS analysis indicates the presence of boron in the  $\text{Nb}_2\text{O}_5$  and in the solid solution in the un-oxidized microstructure but not in  $\text{SiO}_2$ . Examples of the EDS spectra collected from 10B alloy after short term oxidation 1200°C are presented in Figure 5.13. It must be noted that the analysis of boron content are qualitative given the disparity in atomic weight between the alloying constituents. These results cannot be used to determine

whether the observed  $\text{SiO}_2$  is borosilicate glass or not and should not be interpreted as an indication that no borosilicate is present. The concentration may not be detectable by the EDS interment.

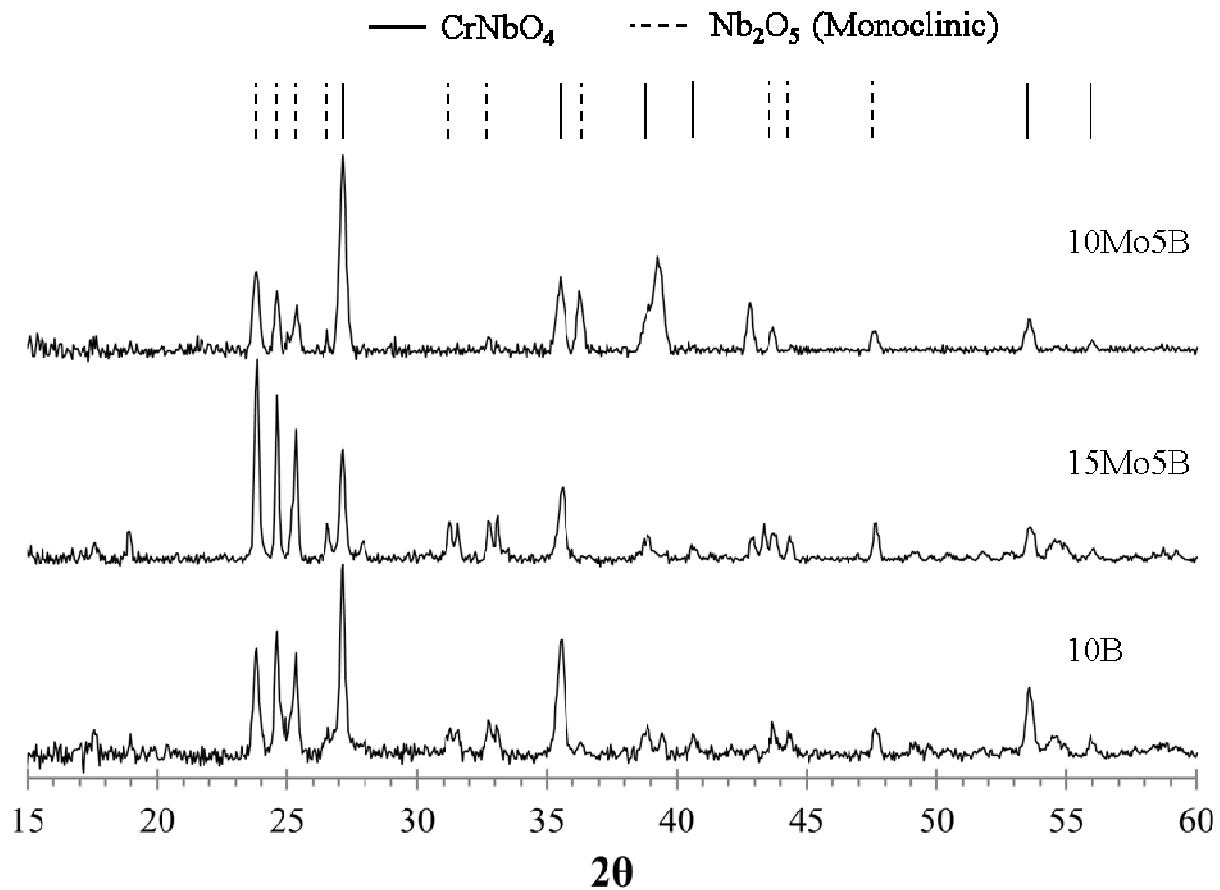


Figure 5.11 XRD spectra collected at 800°C of the surface oxides after short term oxidation of the 10B, 15Mo5B, and 10Mo5B alloys.



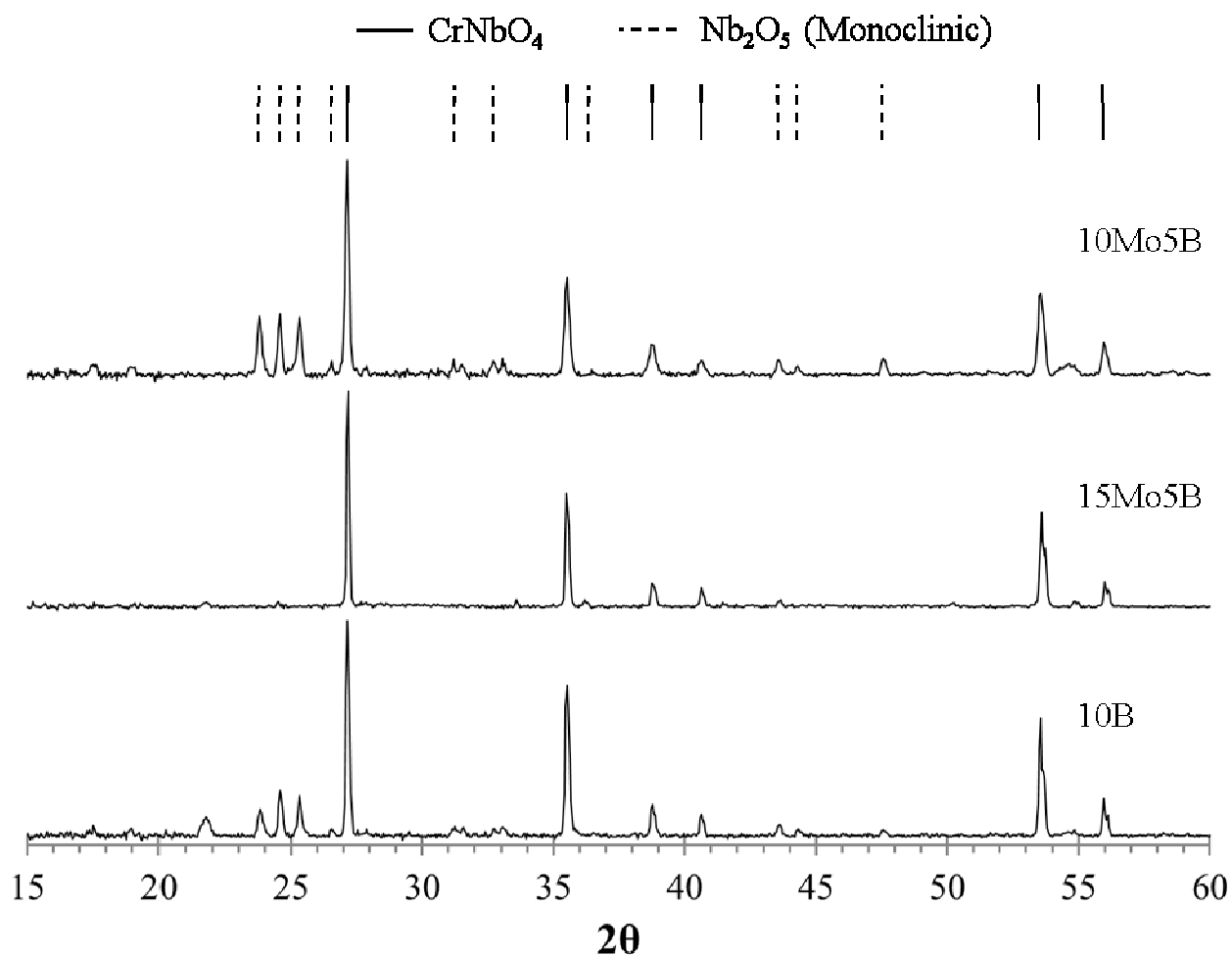


Figure 5.12 XRD spectra collected at 1200°C of the surface oxides after short term oxidation of the 10B, 15Mo5B, and 10Mo5B alloys.

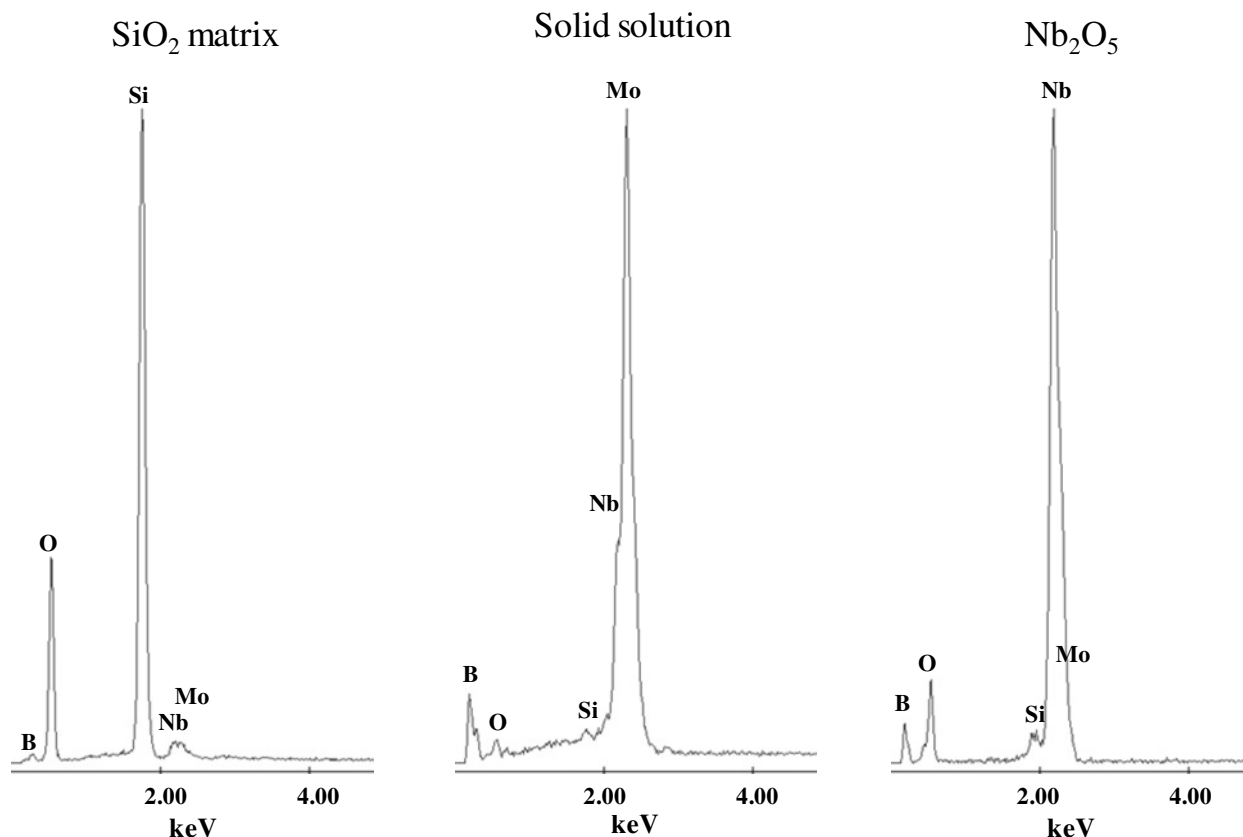


Figure 5.13 EDS spectra collected from the Nb-25Cr-20Mo-15Si-10B alloy after 24 hrs of oxidation at 1200°C. The SiO<sub>2</sub> matrix spectra was collected from the SiO<sub>2</sub> layer with dispersed CrNbO<sub>4</sub> oxide. The solid solution spectra was collected from the remaining molybdenum solid solution in the intermediate oxidation layer. The Nb<sub>2</sub>O<sub>5</sub> spectrum was collected near the SiO<sub>2</sub> matrix closest to the air oxide interface.

### 5.3 THERMAL GRAVIMETRIC CHARACTERIZATION

Thermal gravimetric analysis was carried on the 10B and 15Mo5B alloys at 800, 1000, and 1200°C for 24 hours, results are presented in Figures 5.14, 5.15, and 5.16 respectively. Thermal gravimetric analysis of the 10Mo5B alloy was not carried out. At 800°C the oxidation behavior observed for the 10B alloy was linear for the first three hours of oxidation followed by a parabolic trend. The oxidation behavior of the 15Mo5B alloy was observed to be linear. The parabolic rate constant was calculated after the initial linear weight gain for the 10B alloy to be

16.98  $\text{mg}^2/\text{cm}^4/\text{hr}$ . The linear rate constant for the 15Mo5B alloy was calculated to be 0.0013  $\text{mg}/\text{cm}^2/\text{hr}$ . The linear oxidation behavior indicates that the discontinuous oxide scale observed to develop at 800°C in Figure 5.14 does not provide the 15Mo5B alloy any protection and the oxidation kinetics are not controlled by the diffusion of oxygen through the discontinuous oxide scale.

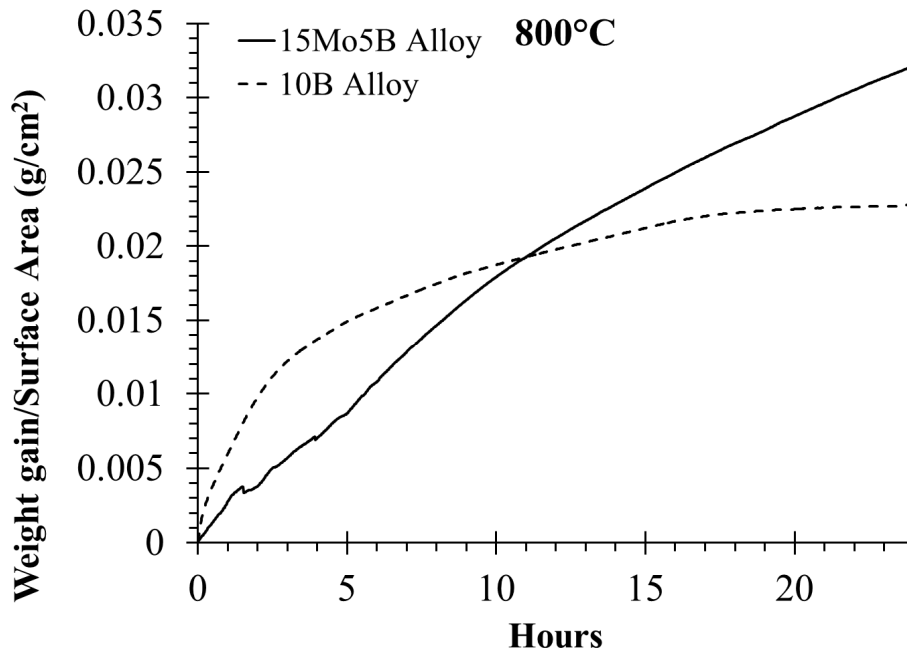


Figure 5.14 Thermal gravimetric results collected for Nb-25Cr-15Mo-20Si-5B and Nb-25Cr-20Mo-15Si-10B alloys at 800°C for 24 hours.

The results collected from the oxidation at 1000°C are presented in Figure 5.15 and indicate that both the 15Mo5B alloy and the 10B alloy had similar oxidation responses. A large initial weight gain is observed followed by slight mass loss. After the mass loss the weight gain is observed to be linear. Linear rate constants for the 15Mo5B alloy and the 10B alloy were found to be 0.00042 and 0.00044  $\text{mg}/\text{cm}^2/\text{hr}$ , respectively. Additional oxidation time may be required for the oxidation process to become diffusion controlled at 1000°C since the oxide scales observed to develop were continuous.

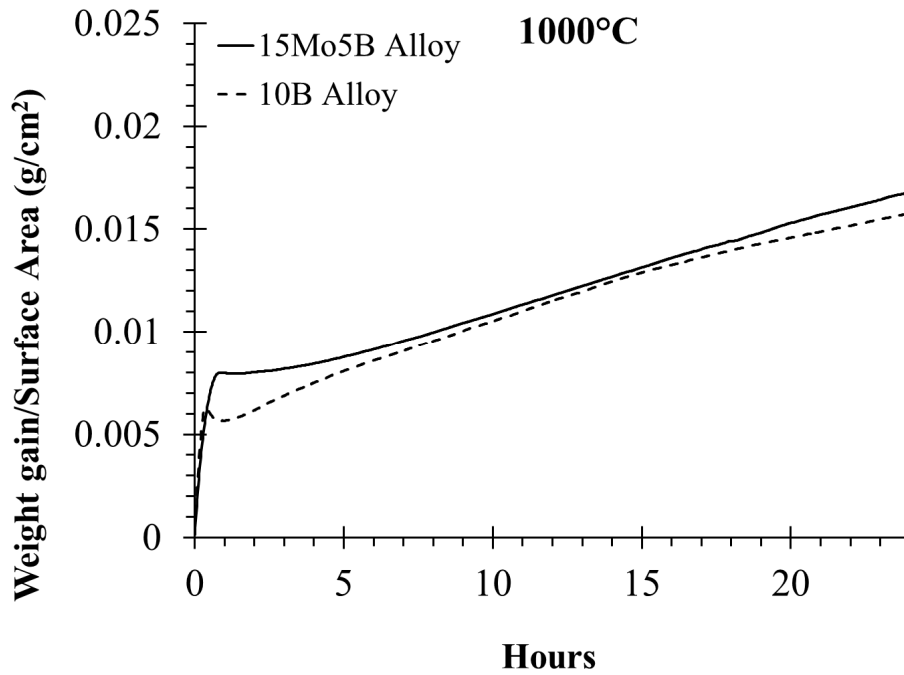


Figure 5.15 Thermal gravimetric results collected for Nb-25Cr-15Mo-20Si-5B and Nb-25Cr-20Mo-15Si-10B alloys at 1000°C for 24 hours.

Results collected from the 1200°C oxidation are presented in Figure 5.16, and indicate transient oxidation behavior in both alloys. Initial weight gain is linear followed by mass loss and then a continuous parabolic oxidation behavior is observed. Parabolic rate constants were calculated after the mass loss for both the 15Mo5B alloy and the 10B alloy to be 44.59 and 8.00  $\text{mg}^2/\text{cm}^4/\text{hr}$  respectively. These results indicate that the oxidation kinetics are diffusion controlled after the first few hours of oxidation given the parabolic nature of the oxidation data. The mass loss observed in both alloys at 1200°C may be the result of oxide volatilization.

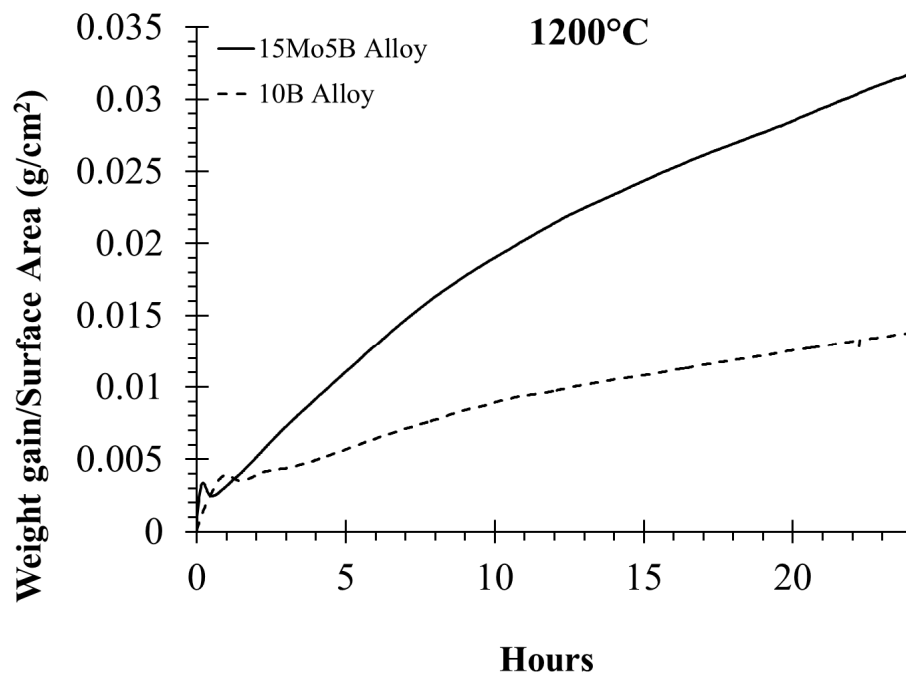


Figure 5.16 Thermal gravimetric results collected for Nb-25Cr-15Mo-20Si-5B and Nb-25Cr-20Mo-15Si-10B alloys at 1200°C for 24 hours.

## 5.4 OXIDE SCALE DEVELOPMENT

To examine the transient oxidation behavior observed at 1200°C the oxide scale development studies were performed. The development of the oxide scales on the 10B, 15Mo5B, and 10Mo5B alloy were examined at 900 and 1200°C. The surface oxide morphology developed at 900°C is presented in Figure 5.17. The oxides developed were identified as  $\text{Nb}_2\text{O}_5$  and  $\text{CrNbO}_4$  and are common to all three alloys. The flat portions in the micrographs were found to be  $\text{CrNbO}_4$  while the protruding structures were found to be  $\text{Nb}_2\text{O}_5$  according to EDS analysis. The morphology of the oxides retain characteristics from the as cast microstructure, this becomes evident with the morphology of the protruding oxide structures are compared to the morphology of the silicides observed in the as cast microstructures. The surface oxide morphology developed at 1200°C is presented in Figure 5.18. All alloys seem to retain similar characteristics to those observed at 900°C. The flat portions of the micrographs are locations where  $\text{CrNbO}_4$  was observed to form and the protruding oxides were observed to be  $\text{Nb}_2\text{O}_5$ .

The samples were cross sectioned to reveal the oxide metal interface. The oxide metal interfaces developed on the 10B alloy are presented in Figure 5.19. A patchy oxide scale consisting mostly of  $\text{Nb}_2\text{O}_5$  is observed to develop at 900°C. At 1200°C the onset of the intermediate oxidation layer is observed. The  $\text{Nb}_5\text{Si}_3$  silicide appears to be preferentially attacked since it appears as though the oxide metal interface advances into the metal farther in areas along the interface where the silicide is present in comparison to the areas along the interface that contain  $\text{NbCr}_2$ .  $\text{SiO}_2$  is also observed to start forming from the oxidized  $\text{Nb}_5\text{Si}_3$  silicide.

The cross-sections from the 15Mo5B alloy presented in Figure 5.20 reveal a discontinuous bulky oxide consisting of a mixture of  $\text{Nb}_2\text{O}_5$  and  $\text{SiO}_2$  at 900°C. Also at 900°C a thin layer of  $\text{CrNbO}_4$  was observe to develop on the Laves phase and solid solution along the oxide metal interface. At 1200°C the oxide scale developed is also discontinuous and consisted of a mixture of  $\text{Nb}_2\text{O}_5$  and  $\text{SiO}_2$ . The  $\text{Nb}_5\text{Si}_3$  silicide was observed to be preferentially attacked

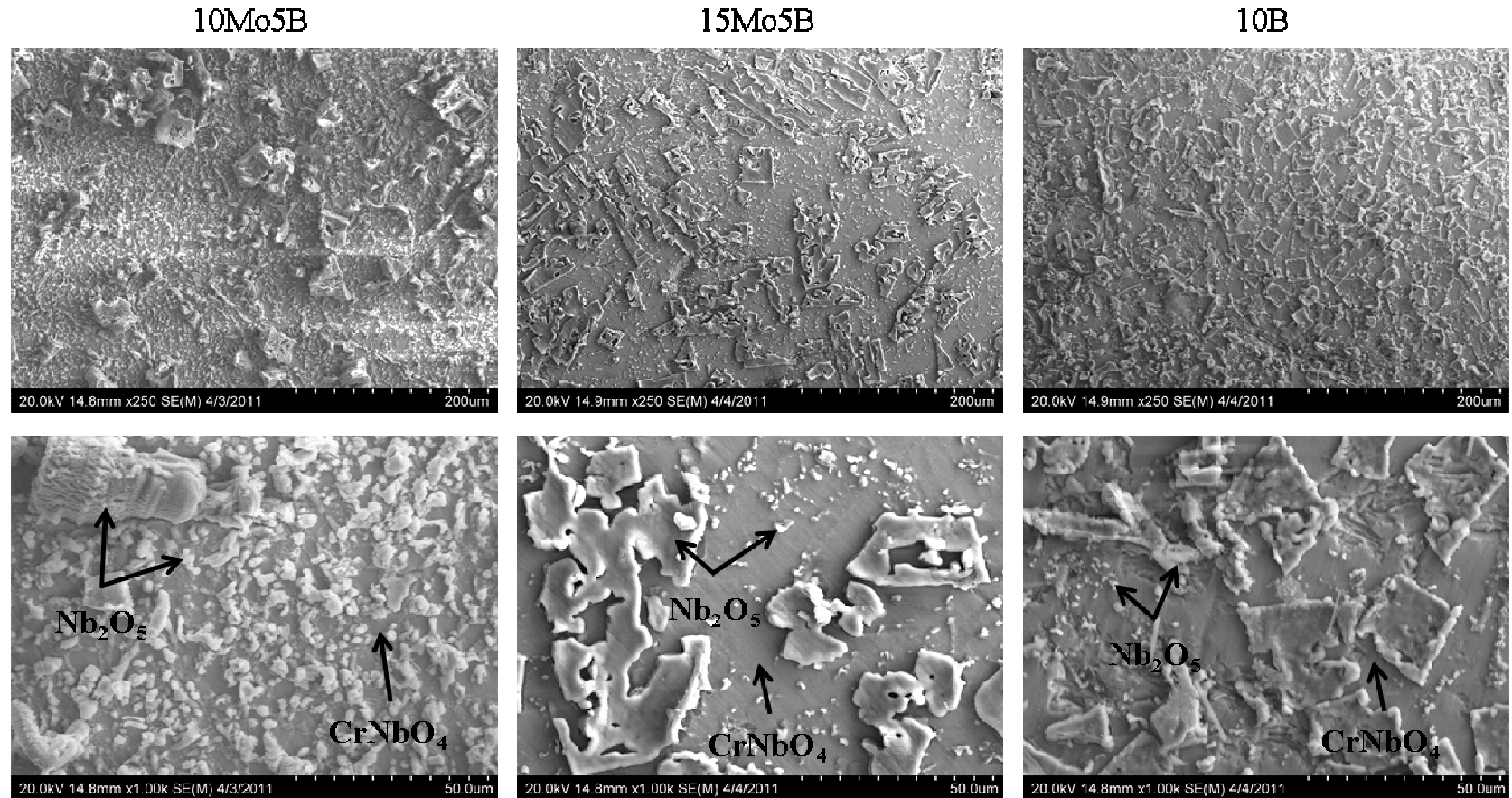


Figure 5.17 Micrographs at 250X and 1000X of the surface oxides developed on the 10B, 15Mo5B, and 10Mo5B alloys after a 10°C/min ramp to 900°C and 10 minutes of oxidation followed by an air quench.

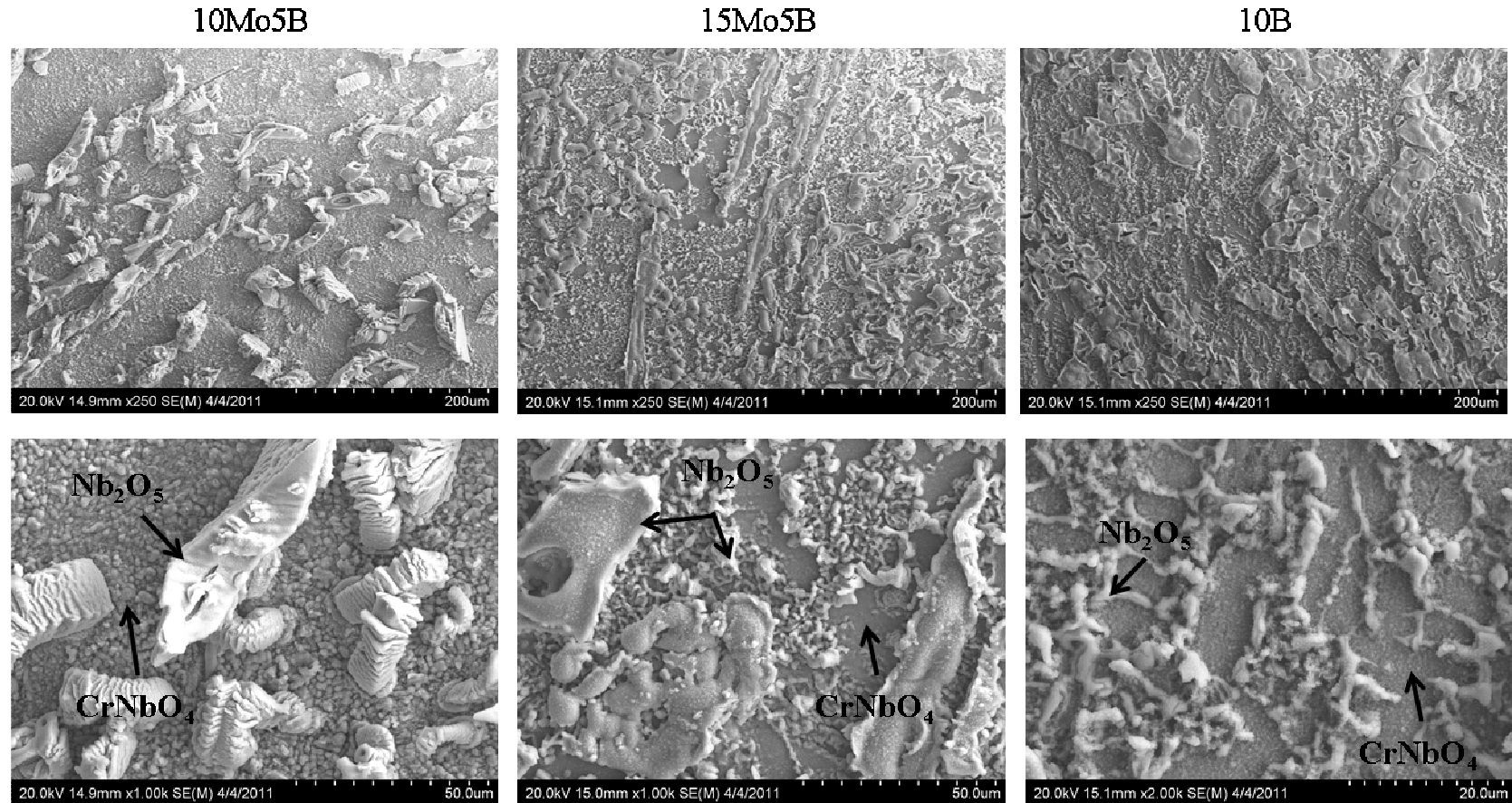


Figure 5.18 Micrographs at 250X and 1000X of the surface oxides developed on the 10B, 15Mo5B, and 10Mo5B alloys after a 10°C/min ramp to 1200°C and 10 minutes of oxidation followed by an air quench.



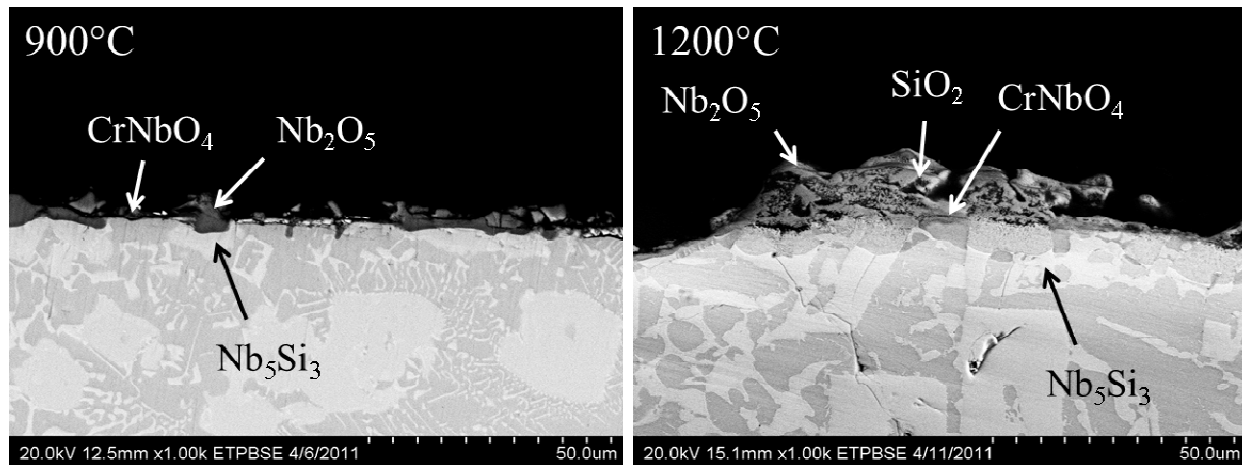


Figure 5.19 Back scatter micrographs of oxide metal interface developed on the 10B alloy after 10 minutes of oxidation at 900 and 1200°C.

but to a larger extent to what was observed in the 10B alloy. The preferential oxidation of the  $\text{Nb}_5\text{Si}_3$  silicide is observed to penetrate past the oxide metal interface and well into the metal. The intermediate oxidation layer can also be observed to be fully developed at 1200°C. A closer examination of the  $\text{Nb}_2\text{O}_5$  and  $\text{SiO}_2$  mixture is presented in Figure 5.21. The high magnification micrograph reveals the morphology of the mixture of  $\text{Nb}_2\text{O}_5$  and  $\text{SiO}_2$  that was developed from the  $\text{Nb}_5\text{Si}_3$  silicide.

The cross-sections from the 10Mo5B alloy are presented in Figure 5.22 and reveal similar oxide morphologies to the 10B alloy. A thin discontinuous oxide scale is observed to develop at 900°C. However, the preferential oxidation of the  $\text{Nb}_5\text{Si}_3$  can be observed to take place and to a larger extent to what was observed in both the 15Mo5B and the 10B alloy. At 1200°C the oxide morphology remains similar to what was observed at 900°C with the exception of the development of  $\text{CrNbO}_4$  over the Laves phase. A similar mixture of  $\text{Nb}_2\text{O}_5$  and  $\text{SiO}_2$  can be observed to develop in the preferentially oxidize  $\text{Nb}_5\text{Si}_3$  silicide.

The observed transient oxidation behavior in the thermal gravimetric results at 1200°C can be attributed to the preferential oxidation of the  $\text{Nb}_5\text{Si}_3$  silicide resulting in the formation of  $\text{Nb}_2\text{O}_5$ . The high oxygen diffusivity and porosity of  $\text{Nb}_2\text{O}_5$  has been well documented [10-13].

Thus it may be possible for oxygen to attack the  $\text{NbCr}_2$  phase and solid solution along the interfaces where  $\text{Nb}_5\text{Si}_3$  has been oxidized to form  $\text{Nb}_2\text{O}_5$  and  $\text{SiO}_2$  leading to an accelerated oxidation rate at the onset of oxidation. The shorter path needed to attack the un-oxidized metal would account for the large initial weight gain observed in the gravimetric results collected at  $1200^\circ\text{C}$  for both the 15Mo5B and the 10B alloys. After accelerated oxidation has taken place and a semi protective scale forms and the volatilization of oxides causes the decrease in weight accounting for the subsequent weight loss observed in Figure 5.16. After these two processes have taken place the oxide kinetics stabilize and continue in a parabolic manner. Figure 5.23 shows a schematic representation of the process.

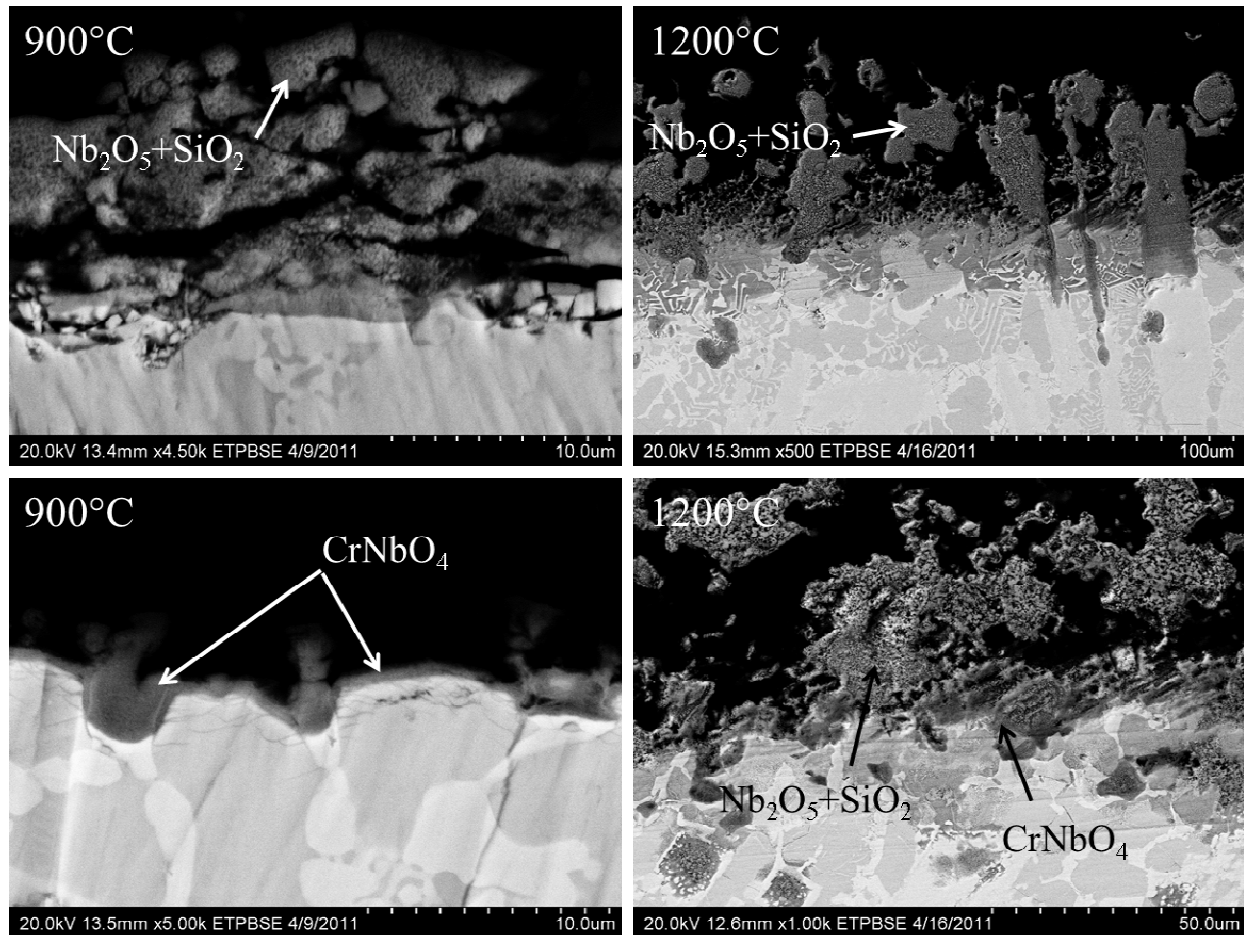


Figure 5.20 Back scatter micrographs of oxide metal interface developed on the 15Mo5B alloy after 10 minutes of oxidation at 900 and  $1200^\circ\text{C}$ . A thin layer of  $\text{CrNbO}_4$  is observed to form over the Laves phase and solid solution phases at  $900^\circ\text{C}$ .

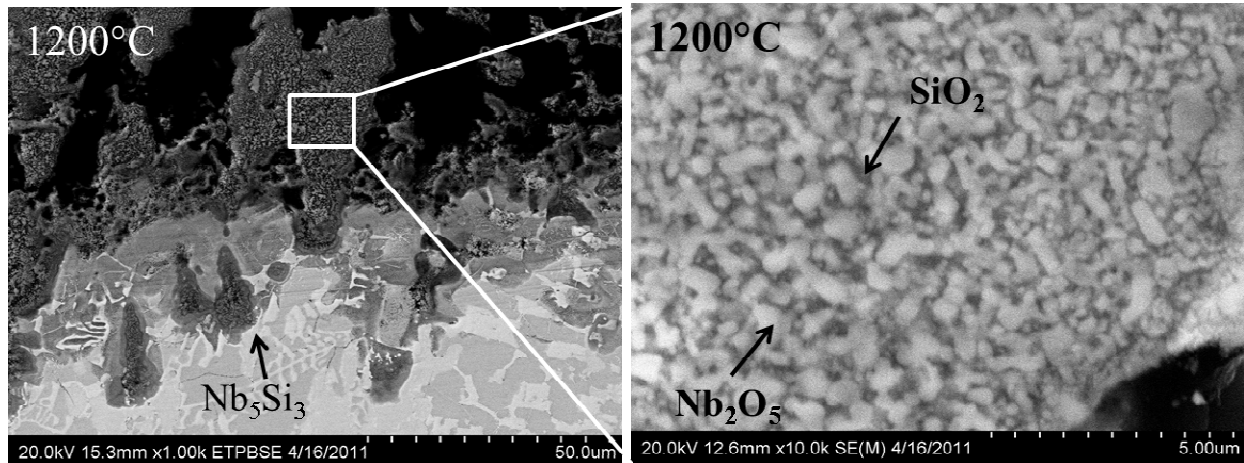


Figure 5.21 Closer examination of the  $\text{SiO}_2$   $\text{Nb}_2\text{O}_5$  oxide mixture developed on the 15Mo5B alloy after 10 minutes of oxidation at 1200°C. The mixture was observed to form from the  $\text{Nb}_5\text{Si}_3$  silicide.

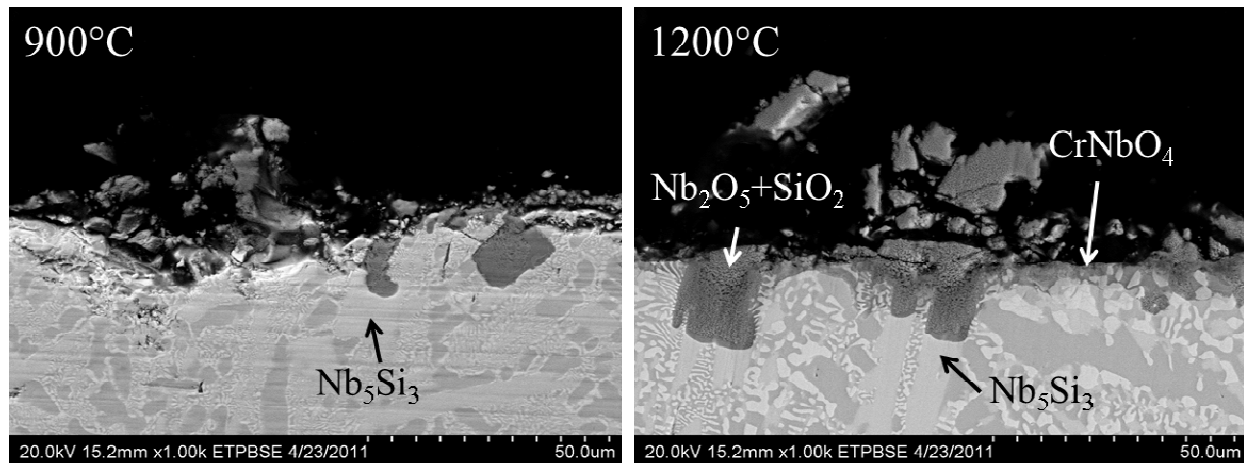


Figure 5.22 Back scatter micrographs of oxide metal interface developed on the 10Mo5B alloy after 10 minutes of oxidation at 900 and 1200°C.

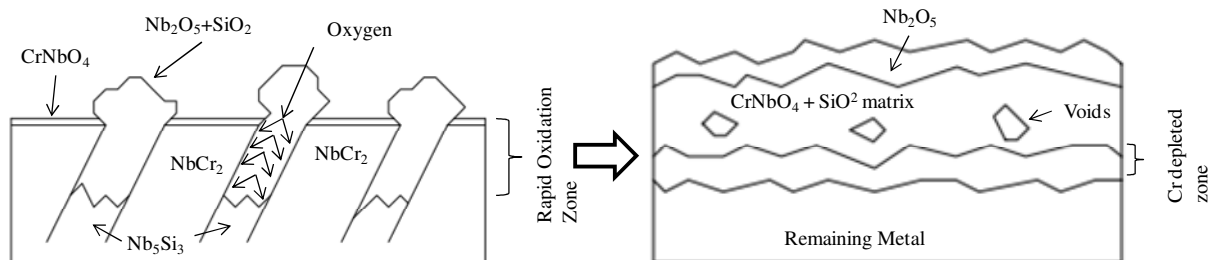


Figure 5.23 Schematic representation of rapid oxidation process responsible for transient oxidation behavior indicated by thermal gravimetric results.

## 5.5 LONG TERM CYCLIC OXIDATION

The long term cyclic oxidation behavior was examined at 700, 1000, 1300, and 1400°C for a total of 168 hours results are presented in Figures 5.24 – 5.27. Only the 10B alloy was subjected to long term cyclic oxidation at 700°C since the 15Mo5B and 10Mo5B were found to suffer from catastrophic pest oxidation after only 24 hours as mentioned in a previous section. The cyclic oxidation was performed in 24 hour intervals till a total of 168 hours of oxidation had been achieved. Macroscopic images were collected of the oxidation products and are presented in Figures 5.28 -5.30.

Figure 5.24 presents the long term cyclic oxidation data collected for the 10B alloy at 700°C. The data indicates that the oxidation response was linear. A linear rate constant of 0.034 mg/cm<sup>2</sup>/hr was determined from the data presented in Figure 5.24. Macroscopic views of the oxide products after long term oxidation are presented in Figure 5.28. It should be noted that the two macroscopic images for the 15Mo5B and 10Mo5B alloys (Figure 5.28 (b) and (c)) were taken after only 24 hours of oxidation, then entire sample had disintegrated into a fine oxide powder.

Figure 5.25 presents the long term cyclic oxidation data collected for all alloys at 1000°C. The 10B and 10Mo5b alloy cyclic data indicates that the oxidation response was linear. The linear rate constant for the 10B alloy was determined to be 0.015 and 0.099 mg/cm<sup>2</sup>/hr for the 10Mo5B alloy. Macroscopic views of the oxide products for the 20Mo10B and 10Mo5b alloys after long term cyclic oxidation are presented in Figure 5.29 (a) and (c). A continuous

oxide scale was observed to form on these two alloys. There was some evidence of pest oxidation for the 10Mo5b alloy but nothing catastrophic. The cyclic oxidation data for the 15Mo5B indicates that the oxidation response was parabolic, but the oxide products presented in Figure 5.29 (b) indicate catastrophic pest oxidation. The parabolic response can be attributed to competing oxide mechanisms [14, 15]. As the sample oxidized  $\text{Nb}_2\text{O}_5$  and  $\text{CrNbO}_4$  are generated, however, several other volatile oxides can form simultaneously causing a mass loss in the sample thus modifying the oxidation kinetics.

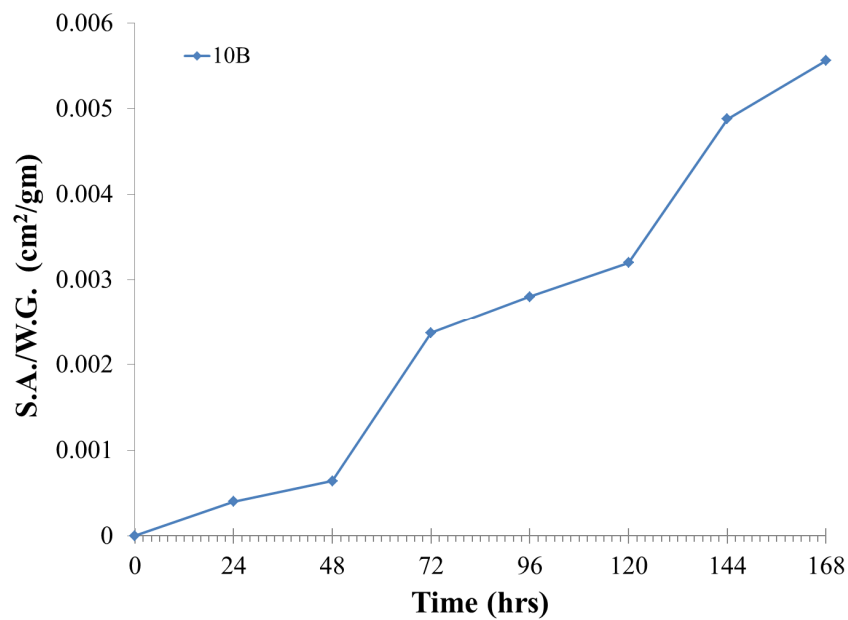


Figure 5.24 700°C long term cyclic oxidation results for the 10B alloy.

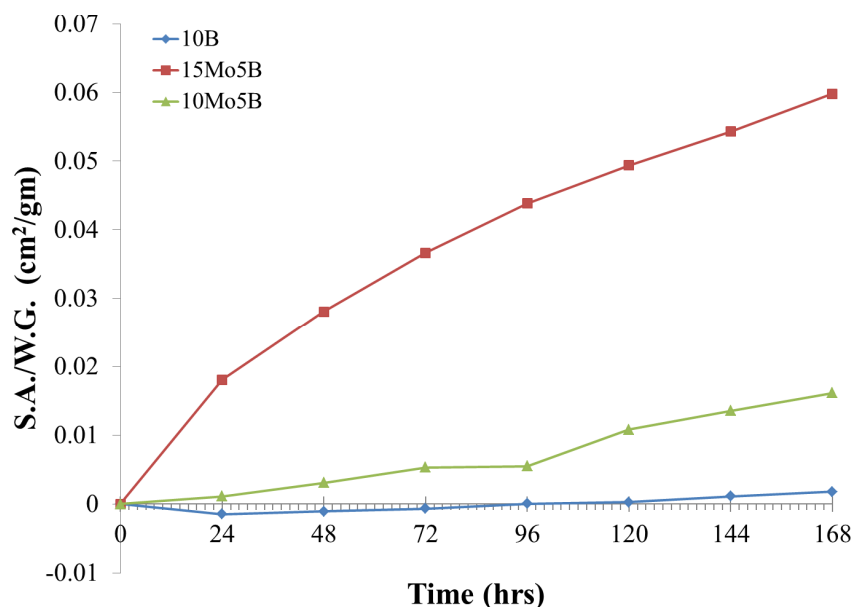


Figure 5.25 1000°C long term cyclic oxidation results for the 10B, 15Mo5B, and 10Mo5B alloy.

Figure 5.26 presents the long term cyclic oxidation data collected for all alloys at 1300°C. The oxidation response for the 10B alloy was observed to follow the parabolic rate law. A parabolic rate constant of  $6.386 \text{ mg}^2/\text{cm}^4/\text{hr}$  was determined for the cyclic oxidation of the 10B alloy. The sample was sectioned and found to contain approximately 60% of the original sample. The oxide metal interface developed for the 10B alloy is presented in Figure 5.31 (a), the morphology is very similar to what was observed in the interfaces developed after short term oxidation. The oxidation response for both the 15Mo5B and the 10Mo5B were mixed linear and parabolic. However, the macroscopic oxidation products indicate that the sample was completely consumed and that spalling of the oxides occurred as evident by the images presented in Figure 5.30 (b) and(c). The oxide scale observed on the 10B alloy was continuous and did not show any evidence of spalling or pest oxidation Figure 5.30 (a).

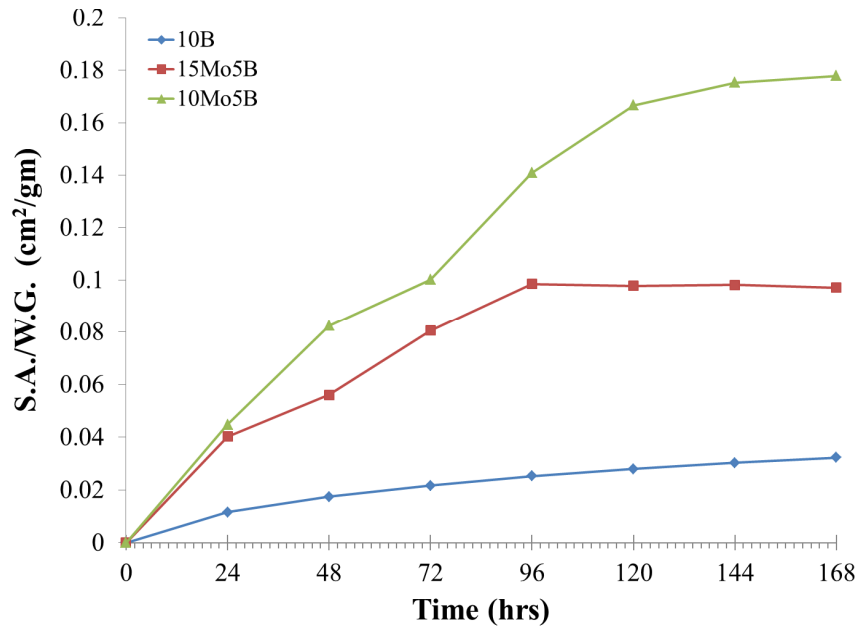


Figure 5.26 1300°C long term cyclic oxidation results for the 10B, 15Mo5B, and 10Mo5B alloy.

Figure 5.27 presents the long term cyclic oxidation data collected for all alloys at 1400°C. The oxidation data for both the 15Mo5B alloy and the 10Mo5B alloy indicate a linear response after a large initial weight gain. The 10Mo5B alloy demonstrates a linear weight gain, when the sample was sectioned none of the sample was found to have survived. The 15Mo5B alloy demonstrates a linear weight loss after a large initial weight gain. When the sample was sectioned none of the sample was found to have survived. The first 96 hours of cyclic oxidation data for the 10B alloy was observed to follow the parabolic rate law, a parabolic rate constant of  $11.2 \text{ mg}^2/\text{cm}^4/\text{hr}$  was calculated from the cyclic data. The sample was sectioned and found to contain approximately 45% of the original sample. The oxide metal interface developed for the 10B alloy is presented in Figure 5.31 (b), the morphology is also similar to the oxide metal interface developed after short term oxidation.

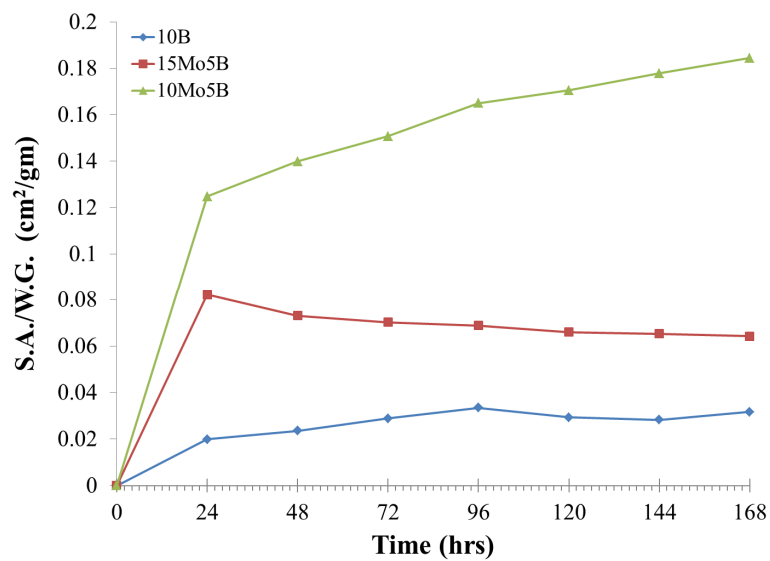


Figure 5.27 1400°C long term cyclic oxidation results for the 10B, 15Mo5B, and 10Mo5B alloy.

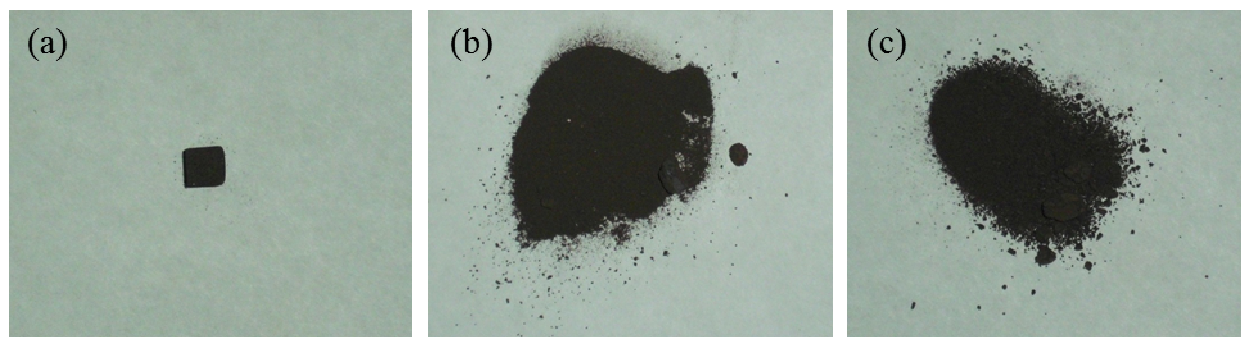


Figure 5.28 Oxidation products after long term cyclic oxidation at 700°C for (a) 10B, (b) 15Mo5B, and (c) 10Mo5B alloys.

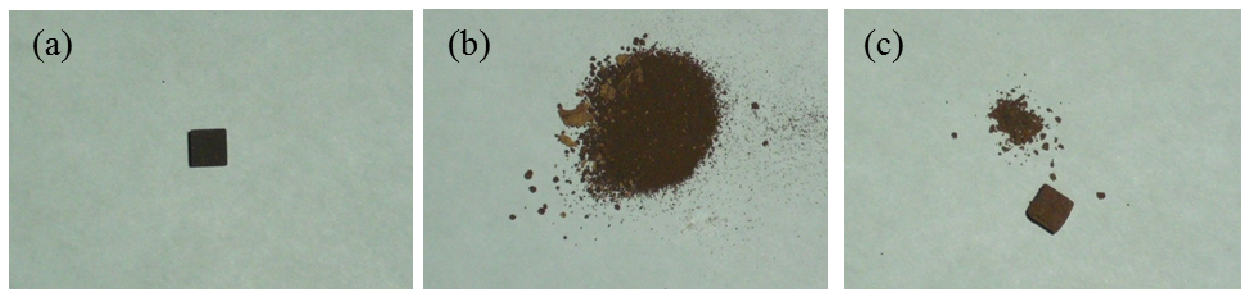


Figure 5.29 Oxidation products after long term cyclic oxidation at 1000°C for (a) 10B, (b) 15Mo5B, and (c) 10Mo5B alloys.



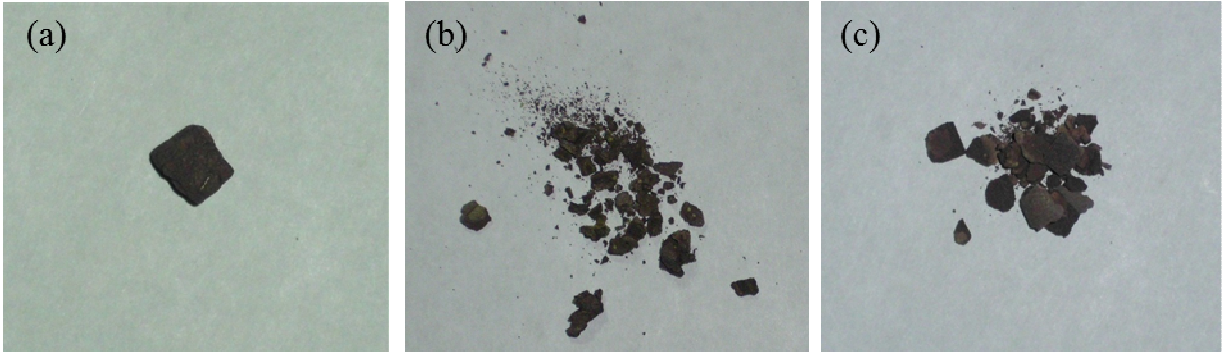


Figure 5.30 Oxidation products after long term cyclic oxidation at 1300°C for (a) 10B, (b) 15Mo5B, and (c) 10Mo5B alloys.

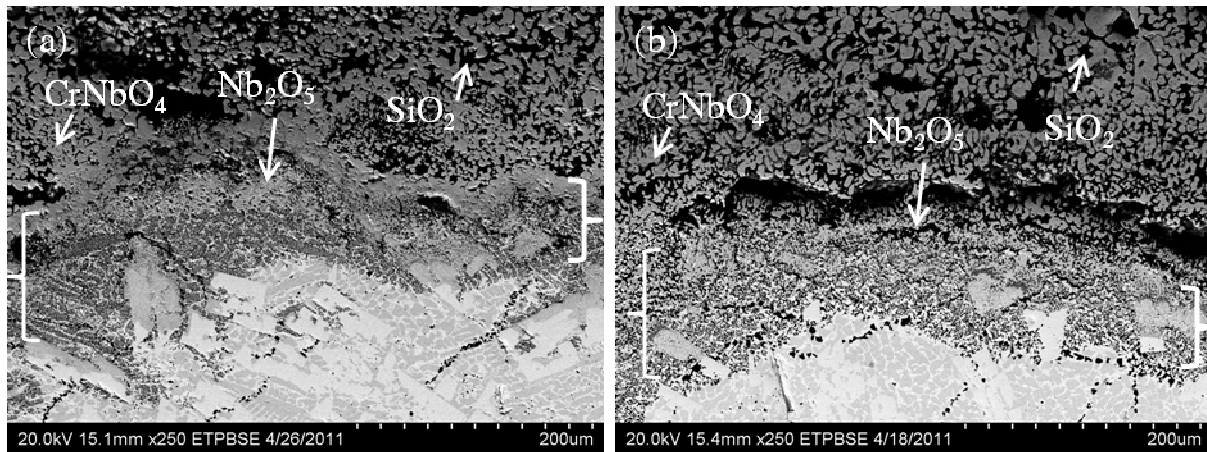


Figure 5.31 Oxide metal interfaces developed for the 10B alloy after long term cyclic oxidation at (a) 1300°C and (b) 1400°C.

X-ray diffraction spectra were collected from the oxidation products formed after long term cyclic oxidation at 700, 1000, and 1300°C for the 10B, 15Mo5B, and 10Mo5B alloy and are presented in Figure 5.32, 5.33, and 5.34 respectively. Two common oxides are present  $\text{CrNbO}_4$  and  $\text{Nb}_2\text{O}_5$  in its monoclinic form. The intensity of the  $\text{Nb}_2\text{O}_5$  peaks is observed to decrease as a function of temperature for all compositions.

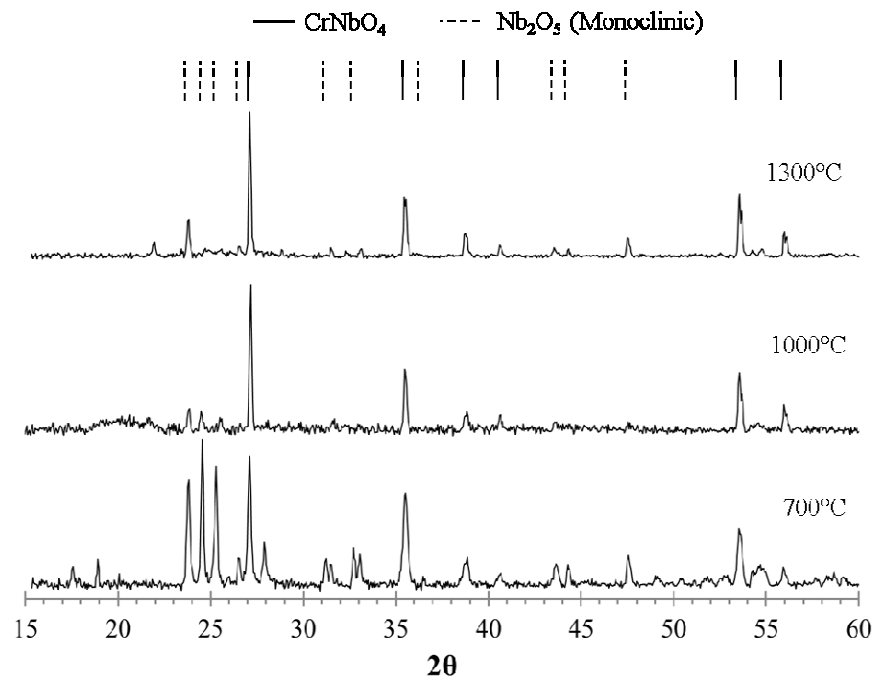


Figure 5.32 XRD spectra collected from oxide products after long term cyclic oxidation at 700, 1000, and 1300°C of the 10B alloy

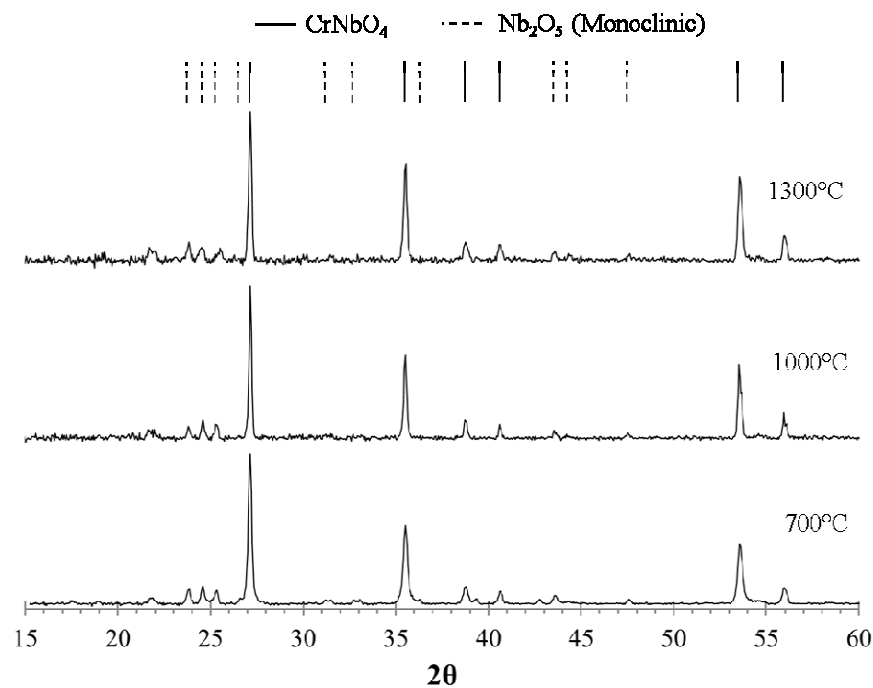


Figure 5.33 XRD spectra collected from oxide products after long term cyclic oxidation at 700, 1000, and 1300°C of the 15Mo5B alloy

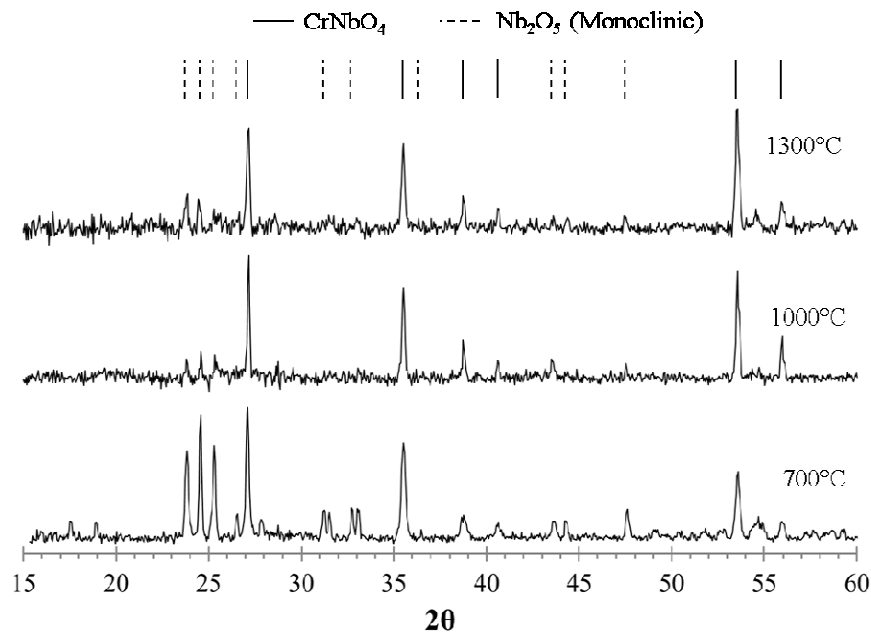


Figure 5.34 XRD spectra collected from oxide products after long term cyclic oxidation at 700, 1000, and 1300°C of the 10Mo5B alloy

## 5.6 SUMMARY

The oxidation response in air for three modified alloys based on the Nb-25Cr-20Mo-15Si-5B at.% alloy with modified molybdenum, silicon, and boron content were observed in a temperature range of 700 to 1400°C. Three phases were found to be common in the as-cast microstructures of all alloy compositions those being NbCr<sub>2</sub>, Nb<sub>5</sub>Si<sub>3</sub>, and a solid solution.

The short term oxidation results indicate that the higher boron content resulted in higher oxidation resistance. Thermal gravimetric results also indicate similar finding. The oxidation kinetics observed at 900 and 1000°C for the 15Mo5B were found to be linear. The 10B alloy was found to have parabolic oxidation kinetics at both 900 and 1200°C. The higher boron and molybdenum content also appear to have enhanced pest oxidation resistance at 700°C. Both the 15Mo5B and 10Mo5B were observed to suffer from catastrophic pest oxidation at 700°C. Boron was observed to be present in the un-oxidized solid solution and in Nb<sub>2</sub>O<sub>5</sub> but not in the SiO<sub>2</sub>

developed in the oxide scale on both the 15Mo5B and 10B alloys according to qualitative EDS analysis. The development of borosilicate could not be confirmed.

Transient oxidation behavior was observed in the thermal gravimetric results for the 15Mo5B and the 10B alloys. The Oxide scale development was examined to understand the transient oxidation behavior. The preferential oxidation of the  $\text{Nb}_5\text{Si}_3$  silicide was observed at the onset of the oxidation process which led to develop  $\text{Nb}_2\text{O}_5$  that allowed oxygen to attack the un-oxidized metal past the oxide metal interface resulting in rapid oxidation accounting for the transient oxidation behavior observed.

## **5.7 RECOMMENDATIONS**

The results obtained from increased molybdenum and boron content merit further investigation of this alloy system. Large additions of boron should be investigated to determine whether or not borosilicate can be developed a niobium based alloy.

Several issues that have hindered the application of niobium based alloys such as pest oxidation at intermediate and low temperatures were observed to be suppressed by the molybdenum and boron content in the 10B alloy. However, the issue regarding the cracks along the oxide metal interface should be addressed. Mechanical properties should also be examined and characterized to determine possible applications. By reducing the amount of primary alpha high oxidation resistance was achieved but the effects on the mechanical properties have not been examined yet.

Regarding the issue of the preferential oxidation of the  $\text{Nb}_5\text{Si}_3$  silicide refinement of the microstructure may possibly result in better oxidation resistance. Finer microstructures have been reported to offer better oxidation resistance [16, 17].

## 5.8 References

- 1 B. I. Portillo. and S.K. Varma. Metall. Mater. Trans. A. 42A (2011) in print.
- 2 Meyer M.K., Thom A.J., Akinic M. Intermetallics 7 (1999) 153.
- 3 Varma S.K., Portillo B, Alvarez D, Vazquez A. World J Eng. Supplement 2 (2010) 442.
- 4 Valot C, Ciosmak D, Lallemand M. Oxid Met 41 (1994) 235.
- 5 Zheng H, Lu S, Su Q, Quan F. Int J Refr Metals Hard Mater. 26 (2008) 1.
- 6 Valot C, Ciosmak D, Lallemand M. Oxid Met 41 (1994) 235.
- 7 P. Kofstad and K.P. Lillerud. Journal of the Electrochemical Society. 127 (1980) 2410-2419.
- 8 M. Skeldon, J.M. Calvert, and D.G. Lees. Oxidation of Metals. 28 (1987) 109-125.
- 9 M. K. Meyer, M. Akinc. Journal of the American Ceramic Society. 79 (1986) 938-944.
- 10 M. P. Arbuzov and V. G. Chuprina. Izvestiya VUZ. Fizika. 2 (1965) 129-133.
- 11 J.T. Clenny and C.J. Rosa. Metall. Mater. Trans. A. 11A (1980) 1385-1389.
- 12 T.P. Hennessey and J.E. Morral. Oxidation of Met. 38 (1992) 163-187.
- 13 J.S. Sheasby. Oxidation of Met. 1 (1969) 121-125.
- 14 G. Baran, M. Meraner, and P. Farrel. Oxidation of Met. 29 (1988) 409-418.
- 15 F. A. Rioult, S.D. Imhoff, R. Sakidja, J.H. Perepezko
- 16 R. Peraldi, D. Monceau, and B. Pieraggi. Oxidation of Met. 58 (2002) 249-273.
- 17 F.A. Rioult, S.D. Imhoff, R. Sakidja, J.H. Perepezko. Acta Materialia. 57 (2009) 4600-4613.

## Curriculum Vita

Benedict Portillo was born in El Paso, Texas. The second son of Raphael Portillo Jr. and Carmen Muñoz Portillo, he graduated from Socorro High School in the spring of 2001 and entered the University of Texas of El Paso in the fall with the Sjoerd Steunebrink Scholarship. He earned his Bachelor of Engineering degree in Metallurgical and Materials Engineering in 2005. He received his Masters of Science degree in Metallurgical and Materials Engineering in 2008 from the University of Texas at El Paso. In the summer of 2008 he joined the Materials Science and Engineering doctoral program.

While perusing his degree, he worked on research associated with the Office of Naval Research while at the University of Texas at El Paso. He presented his work at various international conferences including the 215<sup>th</sup> meeting of The Electrochemical Society in 2009 and The Minerals, Metals & Materials Society 2010 and 2011 annual Meeting & Exposition. His work *Behavior of Nb-20Mo-15Si-5B-20Ti Alloy in Air from 700 to 1300°C* was published in the Journal of Alloys and Compounds in 2010 and *Oxidation Behavior of Nb-20Mo-15Si-25Cr and Nb-15Si-25Cr-5B Alloys* was published in Metallurgical and Materials Transactions A in 2011.

Permanent address: 11450 Peters Rd.

Socorro, Texas 79836

This dissertation was typed by Benedict I Portillo II.